Miniaturized Microwave, Millimeter-wave, and sub-Terahertz Tunable Guided Wave Structures for Wireless Communication Beamforming Applications

by

Eric Thomas Der

A thesis submitted in partial fulfillment of the requirements for the degree of

Doctor of Philosophy

in

Electromagnetics and Microwaves

Department of Electrical and Computer Engineering
University of Alberta

Abstract

In order to meet the growing demands for faster and more reliable wireless communication networks, as well as to connect the billions of new devices that will require on demand access to the internet, the telecommunication industry seeks to expand the current wireless communication infrastructure into millimeter-wave and terahertz band where spectrum is abundant and relatively under-utilized. Transceiver antenna arrays at these frequencies require beamformer networks in order to be able to transmit over long distances with reasonable signal-to-noise ratios, while still being able to maintain coverage in all directions.

Many devices at these frequencies use waveguide components and interconnects due to their high-power handling and low-loss propagation characteristics. However, these devices are often difficult to integrate with planar circuit platforms. Furthermore, it is known that the size and complexity of phased array feed networks scales with the number of antenna elements. In a world with growing demand for more compact devices, it is therefore prudent to investigate miniaturization techniques of waveguide interconnects and devices. This thesis presents the theoretical background, simulation, engineering trade-off studies, practical implementation, and experimental results of novel waveguide components critical to 5G and 6G beamforming frontends such as Butler matrices, phase shifters, and single pole double throw switches, all implemented using miniaturized waveguide interconnects such as ridged half-mode substrate integrated waveguides (RHMSIW) and evanescent-mode waveguides.

Implementations of RHMSIW Butler matrices presented in this thesis at 3.5 GHz and 28 GHz 5G bands achieved some of the smallest form factors at the time of publi-

cation, achieving up to 73% miniaturization over their half-mode topology counterpart while still maintaining lower insertion loss over commercially available tunable phase shifters.

The silicon evanescent-mode waveguide switches presented in this thesis also achieve over 70% reduction in device volume over commercially available waveguide switches in the W-Band. Furthermore, the switches have three orders of magnitude higher measured speeds over state-of-the-art electromechanical switches in the band while still being able to theoretically handle 5 W of RF power. Using the equipment available at the time of publication, the switch technology was experimentally demonstrated to successfully handle 1.6 W of power. De-embedding the transitions, the switch technology achieves insertion losses as low as 0.5 dB.

Preface

This thesis is a compilation of original first-author works by Eric T. Der.

Parts of Chapter 2 and Chapter 3 have previously been published in the following conference and journal papers:

1. E. T. Der, T. R. Jones and M. Daneshmand, "Miniaturized tunable phase shifter using a periodically loaded ridged half-mode substrate integrated waveguide," IEEE MTT-S Int. Microw. Symp. Dig., Boston, MA, USA, 2019, pp. 180-183.

2. E. T. Der, T. R. Jones and M. Daneshmand, "Miniaturized 4×4 Butler matrix and tunable phase shifter using ridged half-mode substrate integrated waveguide," in IEEE Trans. Microw. Theory Techn., vol. 68, no. 8, pp. 3379-3388, Aug. 2020.

The contents of Chapter 4 was accepted for publication at the 2021 International Microwave Symposium conference entitled:

3. E. T. Der, T. R. Jones and M. Daneshmand, "A miniaturized 28 GHz 4×4 Butler matrix using shielded ridged half-mode SIW," IEEE MTT-S Int. Microw. Symp. Dig., Atlanta, GA, USA, 2021, pp. 776-779.

For the above contributions, Prof. Mojgan Daneshmand was the supervisory author who was involved in concept formation and manuscript editing. I was charged with the conception, design, simulation, fabrication, experiments, and write-up of the paper. Thomas R. Jones, was a senior doctoral candidate – and later post-doctoral

fellow – who provided technical support, experiment setup, and assisted with editing the submitted manuscripts.

The content on leaky-wave radiation in Chapter 4 will be submitted to the Transactions on Antennas and Propagation as a Communication under the title "Radiating Behavior of a Miniaturized Ridged Half-Mode Substrate Integrated Waveguide and its Application for K_a-Band 5G Leaky-Wave Antennas". Prof. Kambiz Moez is the supervisory author and was involved with editing the submitted manuscript and data analysis, and Adjunct Professor Thomas R. Jones assisted with the theory, data analysis, and editing the submitted manuscript.

The journal papers entitled:

4. E. T. Der et al., "A W-band SPDT photoconductive evanescent-mode waveguide switch," in IEEE Microw. Wirel. Techn. Lett., vol. 33, no. 6, pp. 831-834, Jun. 2023.

5. E. T. Der et al., "Design and characterization of W-band silicon micromachined high-power and high-speed photoconductive evanescent-mode waveguide single and double throw switches," in IEEE Trans. Microw. Theory Techn., 2023. DOI: 10.1109/TMTT.2023.3328483.

were completed during an internship with, and funded by, Jones Microwave Inc. (JMi). The work is presented in Chapter 5. This work was a joint collaboration between the University of Alberta, Purdue University, and JMi. Prof. Dimitrios Peroulis and Prof. Kambiz Moez were the academic supervisory authors. Prof. Peroulis provided support with the concept formation, theory, design, and experiments. Both Profs. Peroulis and Moez were involved with manuscript editing. Thomas R. Jones, Douglas W. Barlage, and Alden Fisher developed most of the semiconductor and optical theory for the work. JMi, under the leadership of CEO Thomas R. Jones, was responsible for all of the fabrication work under their proprietary process and provided the equipment and technical support for characterizing the work. Thomas R.

Jones also provided assistance with concept formation, design, and with experiment setup. Michael D. Sinanis assisted JMi with their process development.

In all of the above contributions, I was responsible for the concept formation, microwave theory, design, simulation, experiments, and manuscript composition.

yo sahassaṃ sahassena saṅgāme mānuse jine |

ekañca jeyyam'attānaṃ sa ve saṅgāmajuttamo ||

One may conquer a thousand men in a thousand battles. But the person who conquers just one person, which is one's own self, is the greatest conqueror.

attā have jitaṃ seyyo yā cāyaṃ itarā pajā |

attadantassa posassa niccaṃ saññatacārino ||

Self conquest is greater than the conquest of others. The victory of one who conquers himself cannot be turned into defeat. He remains a self-controlled individual who lives ever disciplined.

n'eva devo na gandhabbo na māro saha brahmunā |

jitaṃ apajitaṃ kayirā tathārūpassa jantuno ||

Not even gods together with demons can turn such a conquest into defeat.

-Siddhārtha Gautama (Dhammapada v.103-105)

此生永念
父母恩、如來恩、師長恩、國土恩。

Acknowledgements

I would first like to express my sincere gratitude to my late supervisor, Prof. Mojgan Daneshmand who supervised the work presented here up until 2020. I thank her for placing her trust in me and her enthusiasm in encouraging me to transfer into the PhD program shortly before her untimely passing. She will forever be remembered for her patience, humility, and sense of humour that always made our biweekly meetings events to look forward to. May she rest in peace.

I would also like to extend my gratitude and appreciation to my current supervisor, Prof. Kambiz Moez, who provided so much support for the members of Prof. Daneshmand's group during the initial shock and chaos that kicked-off the new decade, and who later unconditionally agreed to assume supervision over this very lost graduate student's research. I thank him for his patience and understanding in letting me take on a full-time internship during the final years of my studies in addition his practical advice and selfless support in helping me bring my work closer to its conclusion.

I would also like to thank Prof. Ashwin Iyer and Prof. Rashid Mirzavand for lending out equipment over the course of this research, as well as the other members of my committee, Prof. Van and Prof. Mansour for all of their valuable feedback.

The support of Dr. Thomas R. Jones has also been instrumental to the success of this research, who secured the funding for its final stages, and who should most certainly be recognized as one of my mentors. Thank you for all of the stimulating and educational discussions about electromagnetics, candid advice about various topics, as well as all of the random conversations about the interesting times and strange world we find ourselves living in.

And of course, many thanks go to Gordon Okamura sensei and Kelly Palmer sensei for their dedication and patience in helping me improve in the art they are so passionate in – as slow of a process as that may sometimes be – as well as the rest of the U of A Judo Club for giving me some my best memories in grad school, where I spent a better part of my time on campus outside of the lab throughout my program. One of the biggest takeaways from these past seven years of practice is the reminder that very first lessons in Judo are about learning how to fall, both metaphorically and literally; that to be able to pull off any fancy moves, one must first develop the resilience to overcome the fear of falling.

Most importantly, I would like to thank my parents for providing a warm and stable home to return to everyday – in both good times and bad times – for providing that inertial frame of reference in a life that can sometimes get very chaotic, and for being the voice of reason reminding me that there are more important things in life beyond the ceaseless pursuit of profit and material "success" that the world often gives us the illusion of believing are paramount. Especially during these interesting times, I also find myself a lot more appreciative of the series of sacrifices they have made throughout their lives that eventually led to me being born and raised in a land far away from the horrors of war and tyranny, in a land with clean air and water, the rule of law, responsible government, and freedom of speech, in this great Western democracy we know as Canada. I could not have asked for a better set of initial conditions that I have not actually done anything in this lifetime to deserve, and cannot even begin to fathom how many orders of magnitude more difficult this 28 year journey would have been were any these fundamental pillars missing or eroded.

To all of this I offer my eternal gratitude. Thank You.

Table of Contents

List of Tables

List of Figures

List of Symbols

Constants

ϵ_0	Permittivity of free space.	$8.85418782 \cdot 10^{-12}\, F/m$
c	Speed of light in a vacuum inertial system.	$2.99792458 \cdot 10^{8}\, m/s$
h	Planck constant.	$6.62607015 \cdot 10^{-34}\, Js$
q	Elementary charge.	$1.602176634 \cdot 10^{-19}\, C$

Latin

a	Waveguide transverse width
f	Frequency
f_c	Cutoff frequency
k	Angular wavenumber
k_0	Free space angular wavenumber
k_c	Cutoff angular wavenumber
m	Mass

Greek

α	Attenuation constant
β	Phase constant
ϵ	Permittivity
ϵ_r	Relative permittivity
γ	Propagation constant
λ_0	Free-space wavelength
λ_g	Guided wavelength
ν	Optical frequency

Abbreviations

5G Fifth generation of cellular networks.

6G Sixth generation of cellular networks.

CAD Computer-aided design.

CPW Coplanar waveguide.

EVA Evanescent-mode.

HMSIW Half-mode substrate integrated waveguide.

IC Integrated circuit.

IL Insertion loss.

MIMO Multiple-input-multiple-output.

mmWave Millimeter-wave.

PCB Printed circuit board.

PEC Perfect electric conductor.

PMC Perfect magnetic conductor.

RF Radiofrequency.

RHMSIW Ridged half-mode substrate integrated waveguide.

RL Return loss.

RWG Rectangular waveguide.

SIW Substrate integrated waveguide.

SPDT Single pole double throw.

SPST Single pole single throw.

TE Transverse electric.

TEM Transverse electromagnetic.

TL Transmission line.

TM Transverse magnetic.

Chapter 1

Introduction

1.1 Motivation

In a world with rising demand for wireless connectivity and data rates, coupled with the fact that the currently utilized low-GHz has limited bandwidth, it is clear that the current wireless communication spectrum is congested and will not be able to sustain the growing traffic [1]. Furthermore, there are roughly 30 billion devices currently communicating over the internet-of-things (IoT), and this figure expected to double over the next four years [2].

One of the key solutions concerning microwave engineers that the fifth generation of mobile networks (5G) proposes is the expansion of the current infrastructure into the millimeter-wave (mmWave) domain where bandwidth is widely available and for the most part, currently unused. At the 28 GHz 5G band, peak data rates of 10 Gbps have already been demonstrated [3]. Moving forward, telecommunication giants such as Samsung, Ericsson, and Nokia have already begun research and development efforts on a sixth generation of wireless networks (6G) and have already proposed the utilization of the sub-terahertz (sub-THz) spectrum for even faster data transmission [4–6].

Although the benefits of mmWave to the future of wireless communications are clear, there remains significant gaps in available technology at these frequencies. According to the Friis equation [7], in order to achieve greater range and improved link

margins as well as to compensate for the high atmospheric attenuation at mmWave frequencies, high gain antennas or arrays are key technologies to enable 5G and 6G radio transmission.

However, high gain radiating elements also limit the physical field-of-view of the transmitter due to their narrower beamwidths. To ensure adequate spatial coverage for transceivers equipped with these high gain antenna elements or arrays, there needs to be some form of capability to dynamically adjust the beam patterns of these radiators such that maximum power is always transmitted between transceivers in motion, techniques known as beam steering or beam switching [8]. Beam steering involves electronically steering the beam of an array by tuning the phase delay of each of its elements. Beam switching on the other hand, involves the redirection of transceiver signals to fixed beam radiating elements that are oriented in several directions; where the element(s) that is/are oriented in the direction of the target transceiver is switched on by the system. With losses even higher in the THz domain - directive, electronically steerable / reconfigurable antennas arrays are even more critical for enabling reliable, high-speed wireless networks [9].

Phased array beam steering - as the name implies - requires the capability to dynamically tune the electrical phase of each array element. One way of doing so is to feed each element with a tunable phase shifter. However, while a variety of options exists for adjusting electrical phase at microwave frequencies, there are a lack of solutions for low-loss, tuning components in the millimeter-wave domain. Furthermore, commercially available phase shifter ICs between 28 to 37 GHz already suffer high insertion losses on the order of 6 dB [10] which are expected to be even higher at sub-THz frequencies. It may therefore be more practical to use discrete beamformers such as Butler matrices which have been shown to have much lower loss owing to the fact that they are purely made up of passive transmission line structures. Alternatively, switched multiple-input-multiple-output (MIMO) omnidirectional arrays have also been proposed where multi-throw switches are used to switch discrete directive

elements on and off, eliminating the need for complex feed networks altogether [11]. Regardless of which solution (or combination of solutions) is used, it is clear that low-loss, compact multi-throw switches, beamforming networks, and phase shifters are critical components in the deployment of 5G and 6G.

Millimeter wave radio transmitters also require higher output powers to maintain an adequate signal to noise ratio (SNR) [8]. Investigations between 71-86 GHz (E-band) have shown 6 Gbps data rates over 36 km with transmitter powers of 0.7 W [12], and this power requirement is expected to be even higher in the W-band (75-110 GHz) radios proposed for 6G. One significant challenge with increased power is the capability of the transceiver front-end system to handle it. At mmWave frequencies, front-ends typically use waveguides due to their high power handling and low insertion loss. However, many of these solutions are manufactured through traditional metal-machining, limiting their ability to be mass-produced and are generally difficult to integrate with planar microwave technologies. With the deployment of compact base station transceivers known as pico-cells being critical for enabling efficient high frequency 5G and 6G networks [13], and the knowledge that the complexity and size of phased-array beamformers scale with the number of antenna elements [14], it is prudent to investigate techniques to miniaturize low-loss, energy-efficient beamforming networks / components in order to ensure widespread use of the technology [15]. The key to solving this problem lies in miniaturizing the system's building blocks and interconnects.

Over the past decades, the demand for planar circuits has motivated researchers to develop substrate integrated waveguide (SIW) technology where rows of metallized via interconnects are used to emulate the electric sidewalls of a reduced height rectangular waveguide and can be fabricated on a PCB. Although SIWs are a good compromise between the planarity of microstrip transmission lines and the low-loss, high-power handling capabilities of rectangular waveguides, the growing demand for electronic devices with a smaller form factor has motivated researchers to devise techniques for

miniaturizing SIW. One such recent technology as a result of that work is the ridged half-mode SIW (RHMSIW) that has the potential to provide over 70% miniaturization in the footprint of conventional SIW [16].

At even higher frequency bands, the size of waveguide devices have a tendency to decrease, making them very sensitive to fabrication tolerances, and it is also known that dielectric losses have a tendency to increase linearly with frequency. Therefore, in the W-band and beyond, the use of an alternative platform that can fabricate air-core waveguides with very tight fabrication tolerances may be required. Silicon micromachining has been shown to be a good candidate, with fabrication tolerances on the order of micrometers and the potential to be integrated with mainstream planar technologies such as CMOS. In recent years, silicon micromachining has already been shown to to be able to successfully fabricate waveguide devices that operate up to THz frequencies [17].

With the demand of small form-factor in consideration as well as the need for high frequency, high power handling beamforming frontends and components for enabling future generations of communication systems, this thesis investigates and documents the design of miniaturized integrated waveguide Butler matrices, phase shifters, and multi-throw switches.

1.2 Thesis Objectives

With the aforementioned need for bandwidth as well as beamforming technologies in the future of wireless communication systems, and the demand for compact devices, the main objectives of this thesis is to demonstrate the transformation of waveguide miniaturization theory into practical implementation of critical beamforming network devices and components. Firstly, novel interconnects will be developed from the application of RHMSIW miniaturization theory and be used to construct novel microwave and millimeter-wave miniaturized Butler matrices and phase shifters. Likewise, evanescent-mode waveguide filter theory will be applied to the development

of wideband, low-loss, high-speed, high-power handling planar waveguide switches operating in the W-Band. To these ends, studies will be conducted to establish the optimal operating conditions of RHMSIW along with studies of evanescent-mode waveguide design trade-offs.

1.3 Thesis Outline

This thesis is presented over six chapters. Chapter 1 details the motivations and objectives of this research project.

Chapter 2 will go over the theoretical background behind the proposed research namely rectangular waveguide theory, SIW miniaturization techniques, and a detailed literature review of the existing techniques for telecommunication beamforming and beamswitching.

Chapter 3 forms the theoretical and experimental backbone of using miniaturized SIW are to develop beamforming devices; a phase shifter and Butler matrix operating at a sub-6 GHz 5G band is presented.

In Chapter 4, it will be shown how the design philosophy from Chapter 3 can be refined for realizing a millimeter-wave version of the Butler matrix design and also presents an analysis of the radiation conditions of the miniaturized SIW used in this work and its application for developing leaky-wave antennas.

The evanescent-mode waveguide approach to device miniaturization is demonstrated in Chapter 5 where reconfigurable, high speed, low-loss, high power handling, optically biased solid-state W-Band (90 GHz) waveguide switches are presented.

Finally, Chapter 6 concludes this thesis by summarizing the key contributions of this research and proposes various future directions for developing the proposed technologies.

Chapter 2

Background

2.1 Waveguide Theory and Miniaturization

Although microstrip transmission lines are widely used to date in microwave circuit design and have a relatively small form factor, they have a tendency to suffer from significant radiation loss at higher frequencies [18]. Rectangular waveguides on the other hand, are popular interconnects used to propagate microwave power at millimeter-wave frequencies due to their high-power handling and excellent high frequency performance [7], both properties that are required to compensate for higher path loss and atmospheric attenuation at higher frequencies. Because waveguides are constructed on one single conductor as opposed to planar transmission lines such as microstrip, stripline, and CPW, a signal propagating inside the medium enclosed by the waveguide's conductor is prevented from radiating and is also shielded from external signal interference. Waveguides have been shown to perform well up to terahertz frequencies but have the disadvantage of having a relatively large physical size as well as being non-planar structures. This section will establish the basic conventions that will be used to discuss waveguides for the rest of the thesis and then review the various techniques used for planarizing and miniaturizing waveguides for more compact device integration.

2.1.1 Rectangular Waveguides

The waveguide is unique in that it allows an electromagnetic wave to propagate through it as long as the width of the waveguide aperture is larger than the wavelength of the EM wave despite only having a single conductor. However, owing to the structure consisting of a single monolithic conductor, the rectangular waveguide (RWG) cannot support TEM modes and will always either have components of the magnetic field (TE modes) or the electric field (TM mode) directed parallel or antiparallel to the direction of propagation, and each of these TE and TM mode have cutoff frequencies below which there is no propagation of the mode [7]. Fig. 2.1 illustrates the spatial convention that will be used for the remainder of this thesis.

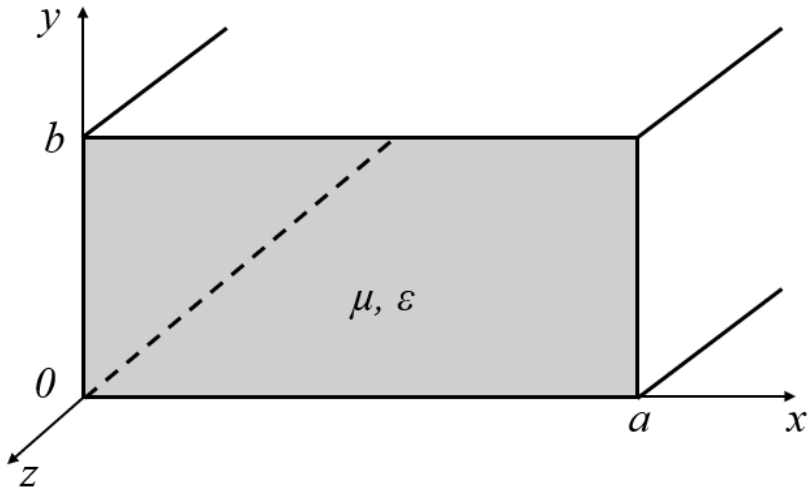

Figure 2.1: Cross-section of a generic rectangular waveguide with width a and height b. By convention, propagation is defined in the positive z direction.

For the applications presented in this thesis, we are generally interested in the TE modes of propagation i.e. there is no electric field in the direction of propagation ($E_z = 0$), and the while the magnetic field is non-zero and represented by $H_z = h_z(x, y)e^{-j\beta z}$. The transverse components of the electric and magnetic field (E_x, E_y, H_x, H_y) can be computed from H_z using Faraday's law (2.1) and Ampere's Law (2.2) [7]:

$$\nabla \times E = -j\omega\mu H \tag{2.1}$$

$$\nabla \times H = j\omega\epsilon E \tag{2.2}$$

where μ and ϵ are respectively, the permeability and permittivity of the propagation medium, and β is the propagation constant of the mode and can be computed using equation (2.3):

$$\beta = \sqrt{k^2 - \left(\frac{m\pi}{a}\right)^2 - \left(\frac{n\pi}{b}\right)^2} \tag{2.3}$$

where integers m and n are mode numbers and $k = 2\pi/\lambda_0$ is the free-space wavenumber with λ_0 being the free-space wavelength of the wave propagating in the waveguide. The mode that begins to propagate at the lowest frequency, known as the "fundamental mode", is the TE_{10} mode with m = 1 and n = 0. The following subtleties can be observed from equation (2-3):

1. The argument of the square root must be greater than zero for a real propagation constant to exist. Below a certain frequencies (when λ_0 increases past a certain point) for a given m and n, β becomes imaginary and the field components decay exponentially from the source [7]. This is known as the cutoff frequency.

2. Rectangular waveguides are dispersive in nature as the propagation constant does not vary linearly with frequency. Since the phase incurred in a transmission line is defined as β_z, phase does not vary linearly with phase in a waveguide. As the frequency approaches cutoff, the effect of dispersion is more apparent.

Generally, as a rule of thumb, a waveguide's operational frequency range is between 125% and 189% of the cutoff frequency [19] above which undesired higher modes may begin to be excited, and below which the signal propagating through the waveguide begins to experience significant attenuation or exhibit dispersive behaviour. Standard RWGs are fabricated to have the height b exactly half of the width a. However in some applications such as wafer-level waveguides [20, 21] and substrate integrate waveguides [22], the fabrication process or substrate thickness may limit the height of the waveguide channel. While this may affect the power handling of the waveguide,

it can be shown using (2.3) and the following equation for the cutoff frequency for TE modes, that the cutoff frquency of the fundamental TE_{10} propagation mode is theoretically unaffected by the reduced height:

$$f_{c_{m,n}} = \frac{1}{2\pi\sqrt{\mu\epsilon}}\sqrt{\left(\frac{m\pi}{a}\right)^2 + \left(\frac{n\pi}{b}\right)^2} \tag{2.4}$$

According to (2.4), for any TE_{m0} (m and n in equations (2.3) and (2.4) are some integer m and 0 respectively) mode, the term under the radical containing b disappears, eliminating the RWG propagation characteristics' dependence on height. This behaviour can be observed in Fig. 2.2 which shows that the cutoff frequency of PEC rectangular waveguides does not change with height. However, it can be seen from Fig. 2.3 that the characteristic impedance of the waveguide decreases with height. At heights approaching zero, the impedance becomes prohibitively low to couple any energy into the waveguide in practical device designs. At a height of 3 µm, the impedance of a standard width W-Band waveguide decreases to just 0.7Ωat midband.

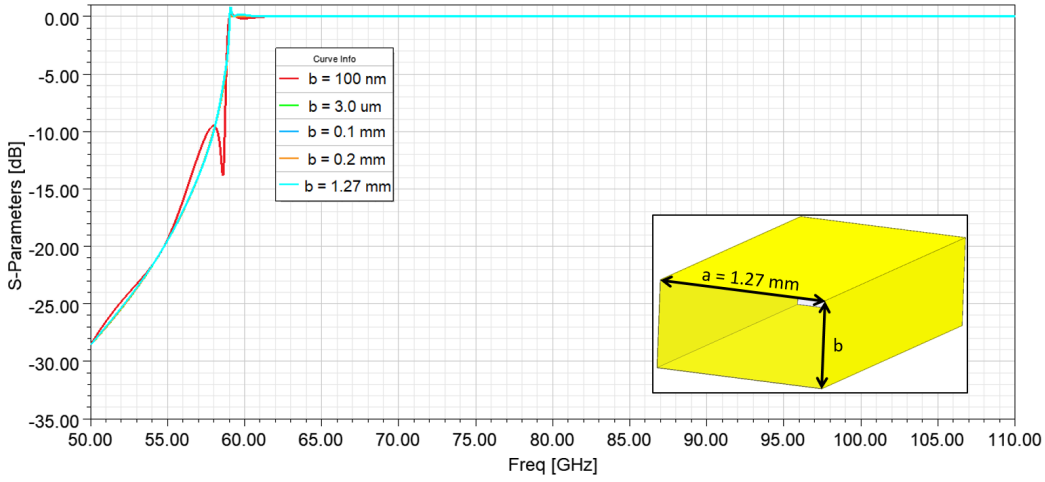

Figure 2.2: The simulated S_{21} responses of PEC rectangular waveguides of varying heights.

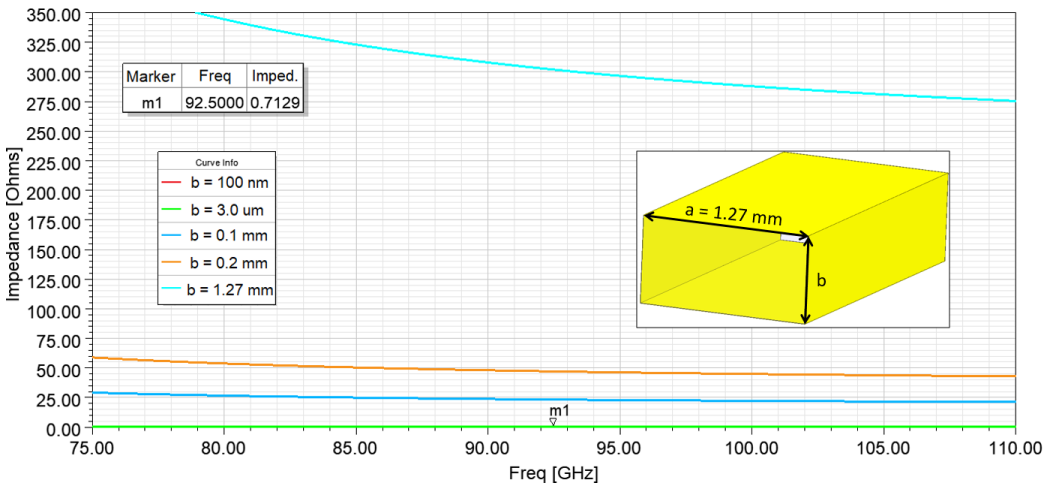

Figure 2.3: The simulated characteristic impedance of PEC rectangular waveguides of varying heights.

It is also important to note that the waveguide loss has dependence on the channel height once the PEC boundaries are replaced with real metals with finite conductivity as shown by the following conductor loss equation for the TE_{10} mode:

$$\alpha_c = \frac{R_s}{a^3 b \beta k \eta} \left(2b\pi^2 + a^3 k^2\right) \tag{2.5}$$

where R_S is the surface resistance of the conductor wall and η is the intrinsic impedance of the material filling the channel [7]. It can be seen from (2.5) that the conductive loss of the TE_{10} mode increases as the channel height b decreases. A parametric study evaluating the effect of channel height on the unloaded quality factor of a single-pole wafer level rectangular waveguide cavity resonator was conducted in [23]; it was shown that the resonator has a 87.6% increase in quality factor when the channel height was doubled from 50 µm to 100 µm which is in agreement with our observations from equation (2.5). Furthermore, it can be seen from Fig. 2.4 that signal attenuation due to conductive losses may become prohibitive to practical designs as the channel height approaches zero.

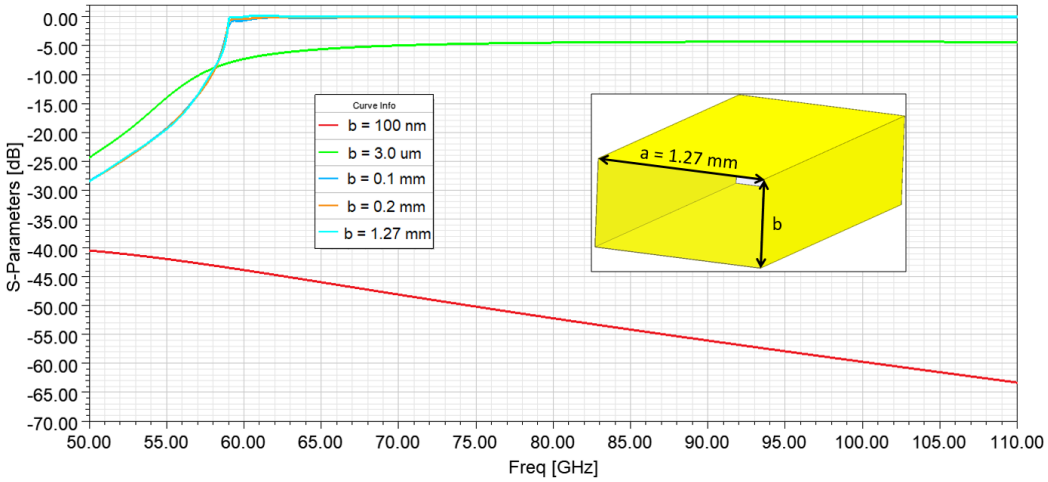

Figure 2.4: The simulated S_{21} responses of rectangular waveguides of varying heights using a conductor with finite conductivity (4.1×10^7 S/m).

2.1.2 Substrate Integrated Waveguides

Owing to the demand for compact devices and the difficulty of integrating three-dimensional rectangular waveguides with planar circuits, substrate integrated waveguides (SIW) were developed over the past few decades as a compromise between the integrability of planar transmission lines (such as microstrip, coplanar waveguides, and striplines) and the high power-handling, good high frequency performance of rectangular waveguides [24]. The study conducted in [24] has highlighted the excellent power handling capabilities of SIW interconnects at high frequencies, which were shown to be able to handle up to 450 W of power at 10 GHz and up to 70 W at 30 GHz.

It should also be noted that due to the discontinuous nature of the via "sidewall", it is not possible to propagate TM modes in SIW structures or any of their miniaturized counterparts.

The electric sidewalls of the rectangular waveguide are emulated with rows of tightly spaced metallized via interconnects between the top and bottom conducting plane of the waveguide. An illustration of a generic SIW structure is shown in Fig. 2.5 [25]:

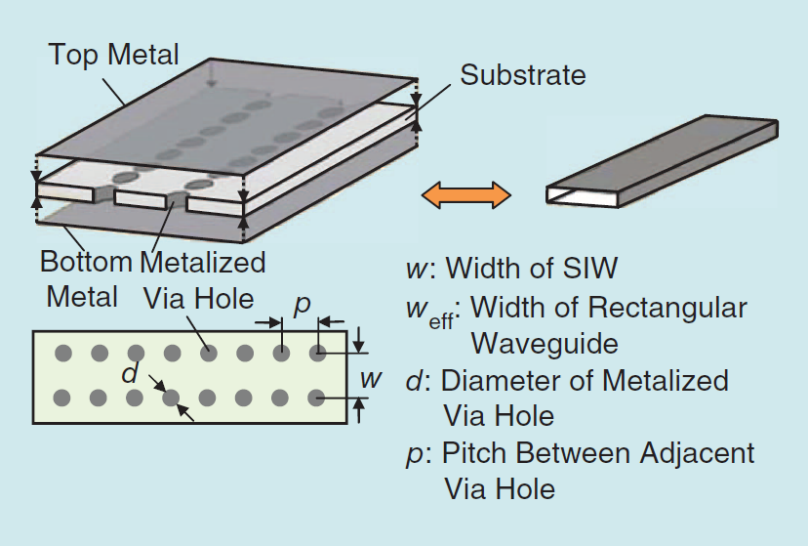

Figure 2.5: Model and diagram of a generic SIW structure [25] © [2014] IEEE

Because the sidewall of the SIW is discontinuous and periodic, there is the possibility of leakage losses and bandgaps to form. However, bandgaps can be avoided by ensuring that the pitch p, is smaller than a quarter of the cutoff wavelength ($p < \lambda_c/4$) [25, 26]. To ensure leakage losses are negligible while still being mechanically possible to fabricate the pitch should be greater than, but no more than double the diameter of the via holes ($d < p \leq 2d$). The effective width of an equivalent rectangular waveguide can also be calculated as follows [25]:

$$w_{eff} = w - 1.08 \times \frac{d^2}{p} + 0.1 \times \frac{d^2}{w} \tag{2.6}$$

where (w_{eff}) is the effective width of an equivalent RWG (the dimension a in the previous subsection) and w is the width of the SIW channel (between the centers of both via holes). As long as $p/d < 3$ and $d/w < 0.2$, equation (2-6) can be used to accurately convert between RWG and SIW models.

2.1.3 Half-mode Substrate Integrated Waveguides

The development of SIW technology in the past few decades has allowed high power handling, high quality factor, and low cross coupling devices to be fabricated

up to millimeter-wave frequencies [24] and widely used for a variety of applications. However, SIW structures still have a tendency to occupy a significant amount of board space and the growing demands for more compact devices in recent years has motivated researchers to propose techniques to miniaturize SIW structures such as the half-mode SIW (HMSIW) which effectively reduces the total footprint of conventional SIW by 50% [27]. Fig. 2.6 compares the transverse electric field configurations of SIW and HMSIW operating in their respective fundamental modes and demonstrates how SIW can be miniaturized into HMSIW:

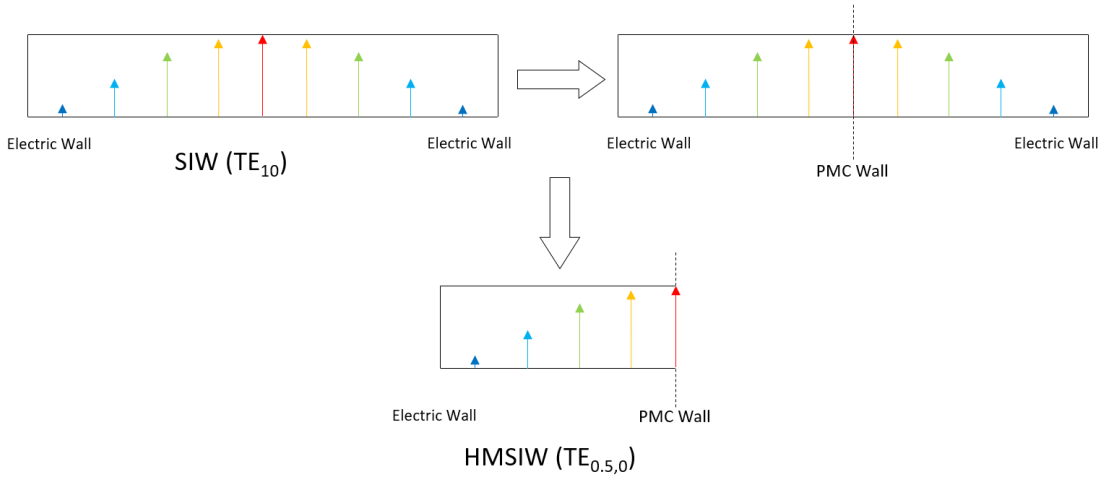

Figure 2.6: A comparison of the transverse field configuration of a conventional SIW propagating the TE_{10} mode and a HMSIW propagating the "$TE_{0.5,0}$" mode.

Consider the transverse plane of an SIW operating in the fundamental TE_{10} mode as shown in Fig. 2.6; a virtual magnetic wall can be introduced down the center of the transverse plane without violating the field configuration of the mode. It was shown in [27] that if the waveguide channel's width-to-height ratio is sufficiently high after bisecting the channel such that the fringing fields on the open end of the HMSIW are small, then the open end behaves as if a magnetic wall is present, this new mode is known as $TE_{0.5,0}$ [28]. The result is a footprint reduction of approximately 50%, with the scale of miniaturization limited by the amount of fringing at the open end [28]. The correction factor to the HMSIW effective width due to an imperfect MC boundary (from fringing) can be calculated from equation (13) in [28].

In [28], the high frequency performance of microstrip, SIW, and HMSIW was also investigated. The dominant attenuation in the HMSIW is due to conductive losses and it was reported that radiation losses are negligible when the waveguide operates within the operational bandwidth of its fundamental mode sufficiently above cutoff. Fig. 2.7 compares the measured attenuation constant of microstrip, SIW, and HMSIW vs. frequency [28] where it can clearly be seen that the difference in losses between SIW and HMSIW are negligible above 36 GHz and that both waveguide structures have superior performance to microstrip.

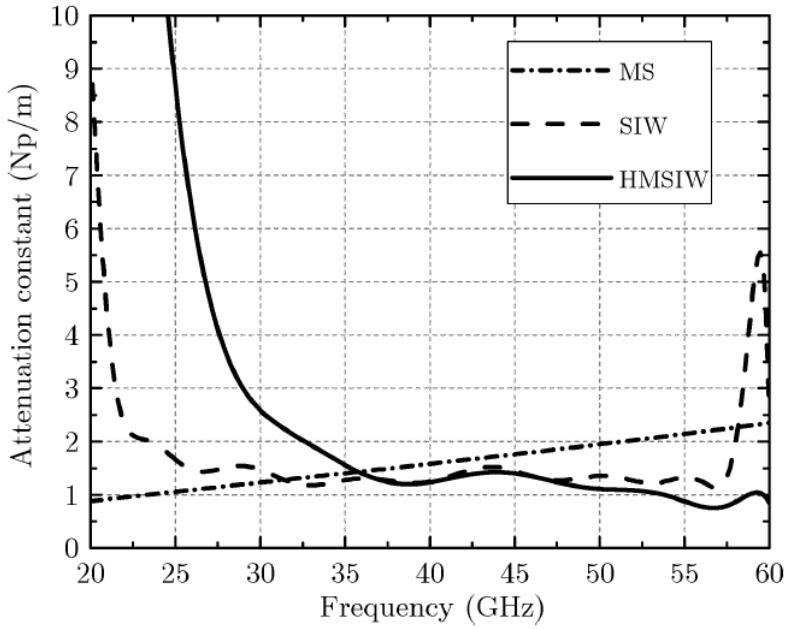

Figure 2.7: A comparison of the measured frequency response of attenuation constants for microstrip, SIW, and HMSIW [28] © [2009] IEEE.

2.1.4 Ridged Half-mode Substrate Integrated Waveguides

Recently, it has been shown that HMSIWs can be further miniaturized through the introduction of a capacitive ridge; the result is a miniaturization of up to 70% in comparison to full-mode SIW. A size comparison of the three waveguide structures described is shown in Fig. 2.8. Additionally, it has been shown that the open-end of RHMSIW suffers less radiation loss in comparison to HMSIW [16].

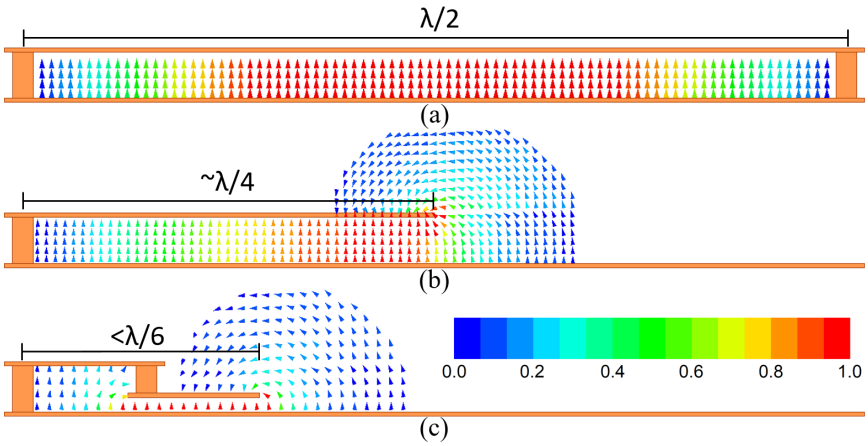

Figure 2.8: Transverse plane fundamental mode electric field configurations and size comparison of (a) full-mode SIW, (b) HMSIW, and (c) RHMSIW.

Through the application of the transverse resonance method, which can be used to obtain the cutoff frequency and dispersion relation of a guided wave structure, it was shown in [16] that the HMSIW could be miniaturized further when a capacitive ridge is introduced on the open side of the waveguide.

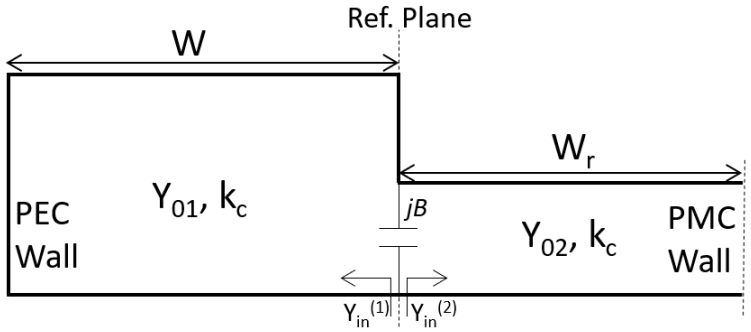

Figure 2.9: The transverse model of a RHMSIW.

Fig. 2.9 depicts the transverse model of a HMSIW with a capacitive ridge introduced; the RHMSIW can be modelled as a HMSIW with a step discontinuity in its transverse plane where there is a transmission line terminated with a short-circuited stub on one end while the other end is terminated with an open circuit. The transverse resonance technique states that the sum of the input admittances looking to the left and right of an arbitrarily placed reference plane must equal zero [16]:

$$Y_{in}^{(1)} + Y_{in}^{(2)} = 0, \tag{2.7}$$

where $Y_{in}^{(1)}$ is the input admittance looking towards the left of the reference plane and $Y_{in}^{(2)}$ looking to the right of the reference plane. For simplification, the reference plane can be placed at the step discontinuity in Fig 3.2. The input admittance, $Y_{in}^{(1)}$, of a short-circuited stub with characteristic admittance of Y_{01} can be calculated using:

$$Y_{in}^{(1)} = -Y_{01} \cot(k_c W), \tag{2.8}$$

where k_c is the the fundamental transverse electric mode's ($\mathrm{TE}_{0.5,0}$) cutoff wavenumber and W represents the width of the full height section of the RHMSIW channel. For calculating the propagation constant of the fundamental propagation mode, the open edge of the capacitive ridge can be assumed to be a virtual perfect magnetic conductor (PMC) boundary. The input admittance of the open-circuited stub with characteristic admittance Y_{02} is therefore computed with:

$$Y_{in}^{(2)} = Y_{02} \tan(k_c W_r), \tag{2.9}$$

where W_r is the width of the reduced height ridge. Substituting (2.8) and (2.9) into (2.7) and dividing both sides by Y_{01}, we obtain:

$$-\cot(k_c W) + \frac{B}{Y_{01}} + \frac{Y_{02}}{Y_{01}} \tan(k_c W_r) = 0 \tag{2.10}$$

From (2.10), the RHMSIW channel's cutoff wavenumber k_c, and by extension, the cutoff frequency can be numerically computed. Note that an additional susceptance term jB representing the capacitance introduced by the ridge was added to the input admittances at the reference plane. Y_{01}, Y_{02}, and B can be obtained numerically from equations (4)–(10) detailed in [16] and Sec. 5-26 of [29]. With k_c, the propagation constant (β) of the guide can then be obtained as follows [7]:

$$\beta = \sqrt{k^2 - k_c^2} \tag{2.11}$$

where k is the wavenumber of an unguided TEM wave propagating in the medium which the RHMSIW device is constructed with.

It was also shown in [16] that maximum miniaturization of the waveguide is achieved when the ridge width (W_r) is between 45 to 50% of the total width ($W + W_r$) of the waveguide. Fig. 2.10 illustrates the difference in width between fabricated HMSIW and RHMSIW C-band (4 to 8 GHz) test lines.

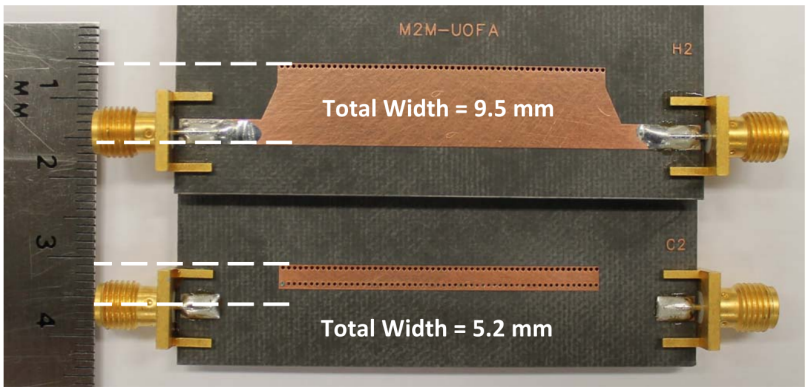

Figure 2.10: Size comparison of HMSIW and RHMSIW test lines fabricated for C-band operation. [16] © [2016] IEEE

Furthermore, it has been shown in simulation and the measurement of the test lines in Fig. 2.10, that the RHMSIW line has a 0.5 dB improvement in insertion loss over the HMSIW line due to lower radiation loss and by extension, there is less cross-coupling between adjacent RHMSIW interconnects in comparison to their HMSIW counterparts [16]. The experiments in [16] also shows that the main contributor to losses in HMSIW is radiation loss.

As depicted in Fig. 2.8, the electric field strength in the RHMSIW is maximum at the capacitive ridge due to the reduced height of that section of the waveguide [16]; this fact is key to the novel designs presented in this thesis and will be discussed in later chapters with greater detail.

Thus far, RHMSIW has been used for the implementation of couplers [16] and

filters [30]. Additionally, a wafer level monolithic waveguide version of the RHMSIW interconnect has been developed [31], showing the potential for this technology to be deployed for a variety of microwave and mmWave solutions.

Fig. 2.11 presents a study of different dimensions of a RHMSIW structure. The simulated lines are constructed on a substrate with an ϵ_r of 3.0 and the waveguide channel is formed with PEC. At different ridge heights (h_2), the transverse dimensions (W and W_r) are tuned such that all of the lines have approximately the same cutoff frequency. Note that the sidewalls were replaced by a solid wall to speed up simulations. From the study, it can be seen that by reducing the height of the ridge (thereby increasing the capacitive loading), smaller transverse dimensions are required to realize the same cutoff frequency, effectively increasing the miniaturization of the interconnect.

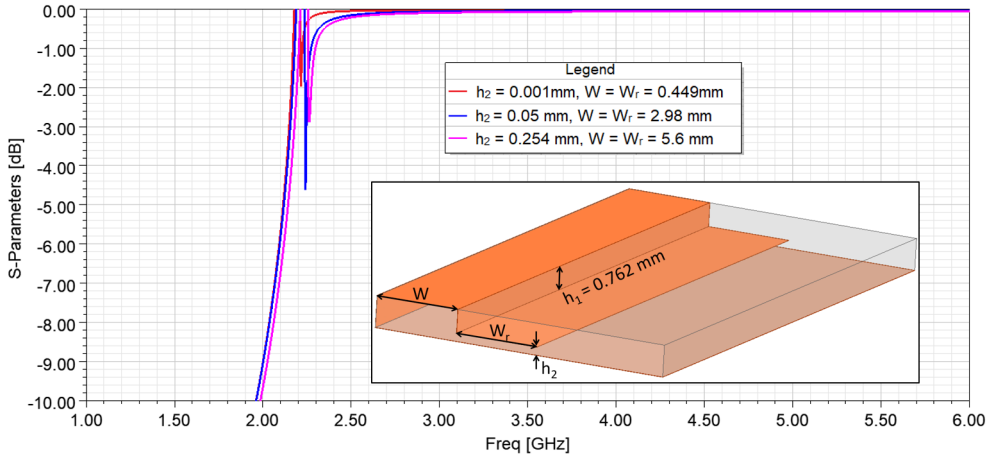

Figure 2.11: The simulated S_{21} responses of PEC ridged half-mode waveguides of varying dimensions with the same cutoff frequency.

However, analogous to what was observed with full-mode rectangular waveguides, it can be seen in Fig. 2.12 that the impedance of RHMSIW will decrease as their miniaturization increases until coupling energy into the waveguide can no longer practically be achieved. Additionally, similar to what was observed in Fig. 2.4, it can be seen in Fig. 2.13 that conductor losses may be prohibitive to be used as a practical interconnect as the degree of miniaturization of RHMSIW increases.

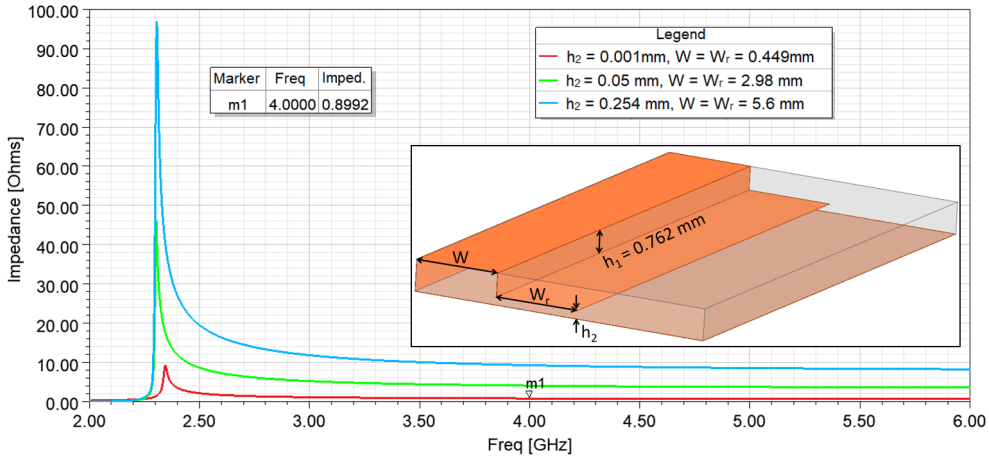

Figure 2.12: The simulated characteristic impedances of ridged half-mode waveguides of varying dimensions with the same cutoff frequency.

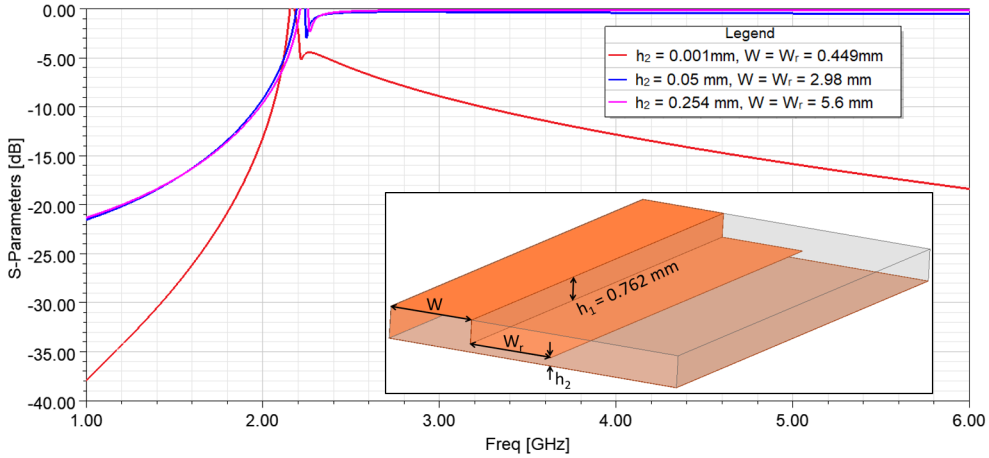

Figure 2.13: The simulated S_{21} responses of ridged half-mode waveguides using a conductor with finite conductivity (5.8×10^7 S/m).

2.1.5 Waveguide Short-Slot Couplers

Short-slot couplers are a critical component in the Butler matrices that will be presented in later chapters. The structure of the short-slot coupler consists of two side-by-side waveguides of equal dimension sharing a common wall. An opening in the common wall provides coupling between the two interconnects and is known as the "coupling region" [32]. A top down view of an RWG short-slot coupler is presented in Fig. 2.14.

The principle of operation for the short-slot coupler can be described through even

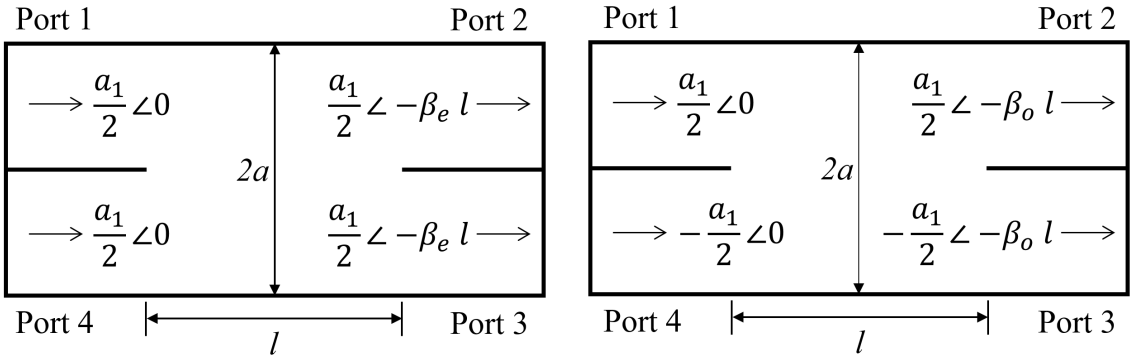

Figure 2.14: The top-down view and even-odd mode analysis of a short slot coupler. (a) Even mode excitation (b) Odd mode excitation.

and odd mode analysis; the even and odd modes excited in the coupling region incur phase at different rates. In even mode excitation, the TE_{10} mode is excited in the coupling region of width $2a$ with $\beta_e = 2\pi/\lambda_{g_e}$, whereas in odd mode excitation, the TE_{20} mode is propagated with $\beta_o = 2\pi/\lambda_{g_o}$. The guided wavelengths of the two modes are respectively [32]:

$$\lambda_{g_e} = \frac{\lambda}{\sqrt{1-\left(\frac{\lambda}{4a}\right)^2}} \tag{2.12}$$

$$\lambda_{g_o} = \frac{\lambda}{\sqrt{1-\left(\frac{\lambda}{2a}\right)^2}} \tag{2.13}$$

The phase difference between the modes is then $\Delta\theta = \beta_e l - \beta_o l$ and by superposition, we can obtain the relationship between the output voltage b_2 and b_3 and the input voltage a_1 [32]:

$$b_2 = \frac{a_1}{2}\angle(-\beta_e l) + \frac{a_1}{2}\angle(-\beta_o l) = a_1 \cos\frac{\Delta\theta}{2}\angle\left(-\beta_o l - \frac{\Delta\theta}{2}\right) \tag{2.14}$$

$$b_3 = \frac{a_1}{2}\angle(-\beta_e l) - \frac{a_1}{2}\angle(-\beta_o l) = -j a_1 \sin\frac{\Delta\theta}{2}\angle\left(-\beta_o l - \frac{\Delta\theta}{2}\right) \tag{2.15}$$

From (2.14) and (2.15), it can be seen that the output signals are always 90° out of phase regardless the length of the coupling region and by extension, independent of

frequency within the operational band of the waveguide. However, for 3 dB coupling, the length of the coupling region l, must be tuned such that $\Delta\theta = \pi/2$. Theoretically, port 4 is isolated as the analysis presented here neglects the even mode mismatches from discontinuities at the common walls on both ends of the coupling region [32]. Some form of matching components such as capacitive domes [32] or inductive side-wall discontinuities [7] are therefore required to mitigate the effects of even mode reflections.

Variations of the short-slot coupler have also been implemented using SIW [33–35], HMSIW [36], and RHMSIW [16], the former two topologies are shown in Fig. 2.15 which again showcases the significant footprint reduction of HMSIW devices over conventional SIW. RHMSIW short-slot couplers will be discussed in Chapter 3 with greater detail.

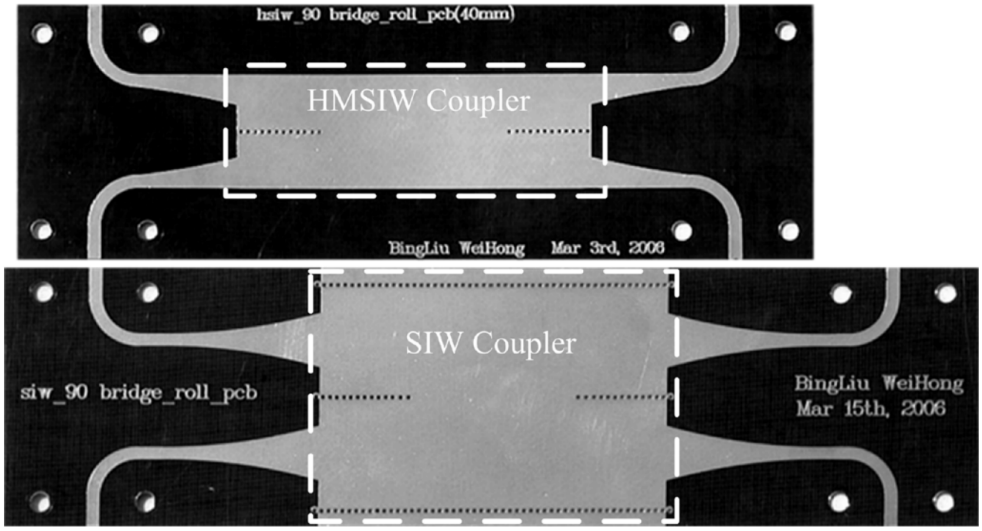

Figure 2.15: A size comparison of fabricated SIW and HMSIW 3 dB couplers for operation between 10.4 to 11.9 GHz. [36] © [2007] IEEE

2.1.6 Other Waveguide Miniaturization Techniques

In addition to HMSIW and RHMSIW, there are additional techniques that have been developed by researchers in recent years for waveguide miniaturization. Folded RHMSIW (FRHMSIW) miniaturizes RHMSIW further by folding the capacitive ridge

under the waveguide channel and offers a 25% increase in the miniaturization provided by RHMSIW over SIW [37]. FRHMSIW has also been used for resonant cavities and filter applications along with its further miniaturized quarter-mode counterpart (FRQMSIW) [38, 39]. However, due to the field configuration of the transverse plane in FRHMSIW, the structure is unsuitable for applications in short-slot couplers.

Using a different approach to the techniques previously described, evanescent mode transmission poles have been used to operate full-mode SIW structures below their normal cutoff frequencies, effectively miniaturizing the waveguide. Multipole filters have been implemented using evanescent mode SIW technology thus far [40–42]. The use evanescent-mode waveguide technology to design compact, low-loss, high isolation reconfigurable switches will be discussed with greater detail in Chapter 5.

2.2 Beamforming Systems and Components

Another way to compensate for the higher path loss at high transmission frequencies is to increase the gain of the transceiver by using more directive antennas or by combining radiating elements into an array, but by doing so, the field-of-view of the transceiver will be reduced. In order to provide adequate coverage, the shape/direction of the array's radiating beam of the array must have the ability to be dynamically altered. One way this can be achieved, is by physically rotating the array using motors. However, there are limitations on the lifetime, reliability, and speed of mechanical rotors which makes them impractical for use in high-speed mobile communication. Alternatively, the transceiver beam can be manipulated electronically by dynamically adjusting the phase of signals passing through each array element or by switching antenna elements oriented in different directions on and off, solutions collectively known as beamforming.

2.2.1 Beamforming Architectures

Industry and academia defines three main beamforming architectures: analog, digital, and hybrid. The block diagrams presented in Fig. 2.16 illustrate the transmitter side of these three architectures. Analog beamforming networks have the most simple architecture, using the fewest number of digital-to-analog converters (DAC), filters, mixers, and amplifiers, collectively known as RF chain components. However, the frequency dependence of the antenna elements and phase shifting frontend are fundamentally frequency dependent components and the main lobe of the radiated signal may swerve with frequency. Furthermore, analog beamforming systems will generally only support a single data stream [43, 44].

In contrast, digital beamformers address the beam swerve issue by adjusting the phase and amplitude weightings of the digital signals for all frequencies inside the baseband processor before outputting them to each RF chain. Furthermore, digital beamformers have the advantage of communicating with several data streams simultaneously. However, this digital beamformers are much more complex systems, requiring a separate RF chain for each array element, and costs can be prohibitive for widespread deployment at mmWave frequencies (and beyond) where components such as power amplifiers and DACs - as well as analog-to-digital converters (ADC) for the receiver chain - are significantly more expensive. Therefore, digital beamformers are generally only proposed for sub-6 GHz 5G bands [43, 44]. Digital beamformers are also known to have high power consumption, with a recent study showing a near threefold difference over a reference analog system [45].

To allow several simultaneous data streams in a multiple-input-multiple-output (MIMO) configuration while also minimizing the number of expensive RF chain components, a analog and digital "hybrid" architecture can be used as depicted in Fig 2.16(c). In this architecture, both the digital and analog components of the system can be configured to perform beam steering operations, allowing for the potential to

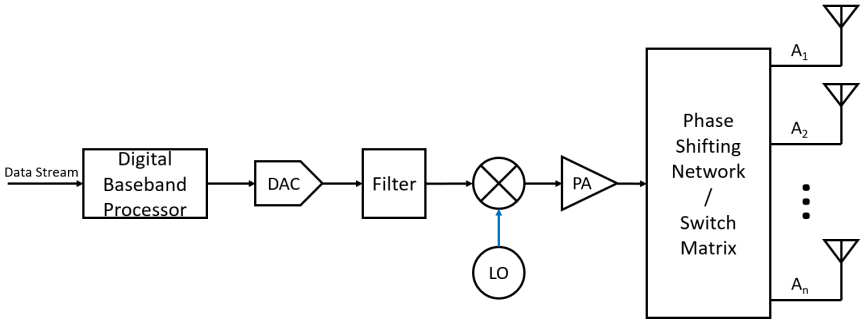

(a)

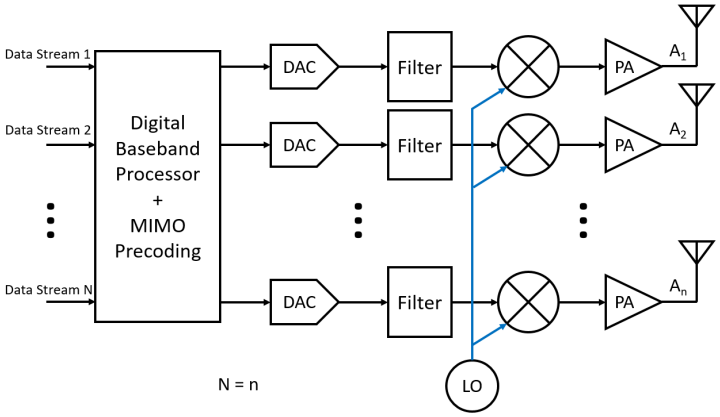

(b)

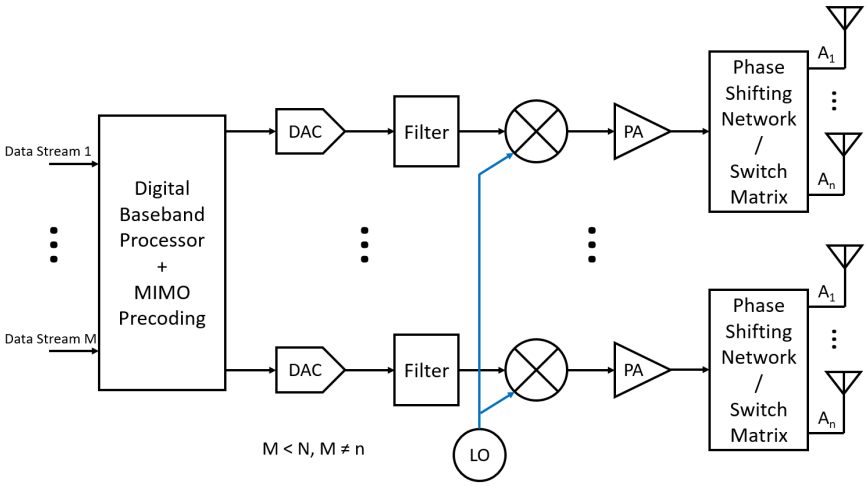

(c)

Figure 2.16: Block diagrams of the three main beamforming architectures: (a) analog; (b) digital; and (c) hybrid.

eliminate analog phase shifters all together in favour of passive selective beamformers such Butler matrices and Rotman lenses [43, 44].

Regardless of whether a purely analog or hybrid architecture is used in mmWave beamforming, it is clear that the design of phase shifting and switch matrix front-ends are critical for enabling analog and hybrid beamformers for the next generation of high-frequency communication base stations which will be the main focus for the remainder of this thesis.

2.2.2 Waveguide and Integrated Circuit Phase Shifters

The fifth generation of wireless communication (5G) seeks to vastly improve the data transfer rate and availability of mobile networks using various innovative techniques. One such technique is the implementation of massive MIMO antenna arrays with beamforming in millimeter-wave as well as sub-6 GHz bands [46]. A key component in beamforming networks are variable phase shifters which allow the phase of each antenna element feed – and by extension the direction of the antenna radiation pattern – to be manipulated.

In the previous section, it was already shown that by using the transverse resonance technique, and capacitively loading the open side of the HMSIW with a continuous ridge, the width of the HMSIW channel can be reduced up to 55% while simultaneously reducing the radiation loss of the waveguide [16].

Reflection phase shifters based off of SIW quadrature hybrid couplers have been successfully demonstrated [47] and one using HMSIW technology in [48], illustrated in Fig. 2.17. However, reflection phase shifters suffer electrically large footprints due to the length of the coupling region which is generally greater than a guided wavelength at the center frequency.

Although ridged half-mode SIW (RHMSIW) technology reduces the channel width drastically, it has little to no effect on the electrical length given the same cutoff frequency as can be seen in Fig. 2.10. As a result, developing reflection phase shifters based on the RHMSIW quadrature couplers presented in [16] may prove to be impractical and difficult to integrate in large scale phased antenna arrays.

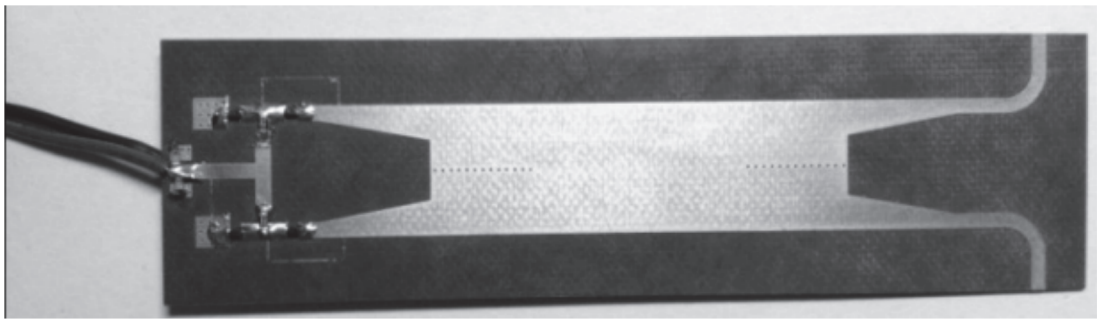

Figure 2.17: A photograph of a HMSIW reflection phase shifter operating in the 12 to 14 GHz frequency band. [48] © [2012] IEEE

In [49] it was shown that the phase of a HMSIW transmission line can be tuned by varying a periodic capacitive loading across the open edge of the waveguide using varactors. A layout of the device proposed in [49] is presented in Fig. 2.18:

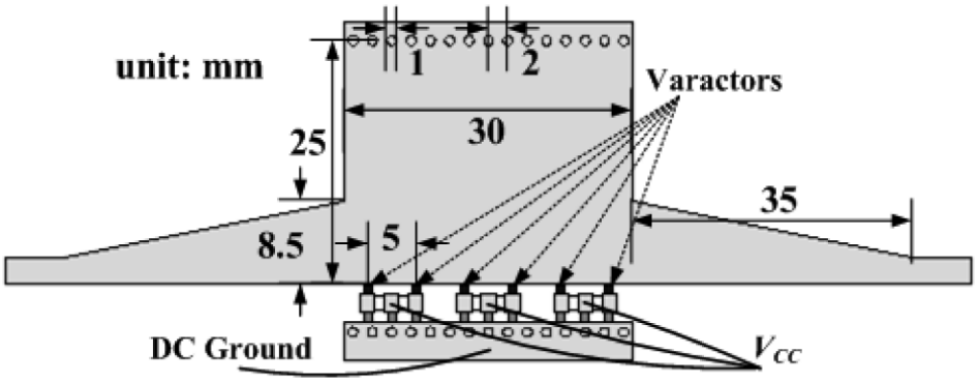

Figure 2.18: Layout of a HMSIW phase shifter using periodic tunable capacitive loads. [49] © [2010] IEEE

While providing less tuning range than the reflection phase shifter in [48], the periodically loaded HMSIW design in Fig. 2.18 offered a much larger bandwidth in a more compact footprint. Chapter 3 and discusses a miniaturized version of this design using RHMSIW.

However, low-loss varactors can be difficult to construct at millimeter-wave frequencies, with a relatively recent state-of-the-art MOS varactor in literature developed on a 43 nm CMOS process only being able achieve a quality factor of 8 at 50 GHz [50].

In literature, a variety of other phase shifter platforms exist for mmWave and

sub-THz operation such as CMOS / HBT transistor-based, MEMS-based devices. However, many switched CMOS phase shifters report very high insertion losses in the W-Band (75 to 110 GHz), with a single bit phase shifter having losses on the order of 5 dB [51], and 4-bit phase shifters having losses in excess of 15 dB [51, 52]. A recent active continuous CMOS phase shifter for operation at 40 GHz also reports a total gain of -7 dB [53]. Furthermore, CMOS phase shifters are known to have poor linearity with typical 1-dB compression points on the order of 15 dBm or less [51, 53, 54].

MEMS-actuated phase shifters on the other hand, have been shown to have much lower IL compared to CMOS phase shifters [55, 56], and have been shown to have the ability to be integrated with waveguides up to sub-THz frequencies with < 5 dB IL [57, 58]. However, MEMS actuators are known to have slow tuning speeds, with the some of the fastest devices operating on the order of 200 kHz to 2 MHz (0.5 to 5 µs) [59].

These challenges open up use cases for switched beamforming networks such as Rotman lenses and Butler matrices which are generally easy to fabricate, low-cost, and have lower losses than active phase shifters owing to the fact that they are purely passive networks [60].

2.2.3 Passive Discrete Analog Beamforming Networks

Over the past decades, phased array antennas have become a vital technology for a variety of wireless applications from radar [61] to beamforming for 5G networks [46]. A phased array involves the manipulation of the progressive phase difference between individual antenna elements in order to obtain array patterns radiating in a desired direction [62]. The phase manipulation can be achieved with the use of phase shifters or through beamforming networks such as Rotman lenses [63, 64] or Butler matrices [65, 66].

Rotman lenses and Butler matrices are discrete beamforming networks where the

differential phase between each element is manipulated through fixed steps depending on which input port is excited; the former operates on optical principles whereas the latter consists of a series of quadrature couplers, crossover lines, and delay lines [65]. While Rotman lenses have the advantage of being true-time delay (TTD) devices [67], they have the disadvantage of having high spillover losses when a limited aperture size is required [68]. Furthermore, work has been published showing that with some modifications to the hybrid couplers in Butler matrices, a relatively flat phase difference response between output ports across a wide bandwidth [69]. Work has also been published that demonstrates the integration of phase shifters with Butler matrices for continuous beam-steering [70].

In [71], the potential of HMSIW technology for large-scale system integration has been demonstrated through the implementation of a miniaturized 4×4 Butler matrix at 10 GHz. However, since the design in [71] is implemented using HMSIW, difficulties arise in the transition from the open edge of one waveguide to the open edge of the other which forces the design to instead transition back into a full-mode SIW in its crossover stages, thereby limiting the full potential of miniaturizing the structure. This actually resulted in less miniaturization when compared to a multilayer folded-SIW design [72].

Alternatively, researchers have proposed discretely switched omnidirectional MIMO arrays. Originally proposed for WLAN applications, due to the simple, energy efficient, and compact nature of their feeding networks [73, 74], recent years have shown renewed interest in the architecture for microwave and mmWave 5G networks. Such arrays do not require the use of phase shifters or beamforming networks, and high gain array elements are instead directly connected to or disconnected from the transceivers via multi-throw switches [75–77]. Regardless, of whether Butler matrices or switched omnidirectional arrays are used in 5G and 6G transceivers, it is clear that efficient switches are a key enabling technology.

2.2.4 Photoconductive Evanescent-mode Waveguide Switches

As fundamental components of transceiver front-ends, RF switches enable functionality including reconfiguration [78], antenna transmit-receive switching or beam-switching [68, 79, 80], or band and channel selection in multiband systems. While a variety of mmWave switch technologies using electromechanical rotors and PIN diodes currently exist, there are generally major trade-offs between power handling, size, and speed [81–85]. Electromechanical waveguide switches offer the highest continuous wave power handling. However, they have switching speeds on the order of several milliseconds which may significantly increase the latency of communication systems [82]. Additionally, the use of electromechanical rotors require large, heavy packaging and are less reliable than solid-state components, having a service life of around 250,000 cycles [83]. PIN diode switches on the other hand offer switching speeds on the order of nanoseconds [84], and have exceptional power handling at lower RF bands [86]. However, at mmWave frequencies, PIN diodes lose their continuous wave power handling, suffer large insertion losses, poor signal isolation, and have low linearity [84].

Researchers have also explored the use of the photoconductive effect in semiconductors for a variety of integrated microwave engineering applications including switches [87, 88], variable attenuators [89], and tunable filters [90]. Photoconductive switches have the benefit of relatively high power handling and excellent linearity [91] while also offering fast switching speeds and low insertion losses with the right choice of material and optical power [92, 93]. Moreover, photoconductive switches have the additional benefit of bias networks completely isolated from the RF path, further improving insertion loss and linearity. Within waveguide structures, photoexcitation can be used to alter the properties of high resistivity silicon posts, changing them from a dielectric to a conductor. When the light source is switched off, the dielectric properties of the posts are restored, effectively allowing microwave signals to be

dynamically redirected within the waveguide channel [94–96]. As will be determined from the studies in this thesis, photoconductive silicon waveguide switches offer an excellent compromise between the switching speed of PIN diode-based solutions and the high-power handling capabilities of electromechanical waveguide switches while also operating at mmWave frequencies. These light-activated switches will open up entirely new use cases for reconfigurable and multifunctional mmWave technology by offering high-speed and high-power handling with low ON-state insertion loss and high OFF-state isolation simultaneously within the same device.

The advantages of photoconductive switch technology in both planar and waveguide platforms has been thoroughly documented by the authors [92, 94–99]. In [92], a DC to 7 GHz reflective series switch constructed in a microstrip platform was shown to be able to handle 35 W of RF power, with an absorptive single pole double throw (SPDT) switch implementation demonstrated in [98]. More recently in [99], it was shown that up to 100 W of RF power can be handled without degradation in loss or isolation, while also demonstrating hot switching up to 30 W. The first ever DC to 110 GHz photoconductive switch in coplanar-waveguide (CPW) technology was also demonstrated in [97].

While integrating mechanically-tuned posts within waveguide switches and filters has been demonstrated [100], the authors presented in [94] the first waveguide switch incorporating photoconductive silicon posts within the waveguide channel as the switching element fabricated using silicon bulk micromachining at mmWave frequencies. Silicon bulk micromachining has the advantages of relatively simple planar integration with very tight feature tolerances on the order of a few micrometers, and has been demonstrated to successfully fabricate waveguide structures that operate up to sub-THz frequencies [101]. Furthermore, silicon micromachining allows the waveguide channel and photoconductive silicon switch posts to be fabricated monolithically with the same process [94]. In [95], silicon micromachined photoconductive waveguide switch technology was further developed by demonstrating that the optical power re-

quirement for achieving a high isolation can be significantly reduced by fabricating a switch topology with two silicon posts inside an evanescent-mode (EVA) waveguide channel.

Chapter 3

Sub-6 GHz RHMSIW Butler Matrix and Phase Shifter

To form the theoretical foundation of developing microwave / millimeter-wave waveguide beamforming networks we first investigated the RHMSIW interconnect at a low-frequency 3.5 GHz 5G band. RHMSIW have the advantage of having the bulk of its electric field concentrated on an open side (see Fig. 2 5) allowing relatively simple integration with tuning elements. The reduced height of the open side helps to minimize radiation loss and has the additional benefit of occupying less design space than equivalent full-mode SIW devices. While the devices presented in this chapter were developed primarily for proof-of-concept purposes, a millimeter-wave version of the Butler matrix presented in the following sections is currently in development and the concept of periodically loaded phase shifters will be applied to future THz designs. The phase shifter design presented in this chapter is a miniaturized tunable phase shifter constructed using RHMSIW technology for operation over three sub-6 GHz 5G frequency bands [102] between 2.5 and 3.7 GHz. Periodic varactor loading is applied across the waveguide, modifying the overall phase velocity of the fundamental quasi-$TE_{0.5,0}$ propagation mode, allowing one to dynamically tune the amount of phase incurred within the transmission coefficient S_{21}. Furthermore, it will be shown in this chapter that the open edge of one RHMSIW line can be connected to the open edge of another RHMSIW line through the capacitive ridge with minimal reflected

power and loss. This chapter also presents two novel designs of 90° bends and the detailed design procedure of each component in the Butler matrix using RHMSIW technology at 3.5 GHz.

3.1 Principle of Operation

3.1.1 Butler Matrix

The Butler matrix is a beamforming network whose topology consists of three main components: quadrature hybrid (QH) couplers, crossover lines, and phase delay lines. A general block diagram of a 4 × 4 Butler matrix is shown in Fig. 3.1. For the remainder of this thesis, the input ports will be defined as ports 1 to 4 and the output ports as 5 to 8.

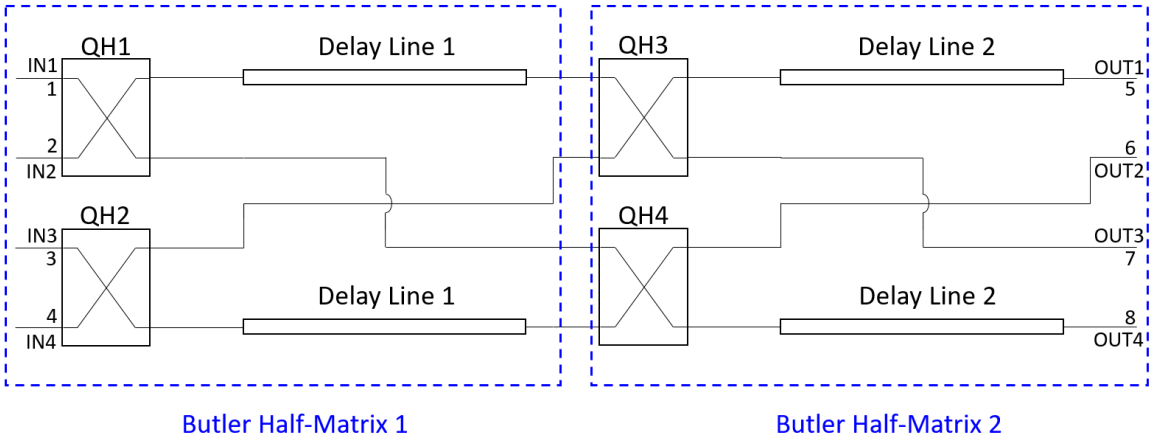

Figure 3.1: Generic block diagram of a 4 × 4 Butler matrix. The design consists of quadrature hybrids, crossover lines, and phase delay lines and can be divided into two halves that are identical with the exception of the delay line dimensions.

The delay lines must be designed such that they incur the same amount of phase as the crossover lines; furthermore, delay line 1 must incur an additional 45° of phase on top of compensating for the phase of the crossover lines. The result is that when port 1 is excited, the signal entering the top port of QH3 leads the signal entering the top port of QH4 by 45° and the other inputs are isolated. Finally, each successive port lags the preceding port by 45° at the output end. When port 2 is excited, the

signal entering the top port of QH4 leads the signal entering the top port of QH3 by 135° resulting in each successive output port leading the preceding port by 135°. Since the Butler matrix is a symmetric device, ports 3 and 4 are just mirror images of ports 2 and 1 respectively, and phase progression at the output ports is identical in the opposite direction to the cases described above. To implement the crossover lines in SIW Butler matrices, it is common in literature to make use of 0 dB short-slot couplers [65, 71, 103].

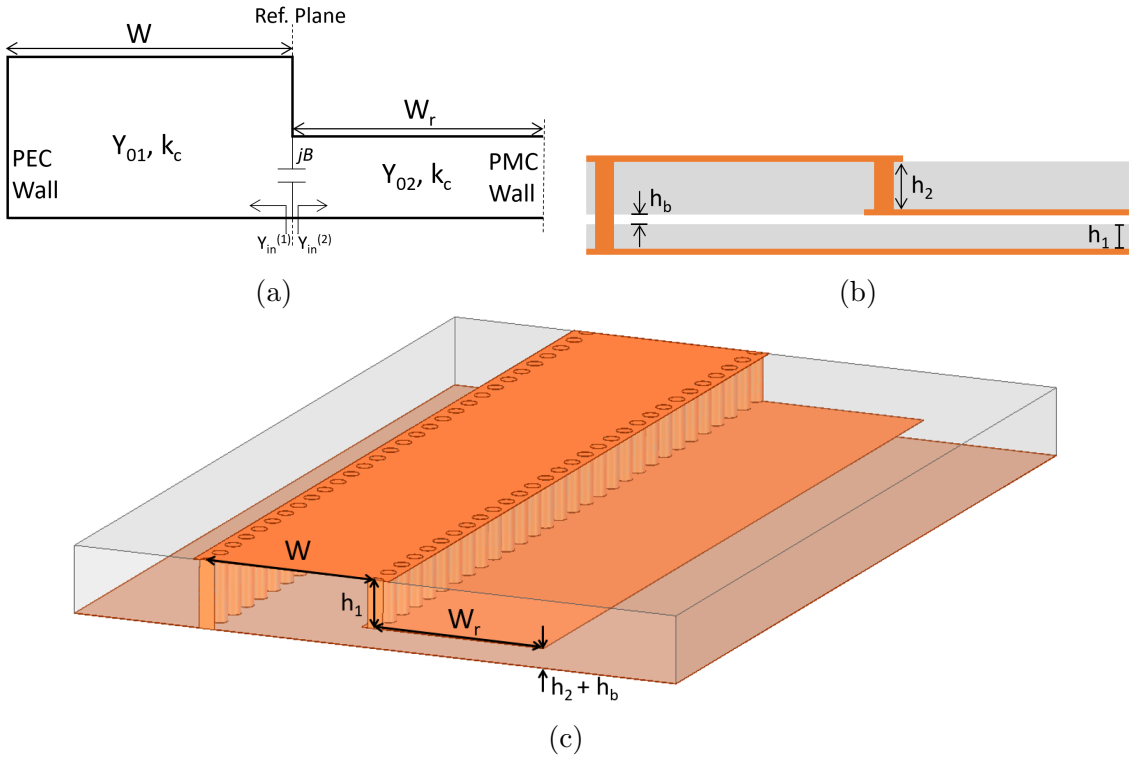

Figure 3.2: CAD drawings of RHMSIW. (a) Transverse model of a RHMSIW. (b) The substrate stackup of RHMSIW fabricated on PCB technology; gray represents the RO3003 material and white for the RO4450F Bondply™ bonding material. h_1 = 0.254 mm, h_2 = 0.762 mm, and h_b = 0.1016mm. (c) 3D model of a RHMSIW line.

3.2 Butler Matrix Design

The proposed design was fabricated on a multilayer Rogers RO3003 substrate, the stack-up is illustrated in Fig. 3.2(b). First, the blind vias are drilled and plated on the 30 mil substrate. Then the conducting layer containing the capacitive ridge is

patterned and bonded to the 10 mil substrate using the 4 mil RO4450F Bondply^{TM}. Finally, the through vias are drilled and plated, and the top conducting layer is then patterned. The sidewall via diameters are 0.5 mm with 0.7 mm pitch. The design details, simulated, and measured results of each subcomponent will now be discussed below. Note that any discrepancies between simulated and measured results are most likely due to loading from the soldered coaxial connectors, and fabrication / substrate tolerances.

3.2.1 Quadrature Hybrid

The quadrature hybrid coupler in the proposed design is based off the Riblet short-slot waveguide coupler topology as discussed in Chapter 2. The RHMSIW short-slot coupler therefore has the narrowest channel to date. A capacitive "dome" was introduced in the center of the coupling region to reduce reflections and improve the overall matching and isolation of the ports [32]. The diameter of the capacitive dome (d_cap) and the RHMSIW transverse dimensions (W and W_r), and coupling region length (L_C) need to be fine-tuned such that the power split, return loss, and isolation between ports are all satisfactory at the frequency of interest. The final dimensions of the quadrature hybrid in the proposed design are shown in Fig. 3.3 and the simulation results of the coupler from ANSYS HFSS and measured results are plotted in Fig. 3.4. Between 3.153 and 3.588 GHz, the measured coupler has less than 1 dB coupling imbalance, less than 0.54 dB insertion loss and greater than 21 dB isolation. The simulated phase difference between ports 3 and 2 ($\angle S_{31} - \angle S_{21}$) plotted in Fig. 3.5 shows that there is less than a 1° deviation from 90°when the quadrature hybrid is operated reasonably above the cutoff frequency.

3.2.2 Crossover Coupler

To avoid the use of multilayer crossover lines, the proposed design makes use of another coupler to implement the crossover stage. When an input port is excited,

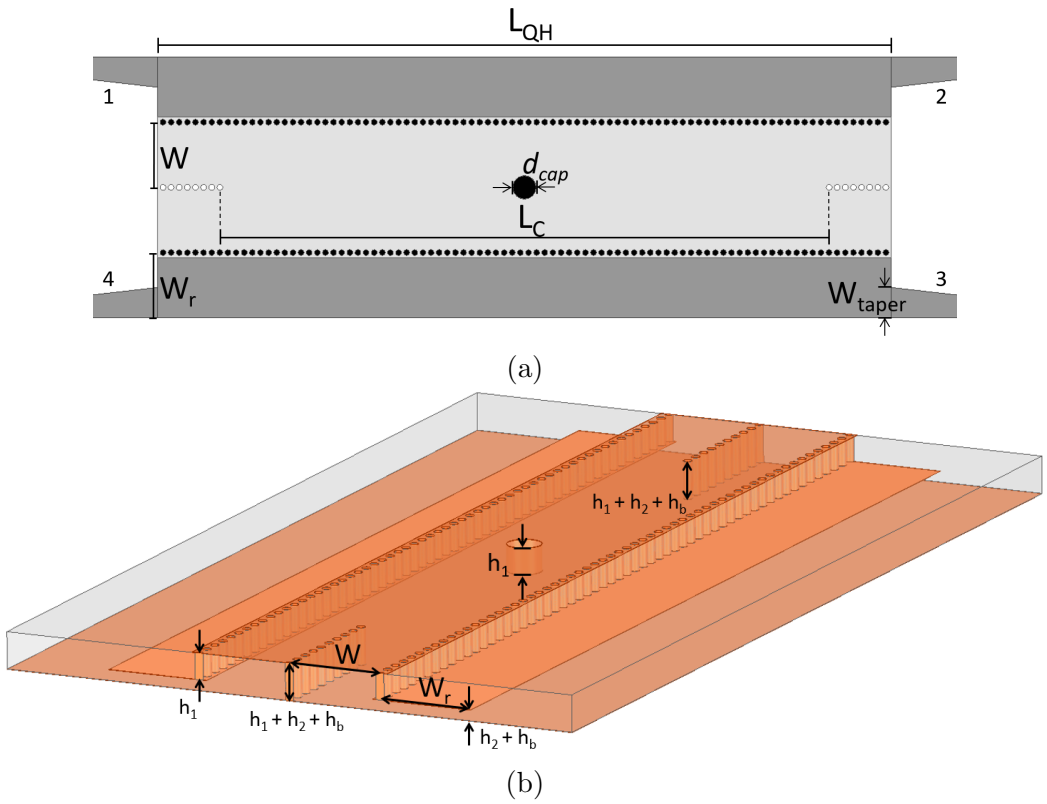

Figure 3.3: The CAD drawings of the quadrature hybrid used in the proposed Butler matrix design. (a) A bird's-eye 2D layout. Microstrip transitions have been added to all ports for the purpose of characterizing the standalone component. $L_C = 52.5$ mm, $d_{cap} = 2.0$ mm, $L_{QH} = 63.2$ mm, $W = W_r = 5.6$ mm, and $W_{taper} = 2.6$ mm. For all layouts in this chapter, black and white circles represent blind and through vias, respectively. The top and embedded ridge conducting layers are shaded in light and dark grey, respectively. (b) A 3D model. The substrate an top metal layer has been rendered semi-transparent.

the adjacent port and the through port should be isolated while transmission to the coupled port should ideally be 0 dB. This 0 dB crossover coupler can be seen as a cascade of two 3 dB quadrature couplers [104] and the resulting length of the coupler is approximately double of the quadrature hybrid.

Keeping W and W_r obtained from the previous section, the return loss, isolation, and coupling were tuned by varying the length of L_C, and the diameter of the three evenly-spaced domes. The layout of the crossover coupler is shown in Fig. 3.6 and the simulation and measured results in Fig. 3.7. The coupler has less than 0.8 dB insertion loss and greater than 20 dB isolation between 3.320 and 3.629 GHz.

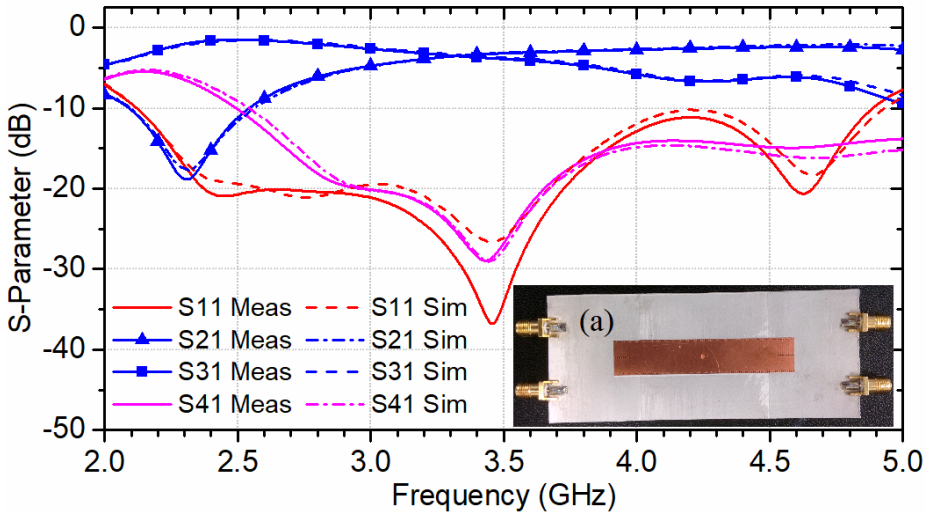

Figure 3.4: Simulated and measured S-parameters of the standalone QH coupler. (a) Photo of the measured QH coupler.

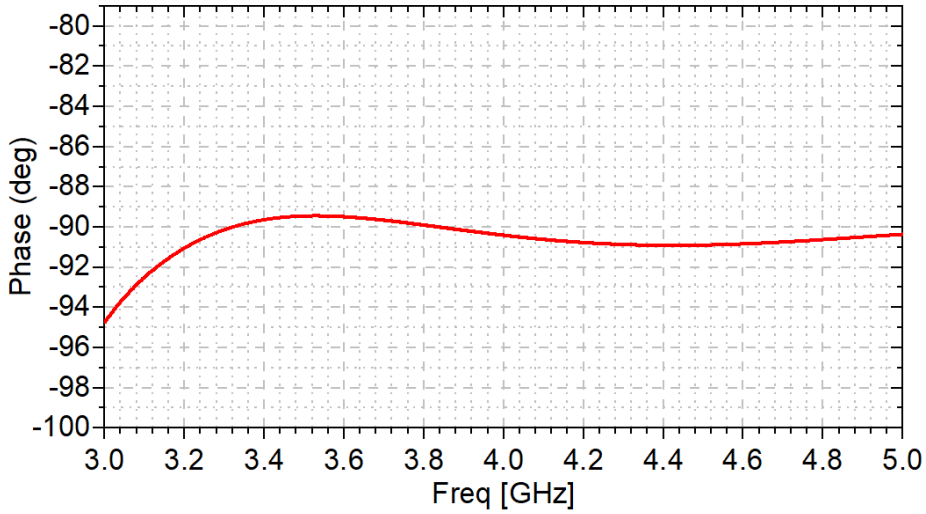

Figure 3.5: The simulated phase difference between port 3 and port 2 of the RHMSIW quadrature hybrid.

3.2.3 Asymmetric Ridge-to-Ridge Transition

Since half-mode waveguides are asymmetrical structures, the adjacent output ports of QH1 and QH2 do not mate directly to the input ports of the crossover coupler if all structures are in half-mode. The solution proposed in [71] implements the crossover couplers as full-mode SIW structures and the half-mode QH ports directly feed into the full-mode structure. However, this solution limits the maximum achievable minia-

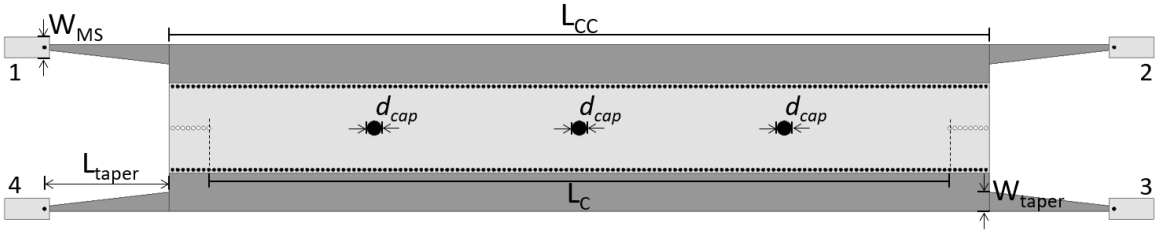

Figure 3.6: Layout of the 0-dB crossover coupler used in the proposed design. The capacitive domes are blind vias of diameter $d_{cap} = 2.0$ mm represented as black circles, and are evenly spaced across the coupling region of length $L_C = 100.1$ mm. The total length of the coupler is $L_{CC} = 110.8$ mm. The microstrip transitions shown here have dimensions $W_{MS} = 2.8$ mm, $W_{taper} = 2.6$ mm, and $L_{taper} = 13.75$ mm and are the same for all other microstrip fed components in this chapter.

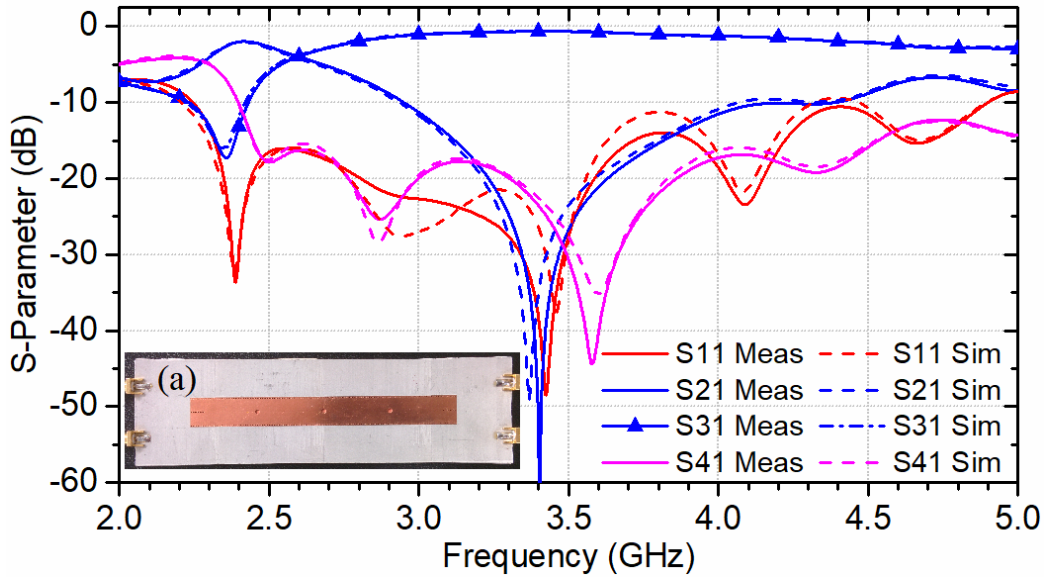

Figure 3.7: Simulated and measured S-parameters of the standalone crossover coupler. (a) Photo of the measured crossover coupler.

turization of the full-systems if a similar solution were to be applied to RHMSIW technology. Instead, we propose a solution where both the QH couplers and the crossover couplers be constructed in the RHMSIW topology.

Since the bulk of the electric field in the fundamental quasi-$TE_{0.5,0}$ mode is concentrated in the ridge, an assumption can be made that only a minimal amount of power is lost due to reflections and radiation when only the ridges of the two stages of couplers are mated with each other. However, to ensure optimal performance, double-edged tapers were introduced on the ridge layer centered at the interface between the

two coupler stages. Fig. 3.8 shows the layout of a ridge-to-ridge connected test line with and without the described tapers, and a reference RHMSIW transmission line of the same length. The length of the tapers L_{rtaper} and width W_{rtaper} can be tuned in simulation until the return loss is maximum at the band of interest.

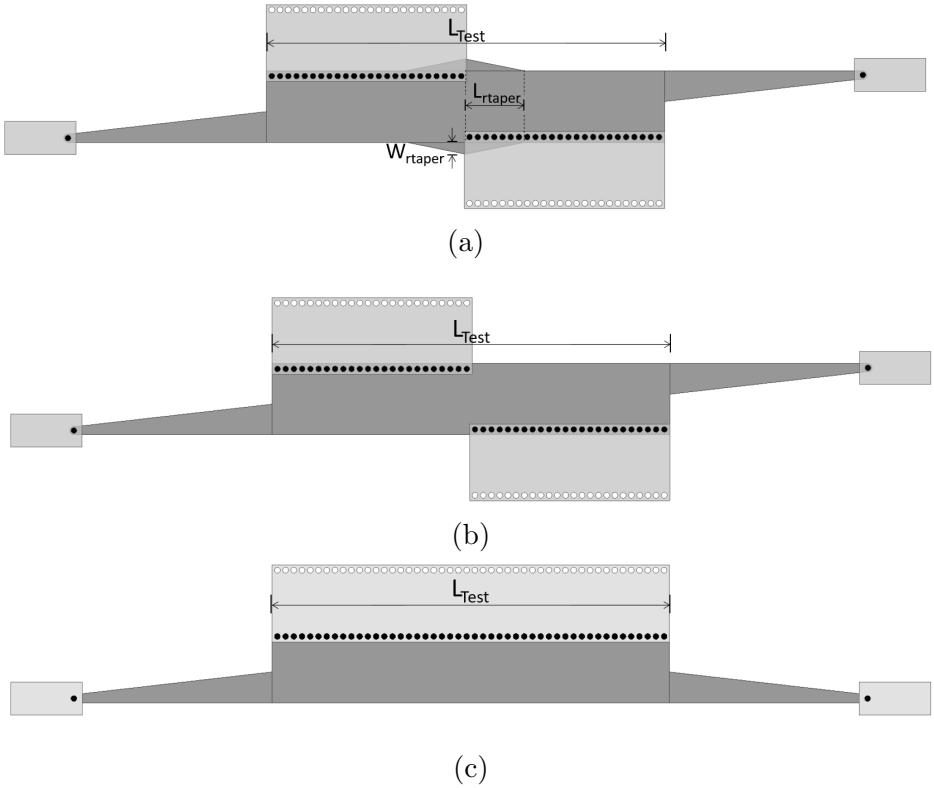

Figure 3.8: Test lines for the characterization of the proposed asymmetric ridge-to-ridge transition. (a) Tapered transition. (b) Untapered transition. (c) Reference line of the same physical length (L_{Test} = 33.8 mm) as the preceding test lines.

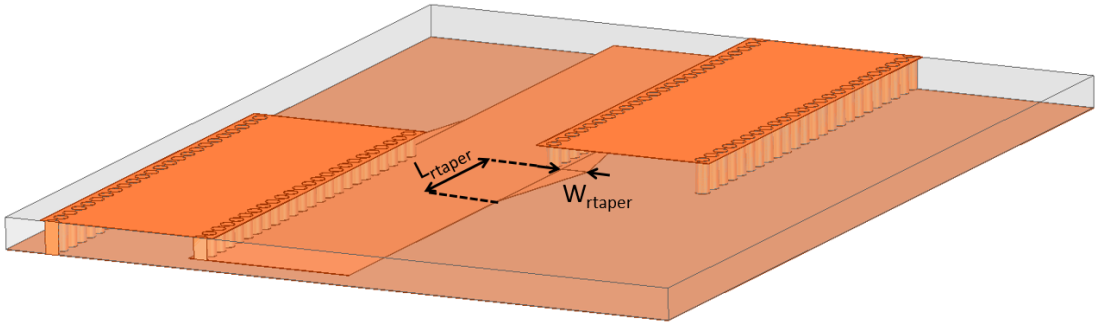

Figure 3.9: A close-up 3D model illustrating the tapered asymmetric ridge-to-ridge transition.

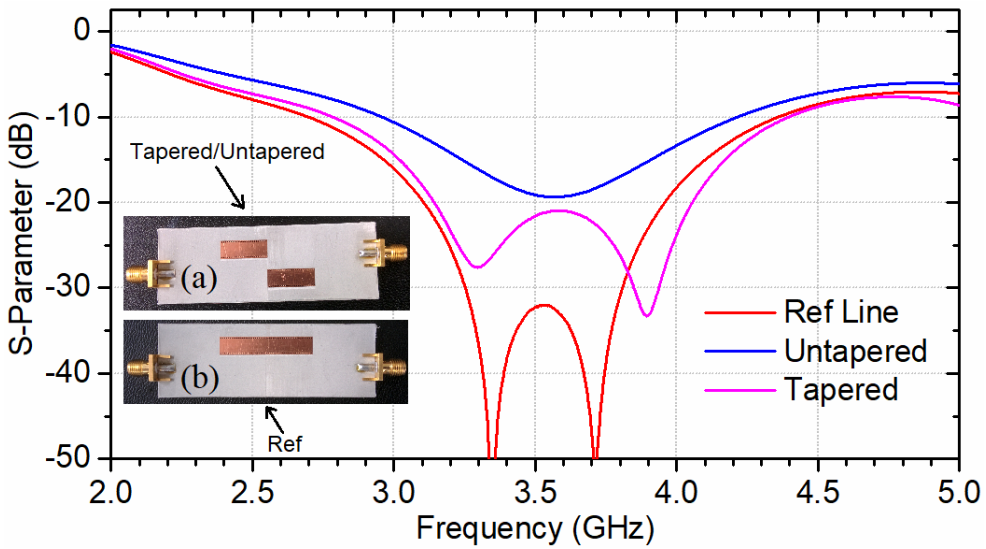

Figure 3.10: Measured return loss comparison of the ridge-to-ridge transition test lines and a reference line of the same length. (a) Photo of ridge-to-ridge connected test lines. (b) Photo of reference line.

A 3D model illustrating the asymmetric transition with tapers is shown in Fig. 3.9, and a comparison of the measured S_{11} responses of the three test lines are plotted in Fig. 3.10. The return loss of the test line without a taper is 20 dB with 0.2 dB insertion loss at 3.51 GHz while the test line with the optimal taper dimensions of L_{rtaper} = 5.0 mm and W_{rtaper} = 1.0 mm has a return loss of 30 dB with 0.16 dB insertion loss. The performance of the tapered line is comparable to the reference line's 35 dB and 0.16 dB of return and insertion loss, respectively. In simulation, it can be shown that the reference line incurs (lags) an additional 3.05°of phase compared to the tapered ridge-to-ridge transition, this must be compensated for in the delay lines that will be described in section 3.2.5.

3.2.4 90° Waveguide Bends

The asymmetry of RHMSIW structures requires the analysis of two types of 90° bends: one where the ridge is on the outer edge of the bend, and one where it is on the inner edge.

The former case is illustrated in Fig. 3.11 where it can be seen that the return

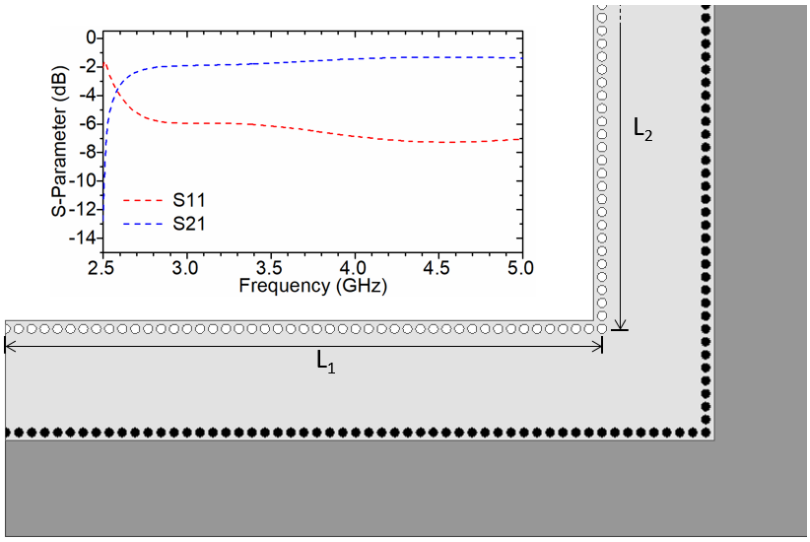

Figure 3.11: Layout and simulation results of a RHMSIW 90° bend with the ridge on the outer edge of the bend. $L_1 = L_2 = 32.2$ mm.

loss of the structure is less than 7.5 dB across the entire operational band of the waveguide. The electric field of a guided wave is maximum in the ridge structure and the 90° outer edge bend of the ridge results in increased electric field fringing which by extension, introduces capacitance to the structure. Therefore, we propose mitering the corner of the ridge to improve the return loss at the frequency of interest.

An illustration of the proposed mitre and parametric study of the S_{11} response vs varying mitre lengths is shown in Fig. 3.12. It can be seen that as the length of the mitre increases, the peak of the return loss decreases in frequency. Centering the peak return loss at 3.55 GHz was achieved in simulation by mitering a corner of lengths $L_{Corner1} = 8.7$ mm from the vertex of the bend.

For the case where the waveguide ridge is on the inner edge of the bend, the discontinuity decreases the amount of electric field fringing, resulting in impedance mismatches and reflected power. Therefore, the corner is tapered instead of mitered in order to increase fringing at the bend. The bend with the proposed taper and a parametric study of the S_{11} response with varying taper length are presented in Fig. 3.13. Similar to the previous case, the peak return loss shifts down in frequency as the physical dimensions of the taper increases.

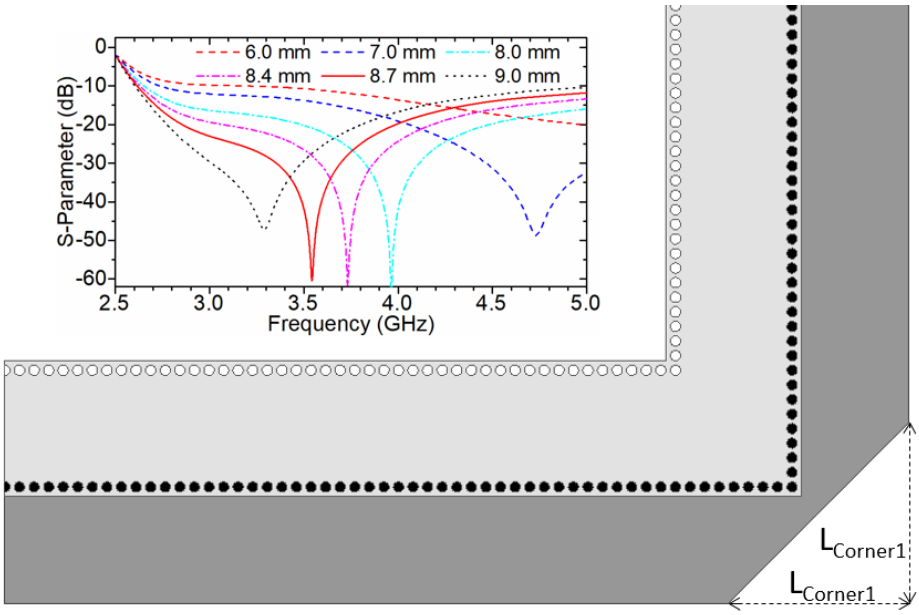

Figure 3.12: Layout and simulated parametric study of a mitered ridge 90° RHMSIW bend. The S_{11} response shifts down in frequency as the physical size ($L_{Corner1}$) of the mitre increases.

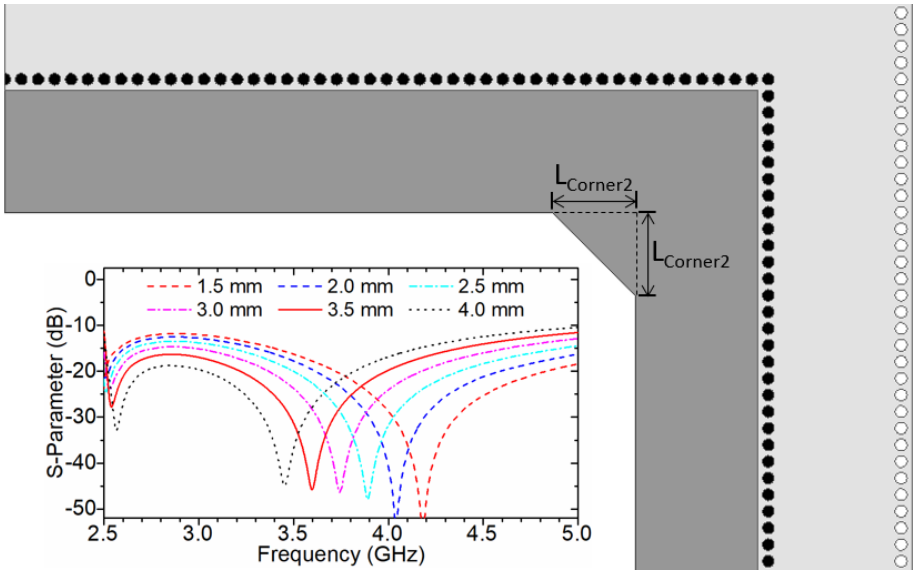

Figure 3.13: Layout and simulated parametric study of a tapered 90° RHMSIW bend with the ridge in the inner edge of the bend. The S_{11} response shifts down in frequency as the size of the taper ($L_{Corner2}$) increases.

3.2.5 Delay Lines

The 90° bends can be applied to the design of delay lines in the proposed Butler matrix design. In the second half of the Butler matrix, the outputs of the QH are

90° out of phase and this must be maintained at the output of the delay line and crossover coupler. Therefore, the phase incurred by a signal propagating through delay line 2 must be the same as a signal passing through the crossover coupler. In the first half of the matrix, the phase difference between the delay line 1 and the crossover needs to be 45°. Therefore, the delay line needs to match the crossover phase delay and incur an additional 45°. In this design, the physical horizontal lengths of the delay lines were chosen to be equal to that of the crossover coupler L_{CC}. The proposed delay line structure is illustrated in Fig. 3.14.

There are two degrees of freedom for tuning the phase incurred in the delay lines: first, through the length of the vertical sections (L_2) in multiples of the via pitch p, and then by extending the ridge width (W_{Ext}) on the upper horizontal section to fine-tune the phase delay.

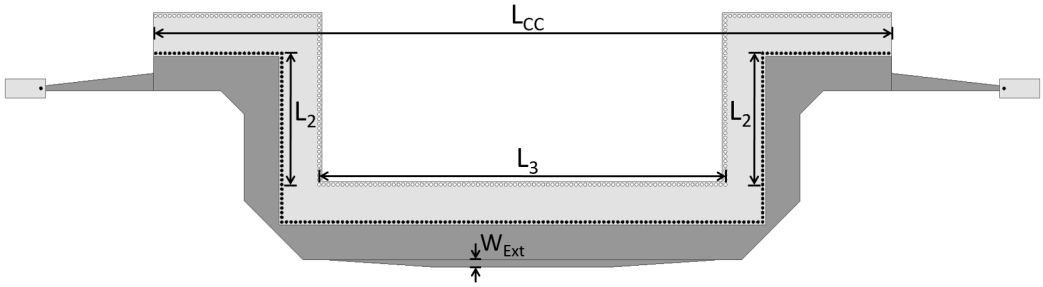

Figure 3.14: The layout of the proposed delay line design is the combination of multiple 90° RHMSIW bends described above. The total horizontal length of the delay line must be equal to that of the crossover coupler (L_{CC}). For delay line 1, DL1: $L_2 = 19.6$ mm, and $W_{Ext} = 1.1$ mm. For delay line 2, DL2: $L_2 = 16.1$ mm, and $W_{Ext} = 0.7$ mm. Finally, $L_3 = 60.9$ mm.

To minimize reflections due to discontinuities on the ridge, the extension is tapered on both ends with equal lengths of approximately $\lambda_g/4$ in the RHMSIW line (without ridge extension). The simulated and measured S-parameter magnitudes for delay lines 1 and 2 are plotted in Fig. 3.15 and their measured differential phases relative to the proposed crossover coupler in Fig. 3.6. Delay line 1 achieves less than 0.9 dB insertion loss between 3.25 and 3.7 GHz and delay line 2 has less than 1 dB insertion

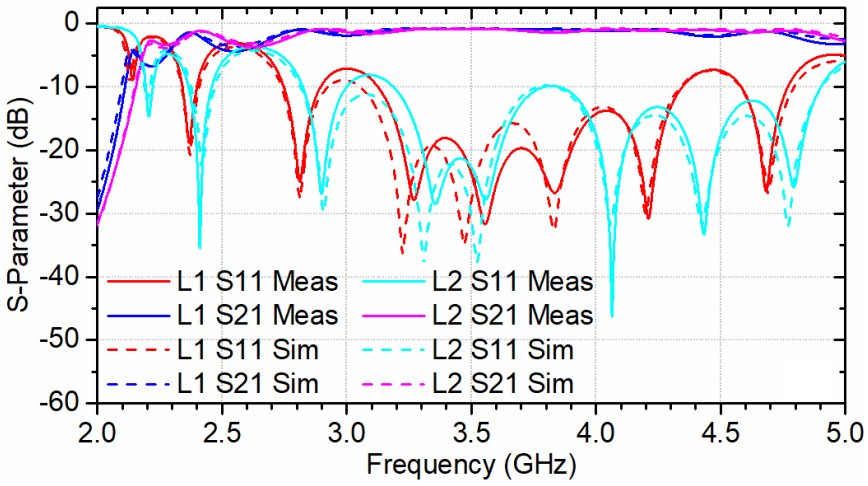

(a)

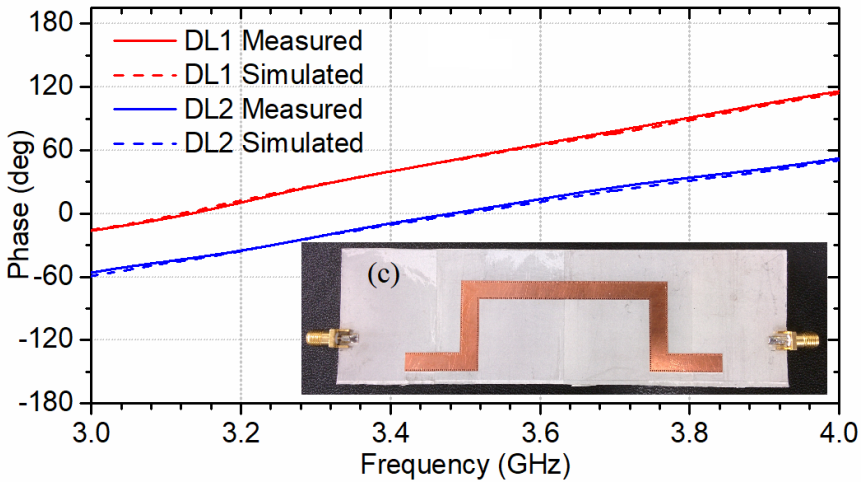

(b)

Figure 3.15: Simulated and measured results for the delay lines. (a) S_{11} and S_{21} response. (b) The differential phase response w.r.t. the crossover coupler with insert photo of a measured delay line. (c) Photograph of a fabricated delay line.

loss between 3.25 and 3.67 GHz.

3.2.6 Half Matrices

Due to the total length of the proposed design, it was more practical to fabricate the structures in two halves as shown in Fig. 3.1. The layout of a half matrix is shown in Fig. 3.16. The dimensions of both half matrices are identical with the exception of the vertical lengths (L_2) and top section ridge width of the delay lines. With excitation of port 1 or 2, there is equal power division between ports 5 and 7. In half-

matrix 1 there is a differential phase of 45°/135° between ports 5 and 7 and ±90° for half-matrix 2.

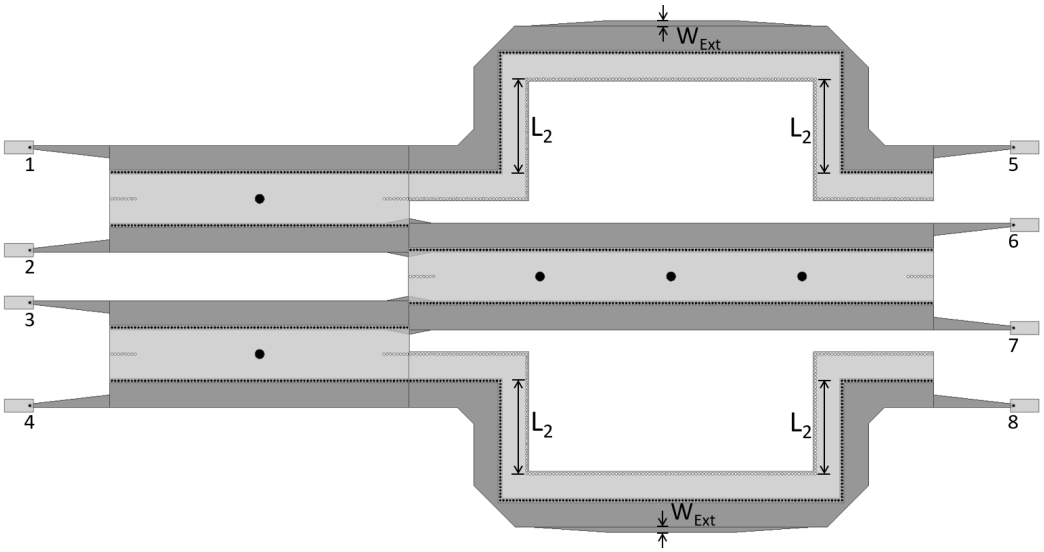

Figure 3.16: The layout of a Butler half-matrix. The two halves of the Butler matrix are identical with the exception of the delay line dimensions L_2 and W_{Ext} which are 19.6 mm and 1.1 mm, respectively for half-matrix 1, and 16.1 mm and 0.7 mm for half-matrix 2.

A comparison of simulated and measured S-parameters for half-matrix 1 and 2 are plotted in Fig. 3.17 and Fig. 3.18, respectively. In Fig. 3.19, the differential phase between the output ports of the two half-matrices are shown. Note that only the S-parameters due to port 1 and port 2 excitation are shown since the structure is symmetric. It can be seen that simulated and measured data are in good agreement.

When port 1 is excited in measurement, half-matrix 1 is able to achieve 1.35 dB insertion loss centered at 3.4 GHz and less than 1 dB coupling imbalance between ports 5 and 7 over the frequency range of 3.2 to 3.635 GHz. In half-matrix 2, the insertion loss is 1.11 dB centered at 3.427 GHz and the 1 dB imbalance band is between 3.176 and 3.805 GHz. When port 2 is excited the insertion loss of half matrix 1 is 0.942 centered at 3.412 GHz and the 1 dB imbalance band is spans 3.2 to 3.635 GHz. In half-matrix 2, the insertion loss is less than 1.07 dB and the 1 dB

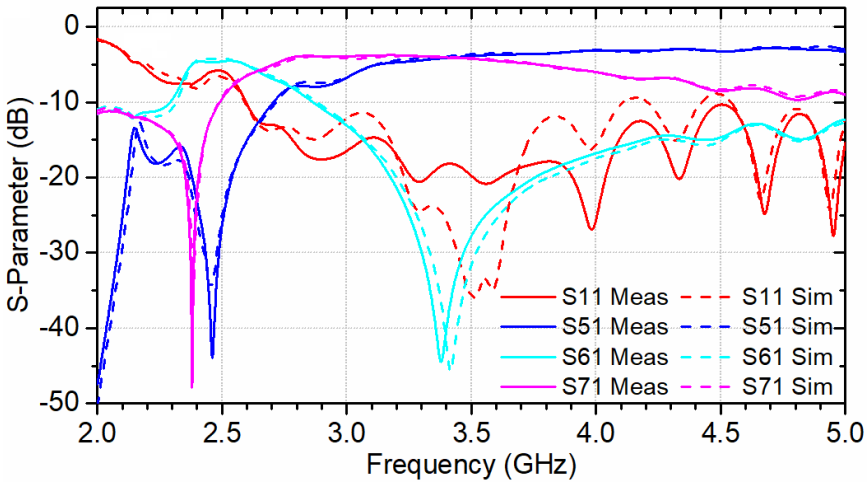

(a)

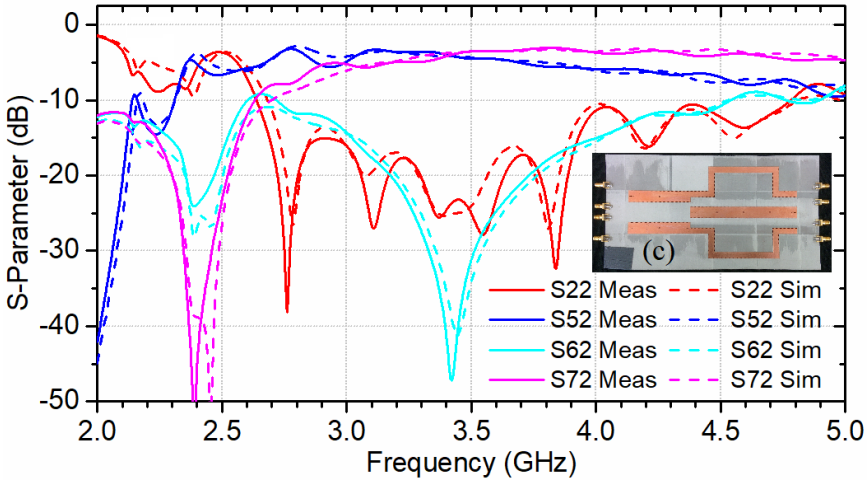

(b)

Figure 3.17: Simulated and measured S-parameters for the first Butler half-matrix. (a) Port 1 of the half-matrix is excited. (b) Port 2 of the half-matrix is excited. (c) Photo of half-matrix 1.

imbalance band is between 3.261 and 3.624 GHz.

3.2.7 Tunable Phase Shifter

A tunable phase shifter similar to the design in Chapter 3 was fabricated and characterized. A summary of the measured results is presented here. A photograph of the phase shifter's test setup is shown in Fig. 3.20. A RHMSIW is periodically loaded with ten varactors along its open side; the propagation constant of the line, and by extension the phase, is manipulated as the capacitance of the loads vary with

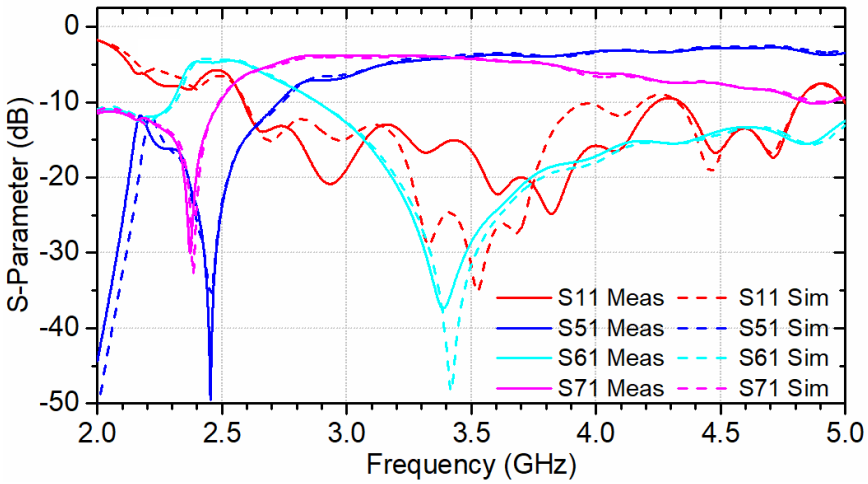

(a)

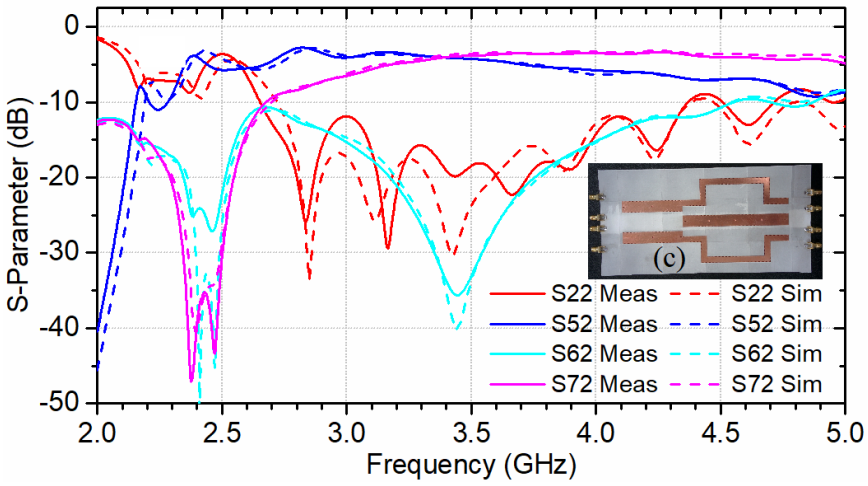

(b)

Figure 3.18: Simulated and measured S-parameters for the second Butler half-matrix. (a) Port 1 of the half-matrix is excited. (b) Port 2 is excited. (c) Photo of half-matrix 2.

the varactor reverse bias voltage.

A plot of the S_{21} phase tuning range vs DC bias voltage is presented in Fig. 3.21. The minimum insertion loss in the 3.4 to 3.6 GHz band is 0.75 dB and the reverse bias voltage was decreased until the insertion loss reaches 3.75 dB (3 dB above minimum IL) at any frequency in the band; the maximum tuning based on this condition is 116°. Additional details on the principle of operation and more simulated and measured data on this device can be found in Appendix B.

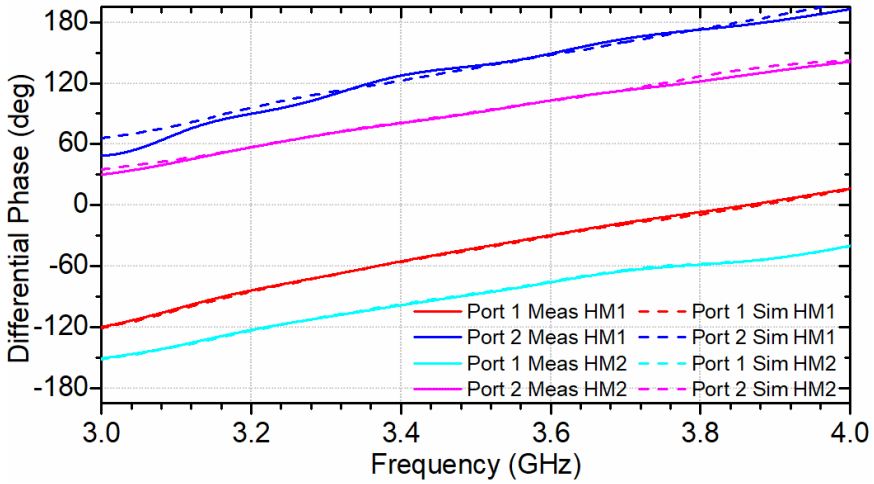

Figure 3.19: The differential phase between ports 7 and 5 when ports 1 and 2 are excited for half-matrix 1 and half-matrix 2.

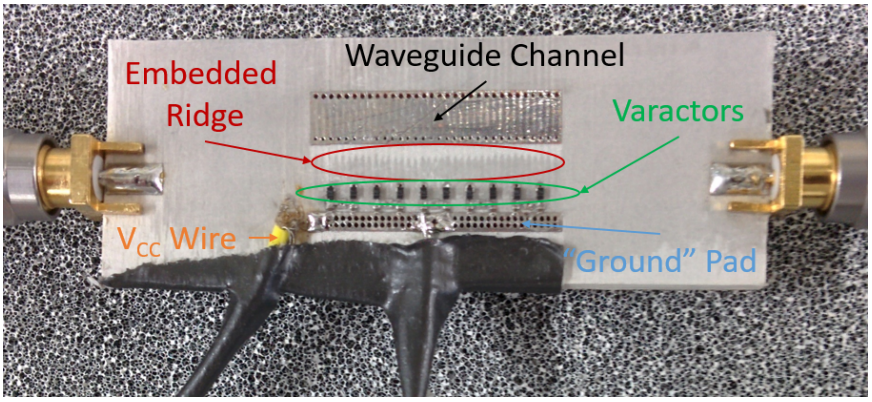

Figure 3.20: The measurement setup of the tunable phase shifter. The capacitive loading on the RHMSIW transmission line varies with the reverse bias voltage that is applied evenly across all of the varactors.

3.3 Results and Discussion

An exploded view of the proposed Butler matrix is depicted in Fig. 3.22 and a photo of the test setup is shown in Fig. 3.23. The two halves of the Butler matrix were connected using four SMA coaxial cables that are within 2° of electrical length tolerance.

Measurements were done on a Copper Mountain C2420 4-port VNA. Four ports of the Butler matrix were measured at a time with the other four terminated with 50 Ω loads. Fig. 3.24 shows the measured S-parameters for port 1 and port 2 exci-

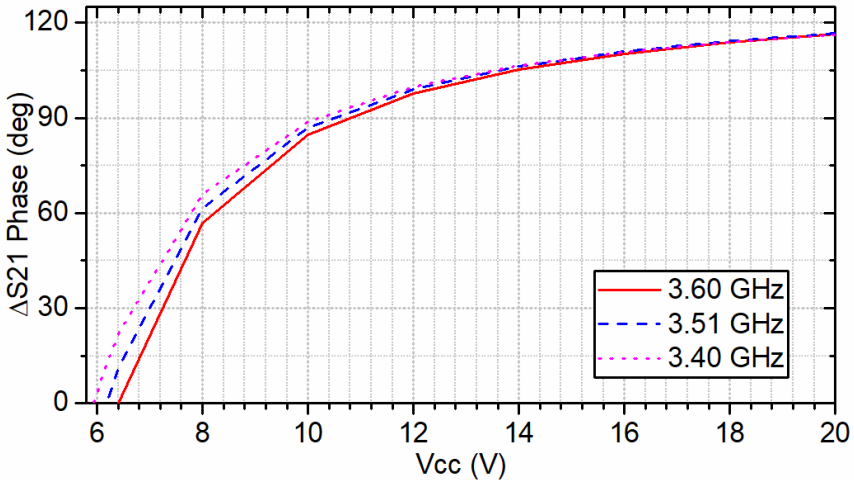

Figure 3.21: A plot showing changes in $\angle S_{21}$ as the DC reverse bias voltage varies.

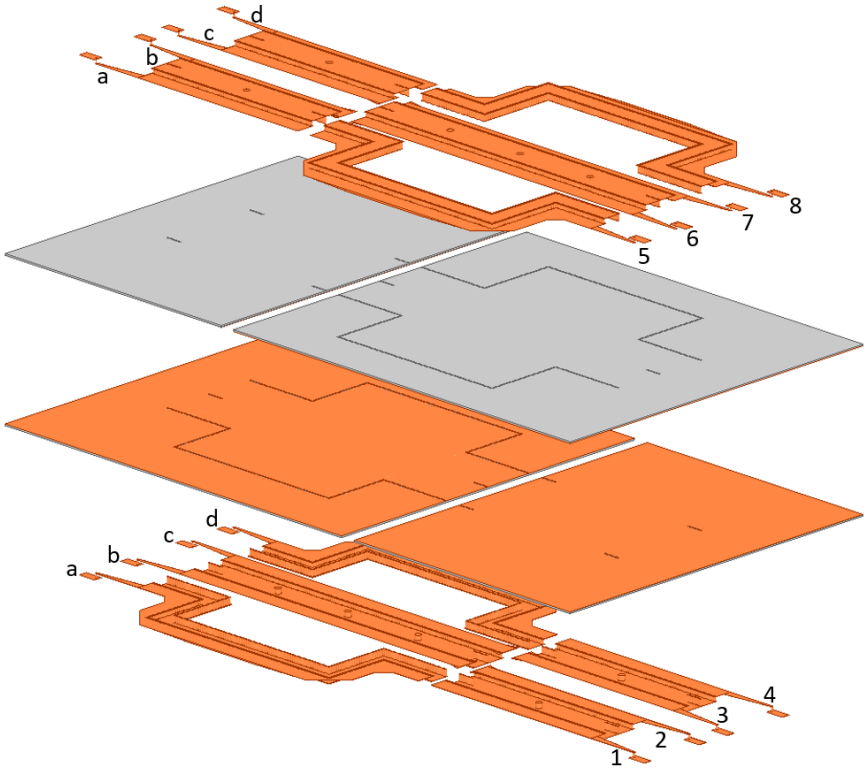

Figure 3.22: Exploded view of the proposed Butler matrix. Input ports are numbered from 1 to 4 and output ports from 5 to 8. The two halves of the device are connected with coaxial cables between each pair of ports labelled from a to d. Note that the substrate between the top conductor of the waveguides and the ridge conductor has been omitted in this diagram.

tation, and Fig. 3.25 shows the resultant progressive phase shift between the output ports. The device's power distribution between 3.422 GHz and 3.598 GHz (5% band-

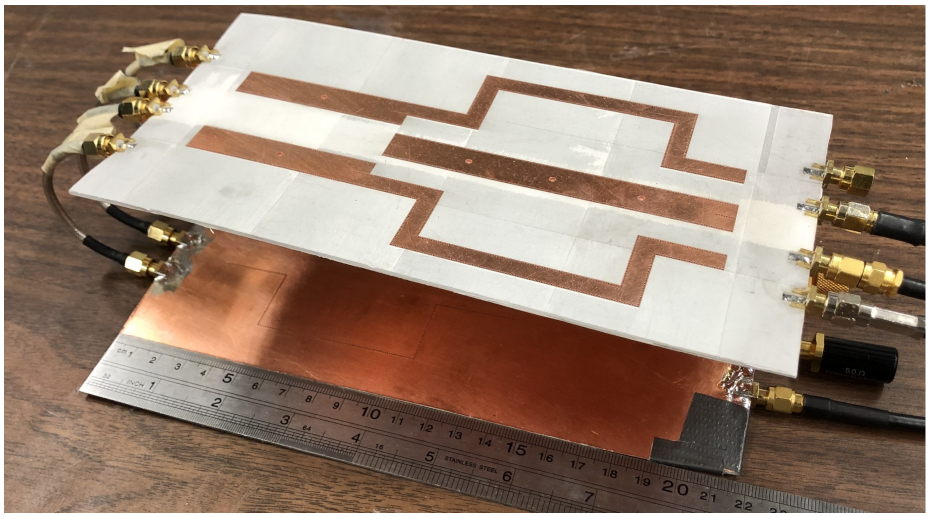

Figure 3.23: The test setup of the proposed Butler matrix. The two halves of the matrix are connected via four phase matched SMA cables.

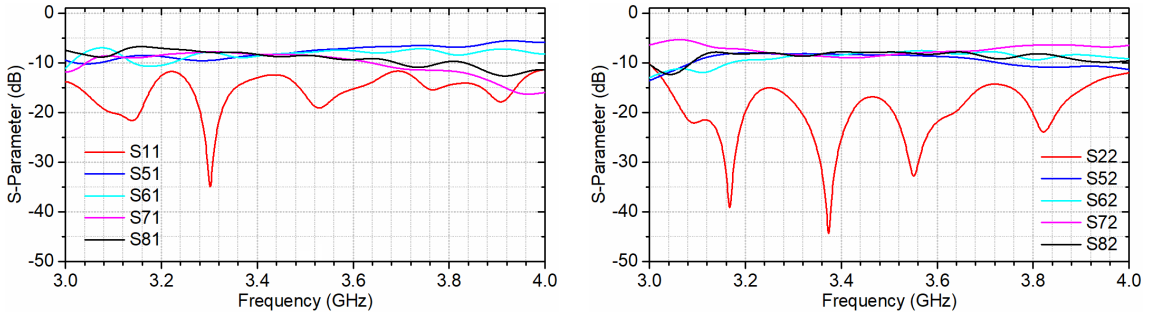

(a) (b)

Figure 3.24: The measured S-parameters of the RHMSIW 4×4 Butler matrix when (a) port 1 is fed; and (b) port 2 is fed.

width) when port 1 is fed ranges from -7.0 to -9.4 dB over the aforementioned band with an average insertion loss of 2.2 dB. When port 2 is fed, the power distribution ranges from -7.5 to -9.0 dB, also yielding an average insertion loss of 2.2 dB. Additionally, the proposed design achieves a -53.5°±21.9° output progressive phase shift when fed at port 1 and +124°±17.2° at port 2. The input isolations S_{21} and S_{32} are greater than 20.4 dB and 26.5 dB respectively in the operational 5% band.

A second set of measurements were collected in which the phase shifter presented in section 3.2.7 was attached to each of the output ports. In addition to enabling continuous beam steering, the variable phase shifters can be used to correct the

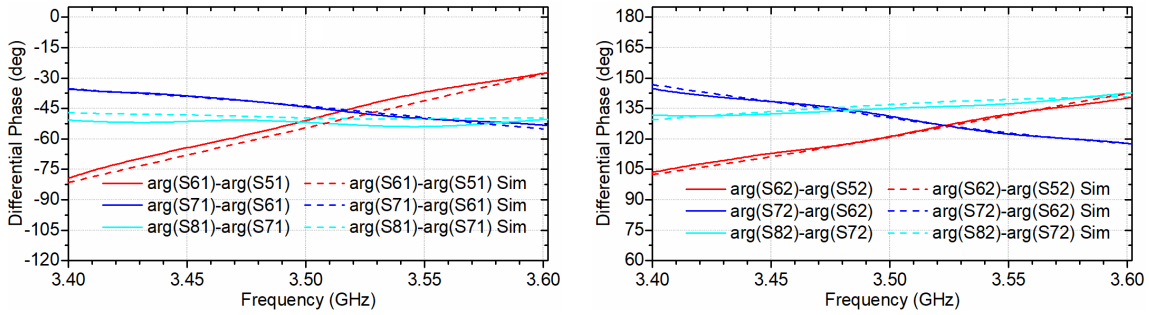

(a) (b)

Figure 3.25: The measured progressive phase shift between adjacent output ports in the 4×4 Butler matrix when (a) Port 1 is excited; and (b) port 2 is fed.

progressive phase errors described above. Fig. 3.26 shows the phase tuning of each output port when port 1 is fed and Fig. 3.27 with port 2 excitation. From the plots, it can be seen that for the same change in bias voltage, more phase tuning is generally possible at the upper band frequencies in periodically varactor loaded phase shifters as seen in [49].

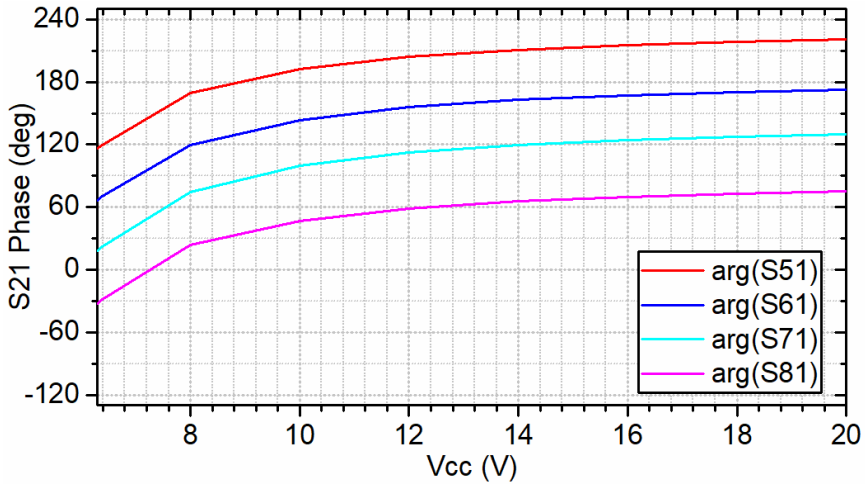

Figure 3.26: Plots showing how the phase shift at the output ports vary when port 1 is fed and the tunable phase shifter is connected to the output ports.

The total effective area the proposed Butler matrix design occupies excluding the coaxial interconnects and microstrip transitions is $11.43\lambda^2$. Table 3.1 shows a comparison of the total area occupied by Butler matrix designs using different SIW technologies in the literature. Note that all of the computed areas have been normalized to the

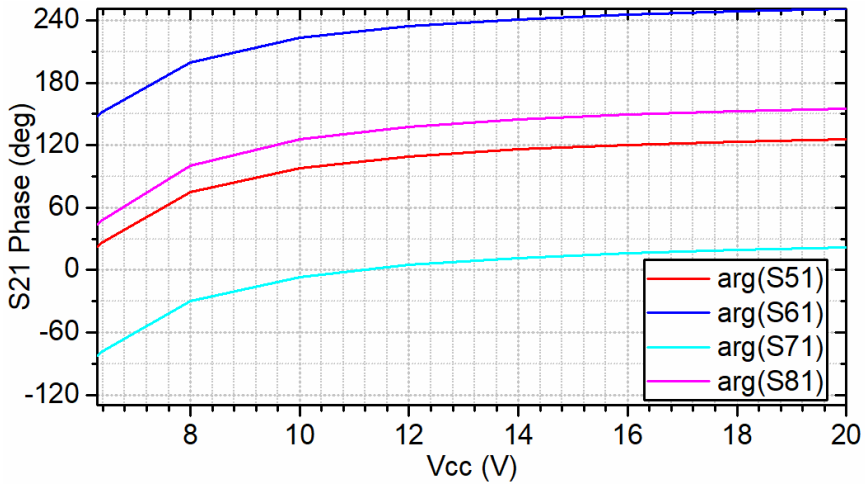

Figure 3.27: Plots demonstrating varying phase shift at the output ports when port 2 is fed and the tunable phase shifter is connected to the output ports.

Table 3.1: Size and performance comparison of the proposed structure with other SIW Butler matrix designs

Ref.	Frequency Range (GHz)	Avg. IL (dB)	Magnitude Imbalance (dB)	Phase Error	Isol. (dB)	Normalized Area (λ^2)	Technology
[65]	58 - 62	2.5	2.5	$\pm 16^\circ$	13.5	42.51	SIW
[66]	72 - 81	1.6	1.5	$\pm 3.5^\circ$	13	59.13	SIW
[71]	9.5 - 10.5	2.07	8.5	$\pm 38^\circ$	12	38.18	HMSIW
[72]	11 - 14	1.0	1.0	$\pm 5^\circ$	15	15.41	Folded-SIW
This Work	3.4 - 3.6	2.2	2.4	$\pm 21.9^\circ$	20.4	11.43	RHMSIW

substrate wavelength squared of the respective devices at their center frequencies. It can be seen that the proposed design offers over 70% miniaturization compared to a HMSIW design with similar layout topology. Further miniaturization of the proposed structure's area can be achieved by decreasing L_3 and increasing L_2 in the delay lines.

The measured results of the various components presented here are in good agreement with simulated results. Discrepancies between the presented results and the original design simulations have been demonstrated to be due to substrate thickness tolerances and thickness variations in the bonding material from the press bonding process. With some minor reworking in the design stage by taking thickness tol-

erances into account and fabricating the device using the same process, it should be possible to get better agreement between simulated and measured results and to improve on the coupling balance and phase error of the proposed Butler matrix.

In order to achieve fully continuous beam steering with the Butler matrix, the radiation pattern must be capable of being steered to the midpoint between progressive phase shifts as a result of the separate excitation of the two input ports [70]. In the case of a 4×4 Butler matrix the difference in progressive phase shift between port 1 and 2 excitation is 90°, the midpoint is therefore 45°. Therefore, to achieve continuous beam steering, a phase shifter with a tuning range of 135° is required.

3.4 Summary

A novel miniaturized Butler matrix fabricated on RHMSIW technology at a sub-6 GHz 5G band was presented. Tunable phase shifters also fabricated using RHMSIW technology can be integrated with the proposed Butler matrix and has been shown to achieve semi-continuous beam steering. The detailed design procedure for all the subcomponents of the proposed Butler matrix was discussed and the measurement results presented agree with simulation. Additionally, two novel RHMSIW interconnects were presented that also have potential for applications other than Butler matrices.

The proposed Butler matrix yields an average insertion loss of 2.2 dB and has a maximum phase error of ±22° over a 5% bandwidth centered at 3.51 GHz. Furthermore, the proposed RHMSIW device achieves over 70% miniaturization over a similar HMSIW design. With some minor reworking based on the analysis discussed in this chapter, the performance can be improved further and can even be scaled up for operation at the 5G mm-wave bands. RHMSIW technology has been shown to be a promising solution for implementing miniaturized beamforming devices at sub-6 GHz 5G bands and shows potential for expansion into the mm-wave domain.

Chapter 4

28 GHz 4×4 Shielded-RHMSIW Butler Matrix

In Chapter 3, a 3.5 GHz low-frequency prototype of a 4×4 RHMSIW miniaturized Butler matrix was presented. In this chapter, we will show how the design can be scaled up for operation at 28 GHz through the introduction of electromagnetic shielding to mitigate the increased cross-coupling between components at this band.

While it has been shown in [16] that RHMSIW has lower open-to-open side cross-coupling in comparison to HMSIW, the close proximity of components in the proposed system demands some form of electromagnetic shielding on the open edges of waveguides. Thus far, shielded-HMSIW and QMSIW – with defected ground planes and rows of metallized vias for shielding – have been used for the design of miniaturized low-radiation loss microwave components [105], we will borrow some to those concepts to shield RHMSIW lines in close proximity to each other.

It is also known that the radiation loss of many planar transmission lines have a tendency to increase with frequency [18, 106]. To demonstrate the ability of RHMSIW to operate in the K_a-band as an interconnect, this chapter also presents the first ever study of leaky-wave radiation conditions for RHMSIW lines, done between 20 and 30 GHz. It will be shown that the gain falls off very rapidly outside the leaky-wave region of the line. Devices can be developed on the RHMSIW platform as long as the interconnect operates above this region.

4.1 Leaky-Wave Conditions of RHMSIW

RHMSIW propagating their fundamental mode in the linear region have so far been shown to suffer less radiation losses than their equivalent HMSIW counterparts [16]. However, there has been limited investigation on the dispersive region performance of RHMSIW. In this section, we will analytically obtain the propagation constants of RHMSIW to determine the band that the structure will most efficiently radiate as a LWA.

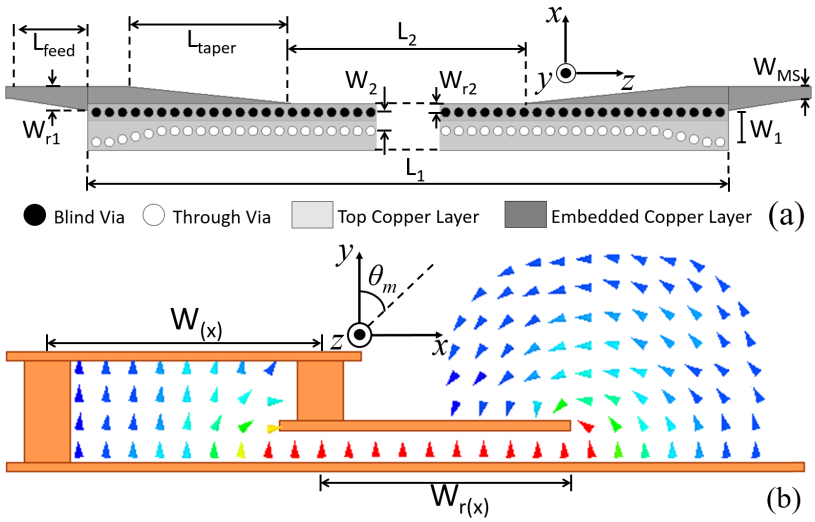

Figure 4.1: Illustrations of the RHMSIW lines / leaky-wave antenna studied in this section. (a) The truncated bird's-eye view layout. The RHMSIW lines studied in simulation are directly fed with 50 Ω microstrip lines. Both the ridge and the electric via wall of the RHMSIW are tapered into narrower sections. The pitch of the via holes are 0.35 mm, the electric wall taper consists of three holes lined up diagonally. (b) The transverse view of RHMSIW. Note that the electric field is strongest and concentrated under the capacitive ridge. The radiation angle θ_m, is defined from the broadside axis (y).

4.1.1 RHMSIW Propagation Mode

The RHMSIW can be modelled as a HMSIW with a step discontinuity in its transverse plane. The transverse plane depicted in Fig. 3.2 can be modelled as a transmission line terminated with a short-circuited and open-circuited stub. The cutoff wavenumber can then be numerically computed from the transverse resonance

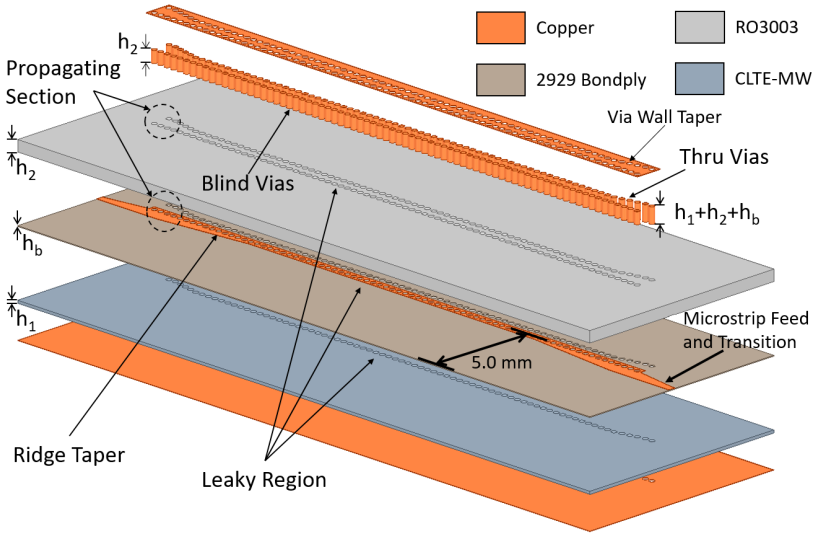

Figure 4.2: The exploded view of the proposed RHMSIW leaky-wave antenna showing the embedded ridge and microstrip feed line.

technique described in equations (2.7)-(2.10) [16].

The RHMSIW structures presented in this thesis as they are without any additional reactive loading always yields real solutions to k_c computed from (2.10). It can therefore be seen from $\beta = \sqrt{k^2 - k_c^2}$ that β is always less than k across all frequencies, i.e., RHMSIW channels are fundamentally fast-wave structures in the medium they are constructed and RHMSIW is therefore able to support leaky-wave radiation [107]. However, some conditions must be met for the structure to radiate into free-space, as will be discussed below.

4.1.2 Leaky Mode Analysis

Fig. 4.1 depicts the layout of the interconnects and coordinate system that will be used to study RHMSIW leaky modes. A 3D exploded view is shown in Fig. 4.2. The lighter shade of grey in Fig. 4.2 represents a Rogers RO3003 substrate ($\epsilon_r = 3.0$, $tan\delta = 0.0011$) which is bonded to CLTE-MW ($\epsilon_r = 3.0$, $tan\delta = 0.0015$) represented by dark grey using 2929 Bondply (beige). 50 Ω microstrip lines are tapered into the RHMSIW capacitive ridge where the electric field of its fundamental propagating mode is the strongest as shown in Fig 4.1(b). Both the ridge and the through-via

electric wall are then tapered into narrower sections which can be shown from (2.10) and (2.11) to decrease β and thus increase the phase velocity at a given frequency. The dimensions of the proposed radiating element in this study are presented inn Table 1. Since the height of the capacitive ridge is only 0.127 mm, the glass-woven Rogers CLTE-MW substrate was chosen as the bottom substrate material due to its mechanical stability during the bonding process [108].

SIW based leaky-wave antennas have apertures running through the full length of their structures that allow an alternate propagation direction [109, 110]. Mathematically, this is represented by introducing a second complex exponential term with a second propagation constant (k_x) [107]:

$$E_y(x,z) = Ae^{-jk_z z}e^{-jk_x x} \tag{4.1}$$

An imaginary attenuation term ($j\alpha$) is added to the otherwise lossless propagation constant β (neglecting conductor and dielectric losses) obtained from (2) to account for power "leaking" away from the power travelling in the z-direction [111]:

$$k_z = \beta - j\alpha \tag{4.2}$$

$$k_x = \beta_x - j\alpha_x \tag{4.3}$$

The transverse complex wavenumber k_x can then be computed from k_z using [112]:

$$k_x^2 + k_y^2 + k_z^2 = \epsilon_r k_0^2 \tag{4.4}$$

where k_0 is the free-space wavenumber. In the context of a RHMSIW propagating its fundamental quasi-$TE_{0.5,0}$ mode, in mono-mode operation with a y-directed electric field at its capacitive ridge, k_y can be assumed to be 0.

The complex $k_z = \beta - j\alpha$ can be computed using a combination of the transverse resonance method and perturbation techniques [113]. However, it can be seen in several studies [110, 114, 115] that these analytic techniques lose accuracy as the

waveguide approaches cutoff. It is therefore more practical to obtain these constants through full-wave EM simulations. Two lines of length L_1 || L_2 = 26 mm || 14.8 mm, and 21.1 mm || 9.9 mm as depicted in Fig. 4.1(a) and Fig. 4.2, are simulated using Ansys HFSS. From the multiline method detailed in Appendix C [116–118], the complex propagation constant for the narrow leaky channel is extracted by de-embedding the effects of the microstrip transitions and the ridge tapers. These de-embedded results are plotted in Fig. 4.3.

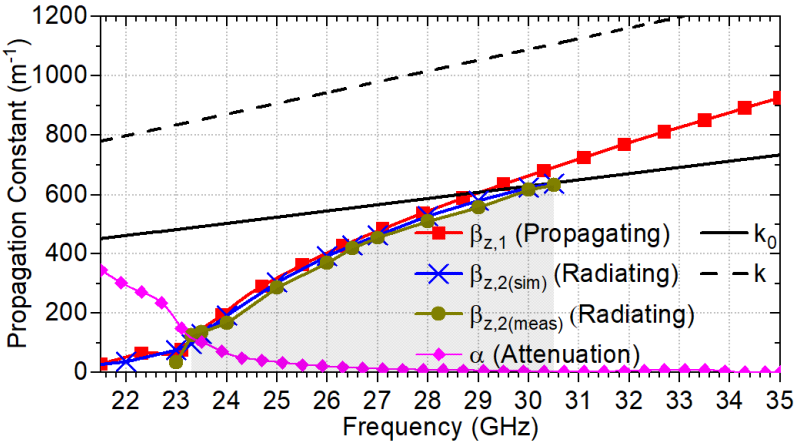

Figure 4.3: A plot of the extracted phase / attenuation constants, and TEM wavenumbers. The shaded area defines the bounds of the RHMSIW leaky-mode. The estimated cutoff of the waveguide (where α intersects $\beta_{z,1}$) is 23.3 GHz. The phase constant of the radiating mode converges with k_0 at around 30 GHz, beyond which, the waveguide ceases to radiate effectively.

Finally, the radiation angle θ_m from the broadside axis defined in Fig. 4.1(b) of leaky-wave antennas can be computed from:

$$\sin\theta_m = \frac{\beta_{z,2}}{k_0} \tag{4.5}$$

where $\beta_{z,2}$ is the leaky-mode propagation constant [112, 115]. Conversely, (4.5) can be used to extract $\beta_{z,2}$ from a known radiation angle obtained from simulation. The extracted $\beta_{z,2}$ curve from simulating a radiating aperture of length L_2 = 23.9 mm is shown Fig. 4.3 where is can be seen to converge with k_0 at around 30 GHz. From the simulated maximum gain vs frequency plot shown in Fig. 4.4, it can be seen

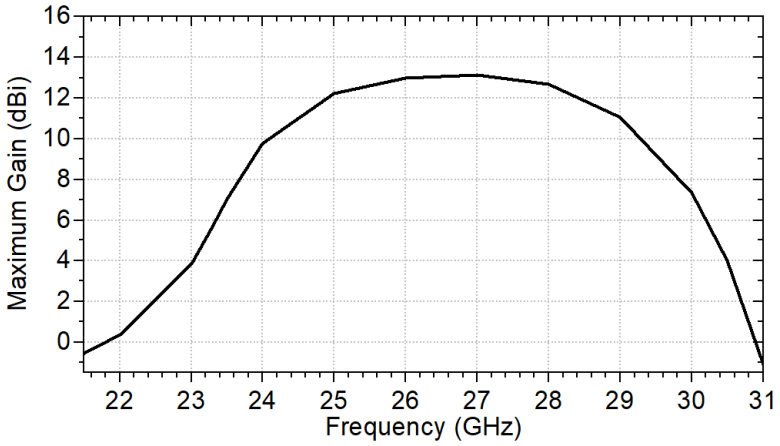

Figure 4.4: The simulated maximum gain of the antenna vs frequency. It can be observed that the gain rapidly falls off beyond 30 GHz at which point the wavevector begins to be directed in the longitudinal direction.

that beyond this point, the gain rapidly decreases with frequency. The discrepancy between $\beta_{z,1}$ and $\beta_{z,2}$ is due to the fact that for the radiating mode, k_y has a non-negligible value since there is propagation outside the plane of the substrate; this results in $\beta_{z,2} < \beta_{z,1}$ as can be confirmed in (4.4). It can also be observed that there is less than a 4% discrepancy between k_0's intersection points with $\beta_{z,1}$ and $\beta_{z,1}$. The studies of sections 4.1.1 and 4.1.2 confirms the findings in [16] that RHMSIW can act as an effective interconnect with very low insertion loss when it is operated in the slow-wave domain ($\beta_z > k_0$). From the findings in these sections, it can also be concluded that leaky-wave antennas can be designed using RHMSIW and that it best radiates between the cutoff frequency and the intersection point of the phase constant (β_z) with k_0.

4.2 Butler Matrix Design

The transverse cross section of a shielded-RHMSIW interconnect is shown in Fig. 4.7 and the three main types of subcomponents of a 4×4 Butler matrix are shown in Fig. 4.6: quadrature hybrids (QH) to split power with a 90° phase difference, crossover lines to ensure the signal with the correct phase outputs through the correct port,

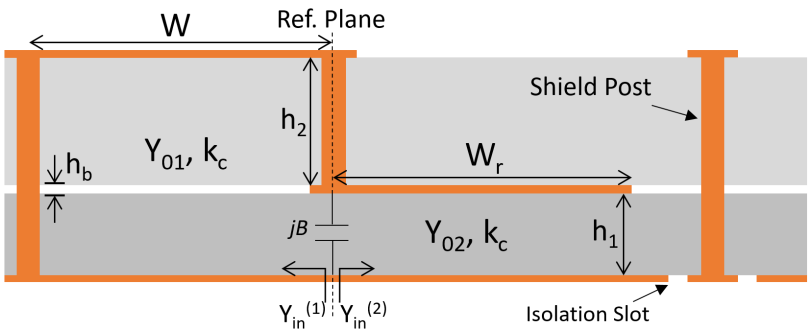

Figure 4.5: The transverse plane cross-section of a Shielded-RHMISIW line. Light grey represents RO3003^{TM}, dark grey CLTE-MW^{TM}, and white 2929 Bondply^{TM}. The thicknesses of the substrates are $h_1 = 0.127$ mm, $h_2 = 0.508$ mm, and $h_b = 0.0381$ mm. W and W_r varies to suit subcomponents' designs.

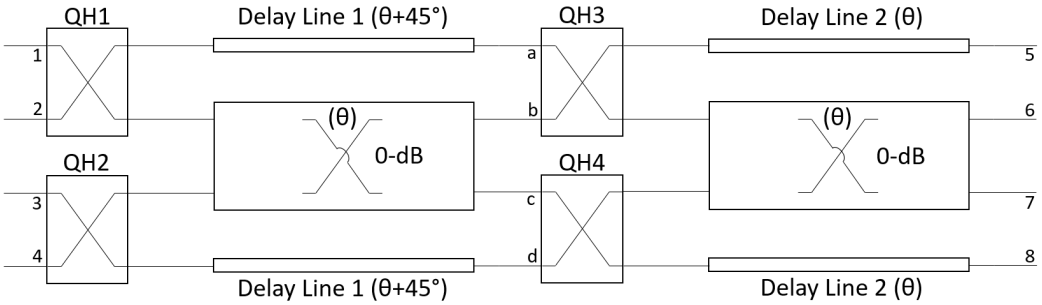

Figure 4.6: The general block diagram of a Butler matrix using 0-dB couplers in lieu of multilayer crossover lines. Input ports in this chapter are labelled 1 to 4 and output ports from 5 to 8.

and delay lines. Delay line 2 must incur the same phase as the crossover coupler, and a further 45° must be incurred in delay line 1. When port 1 of Fig. 4.6 is excited, each successive output port (5 to 8) lags the preceding port by 45°. Similarly, each output port leads each preceding one by 135° when port 2 is excited.

4.2.1 Shielded Ridged Half-mode SIW Quadrature Hybrid

Although it has been shown that RHMSIW have relatively low radiation loss when operated well above cutoff [16], the compactness of the proposed system's layout inevitably leads to cross-coupling between components which can lead to magnitude imbalance and progressive phase error at the output ports. Fig. 4.7 illustrates the layout of the quadrature hybrid (QH) couplers [16] in the proposed device. The mode

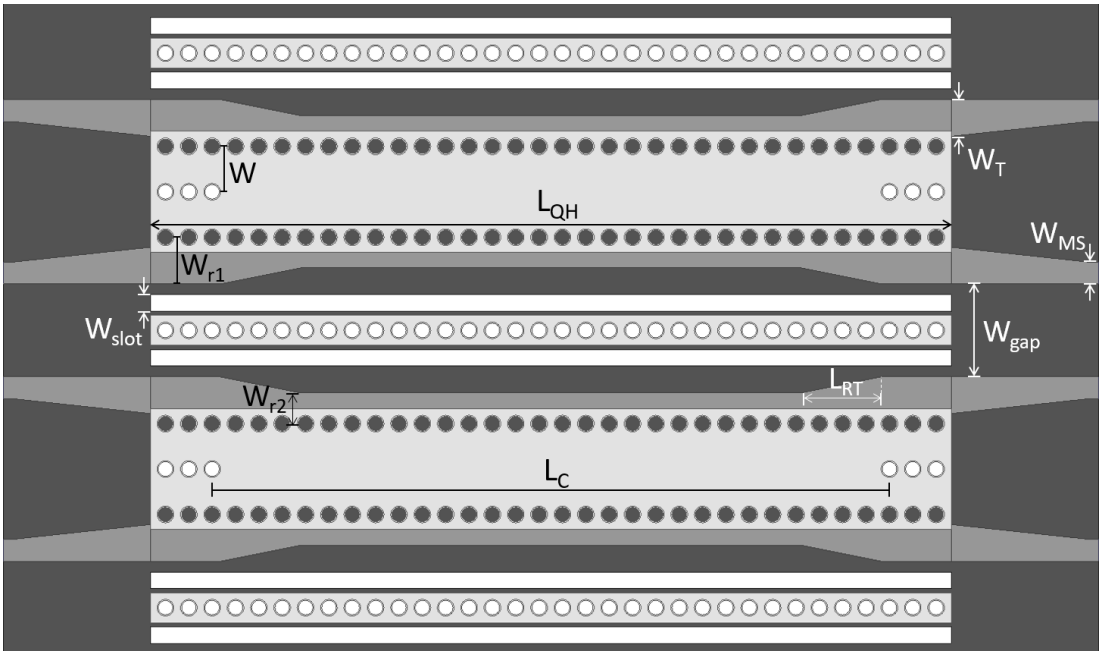

Figure 4.7: The layout of shielded-RHMSIW quadrature hybrid couplers. The light, medium grey, and darkest shades of grey respectively represents the top, ridge, and ground metallization layers. Dark and white circles represent blind and through vias respectively. The transverse dimensions W, W_{r1}, and W_{r2} are 0.68, 0.7, and 0.46 mm respectively. $W_T = 0.55$ mm, $W_{MS} = 0.23$ mm, $W_{gap} = 1.39$ mm, $W_{slot} = 0.3$ mm, $L_{QH} = 12$ mm, $L_C = 10.15$ mm and $L_{RT} = 1.2$ mm.

excited in the coupling region of length L_C can be seen as a superposition of even and odd modes which propagate with different phase velocities. It has been shown in equations (2.14) and (2.15) that the output ports are theoretically always 90° out of phase across all frequencies above the dispersive region and the coupling magnitude can be manipulated by tuning L_C such that $\Delta\theta = L_C(\beta_e - \beta_o) = \pi/2$ [32]. Although it is known to be significantly more narrowband than SIW designs, the RHMSIW QH [16] is known to be the narrowest short-slot coupler at the time of publication.

The two quadrature hybrid couplers feed the same 0-dB coupler in the next stage. Due to the narrow total width of the 0-dB coupler – as a direct consequence of the miniaturization achieved by RHMSIW – the QHs are spaced less than 1.4 mm apart. To minimize cross-coupling, a metallized via wall was inserted in between the two couplers. Slots were etched in the ground plane to act as magnetic walls [105] for the

open sides of the RHMSIW. To maintain the symmetry of the QHs, the slot and via wall pattern is repeated on the opposite sides of the couplers. Finally, the ridge in the coupling region is tapered into a narrower section (W_{r2}) to reduce reflections and improve isolation [65]. In simulating two adjacent RHMSIW transmission with the same ridge taper and spacing, it was shown that there is a 5.0 dB improvement in isolation, and 2.2° of phase difference when shielding is introduced.

4.2.2 Crossover Coupler

The 0-dB coupler used for the crossover stages in the proposed Butler matrix depicted in Fig. 4.8 follows the same operating principles as the short-slot QH coupler; the length of the coupling region (L_C) is tuned such that all power is coupled between diagonal ports while adjacent ports remain isolated, i.e., such that $\Delta\theta = L_C(\beta_e - \beta_o) = \pi$. In the final design of the proposed device, the RHMSIW lines of the QHs are directly connected to those of the 0-dB couplers as shown in Fig. 4.9. It was shown in [16] that the electric field is strongest in the capacitive ridge of the RHMSIW. Due to the asymmetry of the RHMSIW, this fact is key to the device miniaturization using RHMSIW. The ridge is tapered at an angle in this design to further separate the two QH couplers.

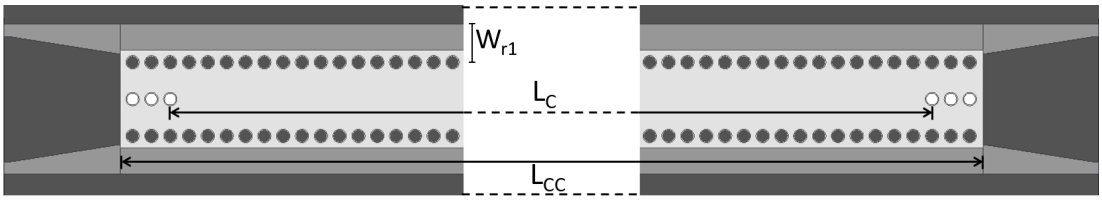

Figure 4.8: The layout of the crossover coupler with dimensions. $L_{CC} = 25.3$ mm, $L_C = 23.45$ mm, and $W_{r1} = 0.7$ mm.

4.2.3 Delay Line

From equations (2.10) and (2.11), it can be shown that the phase of a RHMSIW transmission line can be manipulated by varying the amount of capacitive loading on

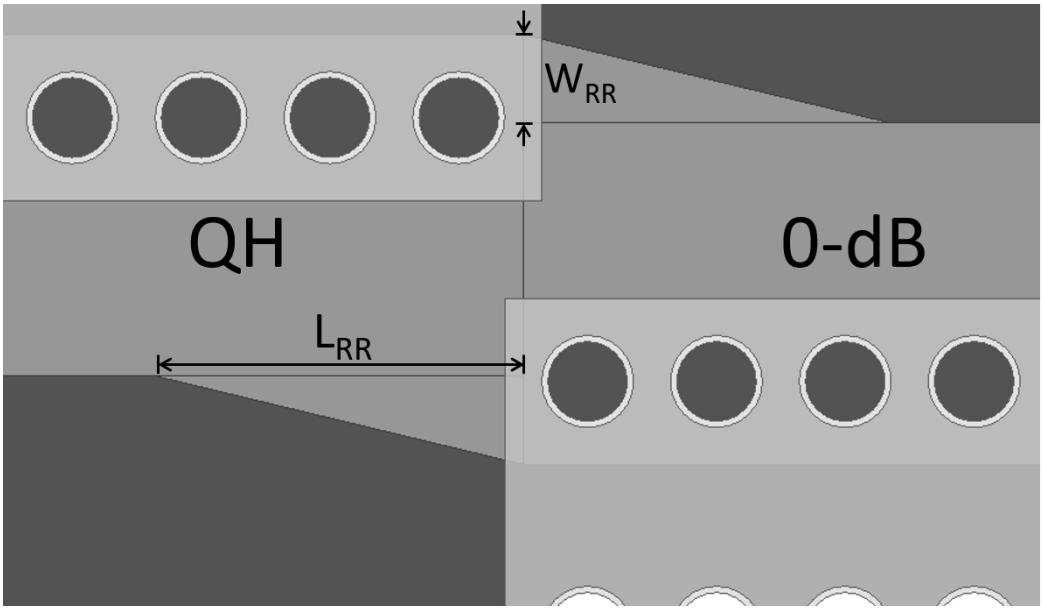

Figure 4.9: Asymmetric ridge-to-ridge transition between the hybrid and crossover couplers. W_{RR} and L_{RR} are 0.215 and 0.95 mm respectively. The top layer has been rendered semi-transparent to show the full pattern of the taper.

the ridge. When the transverse dimensions of the waveguide, W and W_r are altered, k_c, and by extension, β will change; generally, the phase delay decreases with smaller W and W_r as a result of an increased k_c. The phase delay of an RHMSIW can therefore be engineered by tuning the channel widths in simulation. The line must be designed such that it does not operate in the dispersive region where it can radiate as was discussed in section 4.1. The dimensions of the delay lines in the proposed design are given in Fig. 4.10. The first pair of delay lines have larger physical dimensions than the second pair since it must incur an extra 45° of phase.

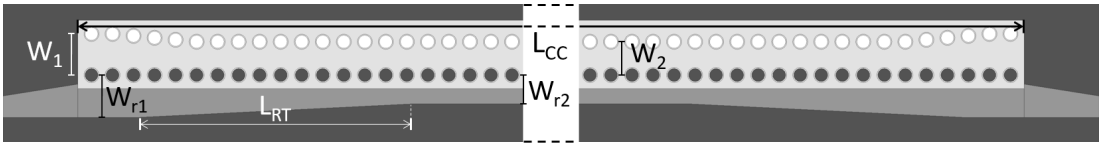

Figure 4.10: The layout and dimensions of the proposed device's delay lines. The delay lines are the same length as the 0-dB couplers (L_{CC} = 25.3 mm). W_1 = 0.68 mm, W_{r1} = 0.7 mm, and L_{RT} = 4.6 mm. For delay line 1, W_2 = 0.56 mm and W_{r2} = 0.555 mm, and are 0.55 and 0.475 mm respectively for delay line 2.

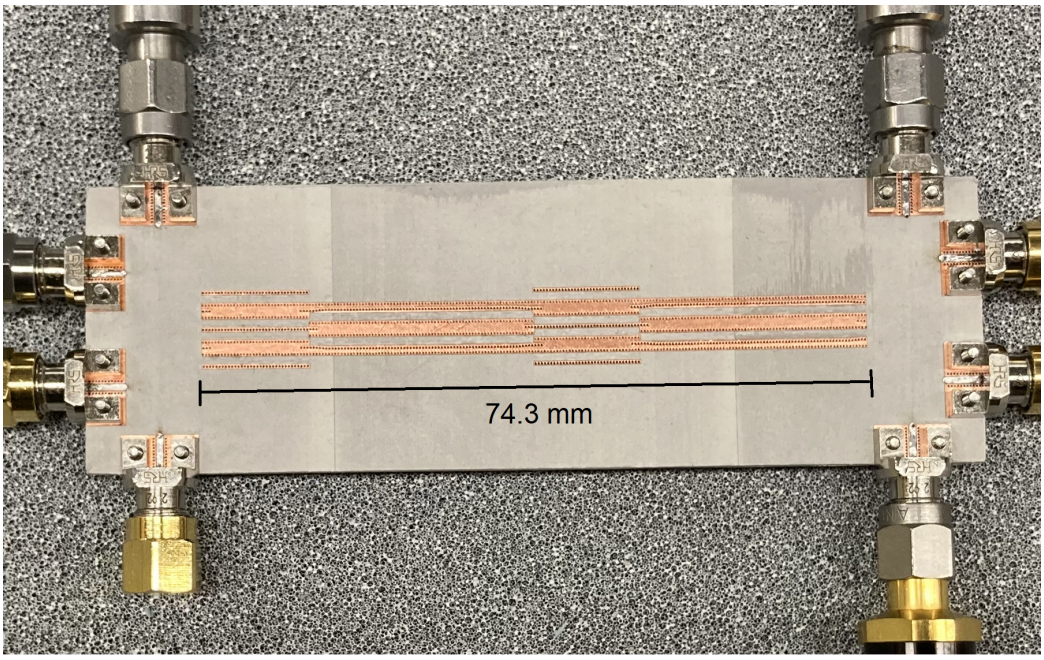

Figure 4.11: A photo of the measurement setup for characterizing the proposed Butler matrix. The total length of the device is 74.3 mm excluding microstrip tapers.

4.3 Results and Discussion

A photo of the experimental setup is shown in Fig. 4.11. Two more pairs of slots are etched into the ground plane adjacent to the four delay lines to improve the isolation between the 0-dB couplers and the delay lines in a similar operating principle to what was described in section 4.2.1. All measurements were done on the HP 8510C VNA. The measured coupling magnitudes are plotted in Fig. 8 and the progressive phase shift in Fig. 9. Note that only the results for the excitation of two input ports are shown due to symmetry.

From Fig. 4.12, it can be seen that the device has greater than 10 dB return loss from 27.33 GHz to 28.8 GHz. The average insertion loss is 6.2 / 6.5 dB when ports 1 / 2 are excited. According to the simulation of the microstrip to CPW feedlines, those connected to ports 1, 4, 5, and 8 have 0.66 dB insertion loss and 0.75 dB for those feeding ports 2, 3, 6, and 7. Corrected for these feeding line losses, the average insertion loss when ports 1 / 2 are respectively excited are 4.9 / 5.1 dB.

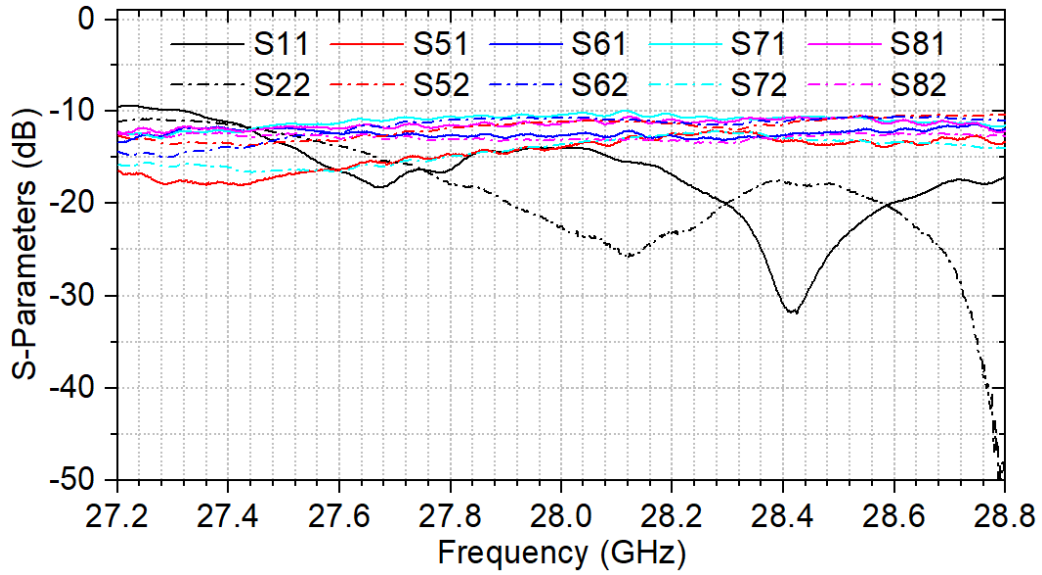

Figure 4.12: Measured coupling magnitude vs frequency plots of the proposed Butler matrix when port 1 (solid lines) and port 2 (dashed lines) are excited.

The Butler matrix achieves -55.3° ± 14.1° and +126.5° ± 30.7° of progressive phase shift between 28.0 and 28.8 GHz when ports 1 and 2 are excited respectively. The average coupling magnitude imbalance between 28.0 and 28.8 GHz is ±1.3 and ±1.2 dB when port 1 and 2 are respectively excited. In the fabrication of the presented device, there were misalignments of the via hole walls on the order of tens of micrometers which is primarily responsible for the relatively large imbalances in progressive phase shift and magnitude in the measured results. The progressive phase shift error of 30.7° could potentially result in more than 10° of beam pointing error for a $\lambda/2$ pitch array driven by this device.

In Table I, the total area (normalized to substrate wavelength) occupied by the proposed design is compared with those of the referenced designs. Although the proposed design has good performance at its center frequency (28.3 GHz), it is apparent from Fig. 4.12 and Fig. 4.13 that the low error does not hold over the entire operational band. This is owing to the fact that the delay lines are operating closer to cutoff (more dispersive) compared to other components in the system. This observation can be supported by the fact that the phase responses in Fig. 4.13 involving port 5, in which

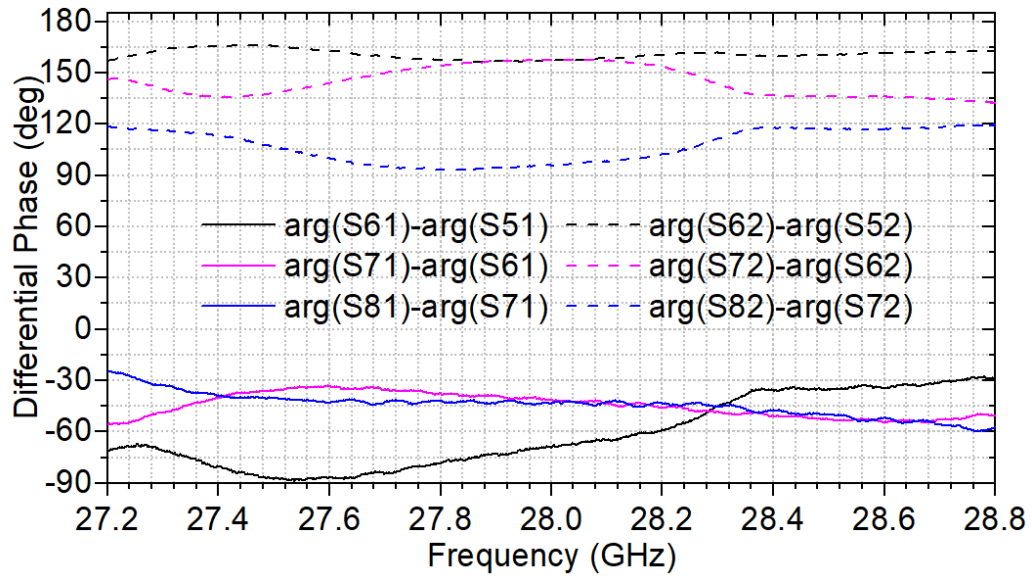

(a)

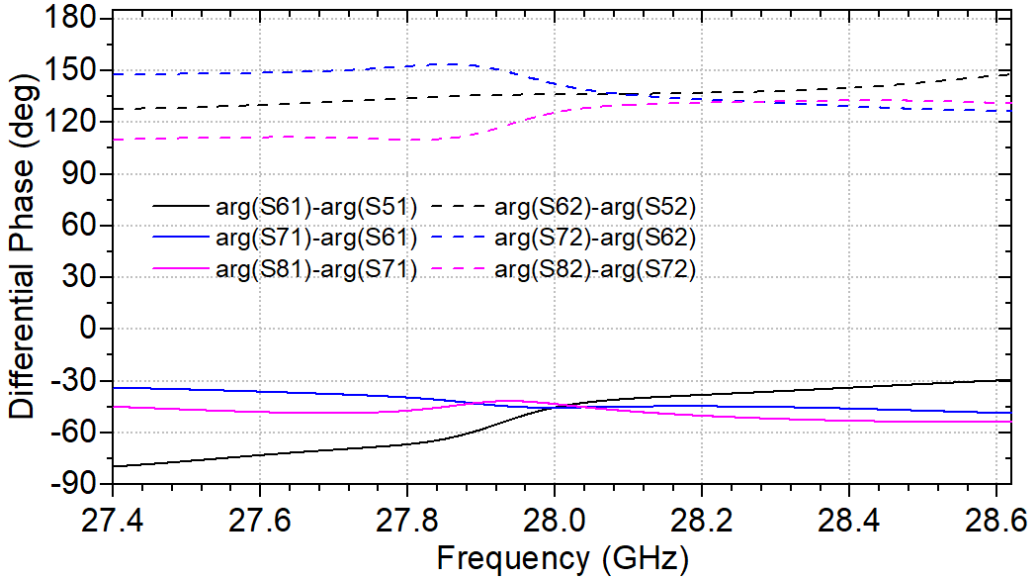

(b)

Figure 4.13: Progressive phase shift vs frequency plots for port 1 (solid lines) and port 2 (dashed lines) excitation. (a) Measured. (b) Simulated.

signals reaching it must pass through two delay lines, tend to also have the greatest variation over frequency. It is however important to note that although RHMSIW structures have a tendency to be narrowband [16], the proposed structure using SD-RHMSIW technology has the smallest footprint at mm-wave frequencies, achieving more than 65% miniaturization over a reference conventional SIW design [65], and

Table 4.1: Size and performance comparison of the proposed structure with other SIW Butler matrix designs

Ref.	Frequency Range (GHz)	Avg. IL (dB)	Magnitude Imbalance (dB)	Phase Error	Normalized Area (λ^2)	Technology
[65]	58 - 62	2.5	2.5	$\pm 16^\circ$	42.51	SIW
[71]	9.5 - 10.5	2.07	8.5	$\pm 38^\circ$	38.18	HMSIW
[72]	11 - 14	1.0	1.0	$\pm 5^\circ$	15.41	Folded-SIW
[119]	175 - 185	1.0	1.8	$\pm 45^\circ$	15.41	Micromachined PTFE SIW
[120]	93.7 - 94.3	0.8	3.0	$\pm 20^\circ$	765.16	CNC Milled GGW
Ch. 3	3.4 - 3.6	2.2	2.4	$\pm 21.9^\circ$	11.43	RHMSIW
This Work	28 - 28.8	6.5	2.6	$\pm 30.7^\circ$	14.59	SD-RHMSIW

that the simulated maximum phase imbalance extracted from Fig. 4.13(b) is $\pm 13.5^\circ$, suggesting that the relatively large realized phase imbalance is due to fabrication tolerances and errors.

4.4 Summary

In this thesis, a miniaturized 4×4 Butler matrix based on shielded-RHMSIW technology was proposed for operation in a 5G 28 GHz band. Unhindered, cross-coupling between components can lead to significant phase and magnitude disruptions in the device's output; the narrow channels, open edges, and close proximity of waveguides in the proposed system therefore demands proper electromagnetic shielding to prevent the undesired cross-coupling. The proposed device achieves a maximum of $\pm 30.7^\circ$ progressive phase error and an average of ± 1.3 dB coupling magnitude imbalance between its output ports. The narrow waveguide channels and tight tolerances of RHMSIW at high frequencies may introduce various fabrication challenges that need to be addressed for practical implementation. Although the published device is only able to maintain low errors over a very narrow band in comparison to other

SIW implementations of the system, it also has the smallest electrical footprint at mm-wave bands to date.

Chapter 5

W-Band Photoconductive Evanescent-mode Waveguide Switches

The utilization of mmWave signals for 5G communication systems present unique challenges such as higher path losses, higher atmospheric attenuation, and greater radiation losses from conventional planar microwave transmission lines such as microstrip [18] and coplanar waveguides [106].

Moving forward, 6G systems are expected to utilize spectrum in the W-band where the aforementioned challenges are further amplified [4]; this requires the development of reliable micromachined waveguide interconnects which have been shown to have relatively low insertion losses up to several hundreds of GHz [121]. In mmWave switch technologies, PIN diodes, electromechanical switches, and RF MEMS have all been integrated into waveguide-based interconnects. However, electromechanical switches have slow switching speeds, RF MEMS have reliability issues and higher production costs compared to semiconductors, and mmWave PIN diodes generally have low power handling and high insertion losses [94].

Photoconductive waveguide switches on the other hand, have been shown to be an excellent compromise between the high switching speeds of semiconductor switches while offering relatively high power handling [92]. Furthermore, they have been shown to offer low insertion loss and have high linearity. In [95], it has been shown the

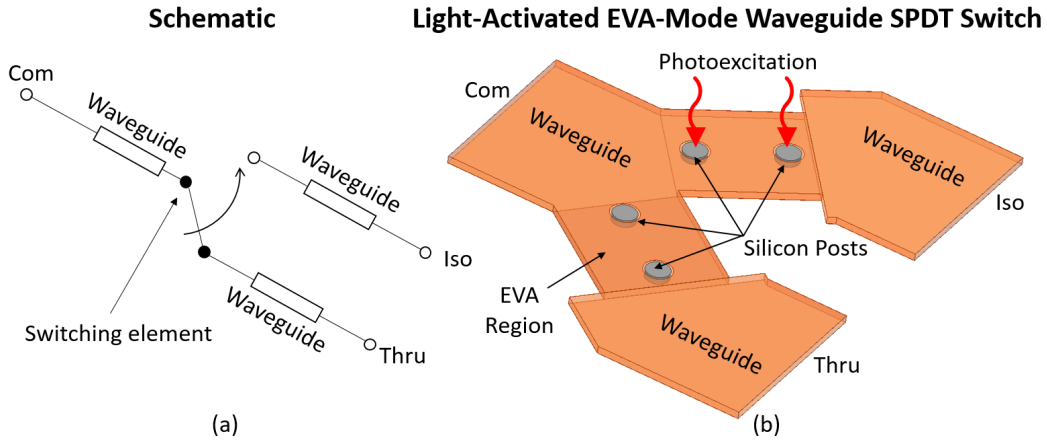

Figure 5.1: Illustrations of single pole double throw (SPDT) switches. (a) General schematic of SPDT switches which consist of a "common" port that is always connected to one of two other branches. The port currently connected to the common port is known as the "through/thru" port, and the disconnected one, the "isolated" port. (b) A general concept of a SPDT switch using the photoconductive waveguide switch technology. The channel that is not excited with light behaves like a bandpass filter whereas the photoexcited branch is shorted and is isolated from the common port.

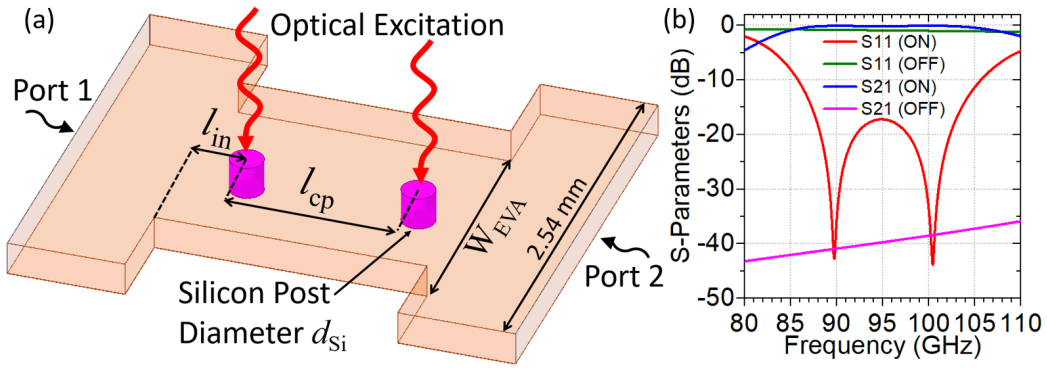

Figure 5.2: (a) The 3D model of a simple silicon photoconductive EVA waveguide switch. W_{EVA} represents the width of the EVA channel, l_{cp} the coupling distance between the silicon posts (center-to-center), and l_{in} the input coupling length. Optical fibers can be used to switch the high resistivity silicon posts inside the waveguide channel between its dielectric and conductive states. The height of the waveguide cavity is 200 µm. The nominal values of l_{in}, l_{cp}, and W_{EVA} are 0.3 mm, 1.02 mm, and 1.5 mm respectively. The nominal silicon post diameter (d_{Si}) is 0.2 mm. (b) A simulation of the 3D models using the nominal dimensions.

optical power needed to achieve high isolation using photoconductive silicon posts can be reduced by placing them in evanescent-mode (EVA) waveguide channels, albeit sacrificing some bandwidth.

Multi-throw switches play a key role in RF communication frontends such as reconfigurable antennas [78], Rotman lenses [68], and Butler matrices [79, 80] which require common source signals to be routed to different channels robustly. In this chapter, a fully waveguide connectorized single pole double throw (SPDT) photoconductive EVA-mode switch design is presented. Furthermore, this chapter provides a detailed theoretical analysis on photoconductive EVA waveguide channel and switch design, the design procedure for a standard to reduced-height waveguide transition, the first demonstration of both single pole single throw (SPST) and SPDT switch designs with three posts to further reduce the optical power requirement, and the first ever characterization of the switching speed and power handling of this waveguide switch technology within the W-Band.

First, the fundamental operating principles, theory, and design of photoconductive EVA waveguide switches are presented; namely, the photoconductive effect along with filter theory using coupled resonators. In Section 5.2, the fundamental design considerations, limitations, trade-offs, and simulated results of photoconductive EVA waveguide switches are discussed. Section 5.3 discusses the design considerations for practical implementations of the proposed switches, with the assembly of the fabricated devices presented in Section 5.4. Finally, in Section 5.5, the experimental setup and characterization results of the fabricated devices, including switching speed and power handling, are presented and discussed.

5.1 Principle of Operation

Fig. 5.1 depicts the fundamental concept of a photoconductive EVA-mode SPDT waveguide switch. 915 nm light is used to redirect the common port of the switch to one of two output ports. The fundamental operating principle behind its switching elements is a combination of the photoconductive effect with EVA waveguide theory. The conductivity of a silicon post can be controlled by the magnitude of optical excitation. When silicon posts are placed inside an EVA waveguide channel in their

dielectric state, a bandpass filter response can be established. In their conductive state, the combination of a waveguide in its cutoff state and a low-impedance shunt from the posts yields very high impedance mismatches, allowing very high switch isolations to be achieved with low intensity optical excitation [95].

5.1.1 Photoconductive Effect

Conductivity can be induced in a semiconductor through excitation with light at a photon energy greater than the bandgap of the semiconductor, generating electron hole pairs inside the material. High resistivity silicon (HR-Si) is a good candidate for the switching element due to its ability to act as a low loss dielectric at the mmWave band in the absence of photoexcitation. Furthermore, its relatively low bandgap offers an abundance of high-power optics solutions for inducing high conductivity. The DC conductivity of silicon can be computed as follows [94, 122]:

$$\sigma_{\mathrm{DC}} = q(\mu_{\mathrm{p}} + \mu_{\mathrm{n}})n' \tag{5.1}$$

where q is the elementary charge, n' is the excess carrier concentration (assumed to be uniform in the material), and μ_{n} and μ_{p} are the carrier mobilities of electrons and holes, respectively. The carrier mobilities of silicon, with n' in units of cm^{-3} and μ_{n} and μ_{p} in units of $cm^2V^{-1}s^{-1}$, can be calculated as follows [94, 123]:

$$\mu_{\mathrm{n}} = \frac{1318}{1 + \left(\frac{n'}{1\times10^{17}}\right)^{0.85}} + 92 \tag{5.2}$$

$$\mu_{\mathrm{p}} = \frac{420}{1 + \left(\frac{n'}{1.6\times10^{17}}\right)^{0.7}} + 50. \tag{5.3}$$

With this, (5.1) can be written to be entirely dependent on the excess carrier concentration n' which can be computed as a function of photoexcitation as follows [94, 122]:

$$n' = \frac{P_0/h\nu}{\alpha H^2}\tau\,(1-R)\left(1-e^{-\alpha H}\right) \tag{5.4}$$

where P_0 is the incident light intensity, R and α are respectively the reflection and absorption coefficients of the material – which can be calculated from the real and imaginary components of the refractive index – τ the carrier lifetime, and H the height of the semiconducting material under excitation. It can be seen from equations (5.1) to (5.4) that the conductivity of the silicon switching elements increases with optical power. It was previously shown in [94], that HR-Si posts extending from top to bottom of a rectangular waveguide channel at its center can be used to switch it ON/OFF to incident radio frequency (RF) signals. When excited with photons above the bandgap energy of silicon (E_g = 1.12 eV [122]), the HR-Si posts enter their conductive state and shorts the TE_{10} mode of the waveguide channel where the electric field is strongest (at the center of the channel). When no light is present, the HR-Si acts as a low loss dielectric and will allow RF propagation through the waveguide.

5.1.2 Evanescent-Mode Waveguide Coupled Resonators

A 3D model of a two-pole silicon photoconductive EVA waveguide switch is illustrated in Fig. 5.2. In the OFF-state of the switch, the silicon posts are excited with 915 nm light from the optical fibers; the posts become conductive due to the photoconductive effect. The now conductive posts at the center of the channel short out the fundamental TE_{10} mode where the electric field is the strongest. Coupled with the fact that the narrow channel is already operating below cutoff, very high OFF-state isolation can be achieved with this design.

In rectangular waveguides, it is known that below the cutoff frequency of its fundamental TE_{10} mode, the waveguide – now in evanescent mode – begins to behave as an inductive component in a π-configuration [124, 125] as shown in Fig. 5.3. The inductances are defined by:

$$L_{\mathrm{m}} = X_0/\omega \cdot \sinh \gamma l \tag{5.5}$$

$$L_{\mathrm{p}} = X_0/\omega \cdot \tanh \gamma l/2 \tag{5.6}$$

where l is the length of EVA channel and [124]:

$$X_0 = \frac{120\pi b}{W_{\mathrm{EVA}}\sqrt{\left(\frac{\lambda}{2W_{\mathrm{EVA}}}\right)^2 - 1}} \tag{5.7}$$

$$\gamma = \frac{2\pi}{\lambda}\sqrt{\left(\frac{\lambda}{2W_{\mathrm{EVA}}}\right)^2 - 1}. \tag{5.8}$$

The height of the channel is represented by b, λ represents the wavelength, and W_{EVA} the width of the EVA channel.

EVA waveguides do not normally allow propagation of RF signals or power. However, in the ON-state of this switch, the loading of the channel with dielectric posts – which behave as shunt capacitors – in unison with the π-connected inductors of the EVA waveguide lumped model will effectively form a filter response with J-inverters where $J = 1/\omega L_{\mathrm{m}}$. Fig. 5.3 shows a general filter model with two resonators (filter poles) coupled with an inductive π-network J-inverter.

In even-mode excitation, i.e., when a magnetic wall (open circuit) is inserted at the blue dotted reference plane in Fig. 5.3, the resulting resonant frequency can be calculated using the method detailed in [126] as:

$$f_{\mathrm{m}} = \frac{1}{2\pi\sqrt{\frac{L_{\mathrm{m}}L_{\mathrm{p}}}{L_{\mathrm{m}}-L_{\mathrm{p}}}C_{\mathrm{p}}}}. \tag{5.9}$$

Likewise, in odd-mode excitation i.e. when an electric wall (short circuit) is inserted instead, the resonant frequency is computed with:

$$f_{\mathrm{e}} = \frac{1}{2\pi\sqrt{\frac{L_{\mathrm{m}}L_{\mathrm{p}}}{L_{\mathrm{m}}+L_{\mathrm{p}}}C_{\mathrm{p}}}}. \tag{5.10}$$

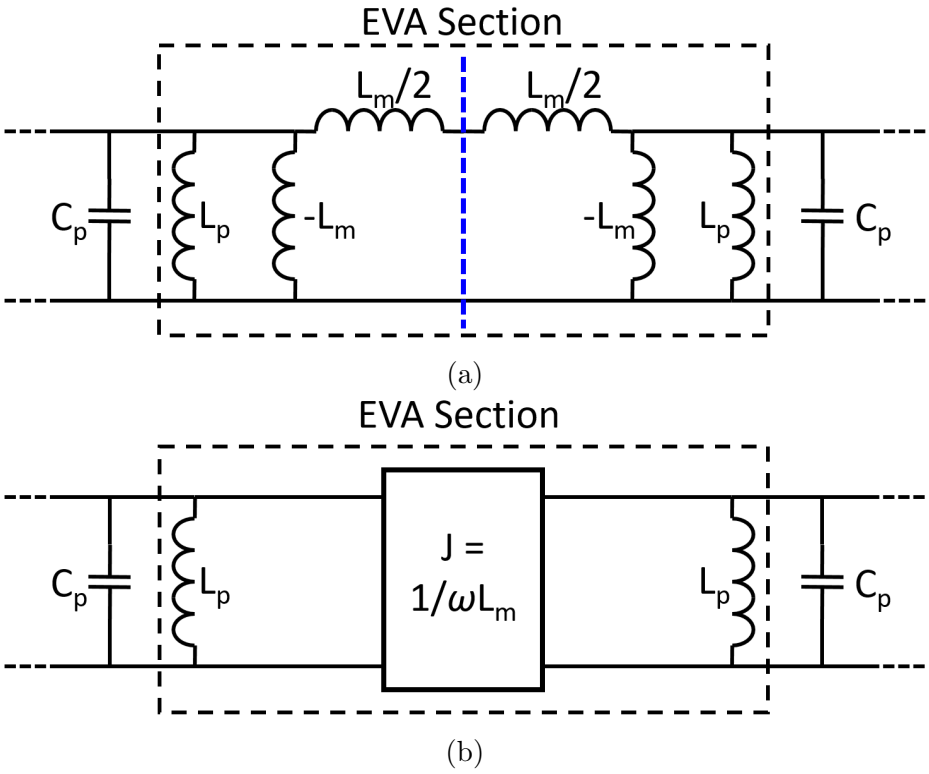

Figure 5.3: The equivalent lumped circuit model of an EVA waveguide section loaded with two dielectric posts at each end. (a) A transmission line section of an EVA guide can be represented by a π-network of inductors whose values vary by the length and width of the section. (b) With the dielectric posts that create a capacitance C_{p}, the evanescent guide effectively forms a two-pole J-inverter coupled bandpass filter response where $J = 1/\omega L_{\mathrm{m}}$.

As the inverter inductance L_{m} approaches a very large value in (5.9) and (5.10), both f_{m} and f_{e} converge to $1/2\pi\sqrt{LC_{\mathrm{p}}}$, the natural resonant frequency of a single uncoupled resonator. Conversely, as L_{m} decreases, f_{m} and f_{e} will diverge indicating an increase in coupling between the resonators. Since L_m is proportional to $sinh\ \gamma l$, it can be inferred that the inter-resonator coupling (k) which can be extracted using $k = (f_{\mathrm{e}}^2 - f_{\mathrm{m}}^2)/(f_{\mathrm{e}}^2 + f_{\mathrm{m}}^2)$, increases with the decrease in length of the EVA channel in between two dielectric posts. Additionally, it can be seen from (5.9) and (5.10) that f_{e} is a higher frequency than f_{m} which is indicative of magnetic coupling between the dielectric posts [126].

In order to couple energy to the bandpass filter response in a practical switch's

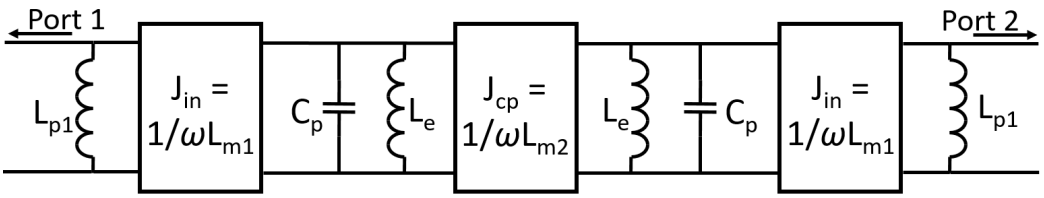

Figure 5.4: The equivalent J-inverter circuit model of the proposed 2-pole photoconductive EVA waveguide switch.

ON-state, a short length of EVA waveguide (l_{in}) needs to run between the waveguide feed and the first resonating post as shown in Fig. 5.2. The final equivalent J-inverter circuit is shown in Fig. 5.4. The resulting inductive components from the three EVA sections are defined as follows [124]:

$$\omega L_{\mathrm{m(n)}} = \sinh \gamma l_{\mathrm{n}} \tag{5.11}$$

$$\frac{1}{\omega L_{\mathrm{p(n)}}} = \coth \gamma l_{\mathrm{n}} \tag{5.12}$$

$$\frac{1}{\omega L_{\mathrm{e}}} = \frac{1}{\omega L_{\mathrm{p1}}} + \frac{1}{\omega L_{\mathrm{p2}}} = \coth \gamma l_1 + \coth \gamma l_2. \tag{5.13}$$

For the distance between posts $l_2 = l_{\mathrm{cp}}$ [124]:

$$\sinh \gamma l_2 = \frac{\delta \sqrt{g_1 g_2}}{\mathrm{FBW}(\coth \gamma l_1 + \coth \gamma l_2)}. \tag{5.14}$$

For the input coupling length $l_1 = l_{\mathrm{in}}$ [124]:

$$\sinh \gamma l_1 = \sqrt{\frac{\delta g_1 R'}{\mathrm{FBW}(\coth \gamma l_1 + \coth \gamma l_2)}} \tag{5.15}$$

where g_1 and g_2 are polynomial coefficients for filter prototypes (Chebyshev, Butterworth etc.), R' is the feed waveguide impedance, and [124]:

$$\delta = \frac{2}{1 + \frac{1}{1 - \left(\frac{2W_{\mathrm{EVA}}}{\lambda_0}\right)^2}}. \tag{5.16}$$

5.2 Limitations and Trade-Offs

The dimensions of the EVA channel, input coupling length, and coupling distance between posts all have performance trade-offs in the proposed switches. In [94], two EVA waveguide switch designs were presented: one where low ON-state insertion loss (IL) was prioritized while sacrificing OFF-state isolation, and another where OFF-state isolation was prioritized while having higher ON-state IL. In this section, an in-depth study of the engineering trade-offs for the two-pole switch dimensions (l_{in}, l_{cp}, d_{Si}, and W_{EVA} in Fig. 5.2) is presented. All studies use a silicon conductivity of 0.1 S/m and sputtered copper conductivity of 2.3×10^7 S/m.

5.2.1 EVA Channel Width and Silicon Post Diameter

A parametric study of the EVA channel width (W_{EVA}) is shown in Fig. 5.5. The loss of the structure can be computed from $Loss(dB) = \text{-}10\log\,(1 - Loss)$, where $Loss = 1 - |\text{S}_{11}|^2 - |\text{S}_{21}|^2$ [127]. Fig. 5.5(a) demonstrates that as W_{EVA} increases, the switch has lower loss in its ON-state, but becomes more absorptive (lossy) in the OFF-state. The more W_{EVA} is decreased, the closer the OFF-state of the switch approaches an ideal short-circuit, as shown in Fig. 5.5(b).

From (5.6) – (5.8), it can be seen that the shunt inductances (l_{p}) will decrease with narrower EVA channels (W_{EVA}). This will result in an upshift in operating frequency. Furthermore, according to (5.8) and (5.14), the fractional bandwidth (FBW) of the switch will be reduced as W_{EVA} decreases. In the OFF-state of the switch, a narrower W_{EVA} yields higher isolation due to a greater impedance mismatch at a given optical power with the EVA waveguide region further in cutoff [95].

To increase the FBW of an EVA waveguide switch, W_{EVA} must increase, but doing so will cause a downshift in operating frequency unless the silicon post diameter (capacitive loading) is decreased to compensate. From Fig. 5.6, decreasing the post diameter generally decreases ON-state loss, but also decreases the reflectivity of the

OFF-state. Therefore, it can be concluded that there is a fundamental trade-off between the ON-state IL and FBW with the OFF-state reflectivity and isolation of the switch.

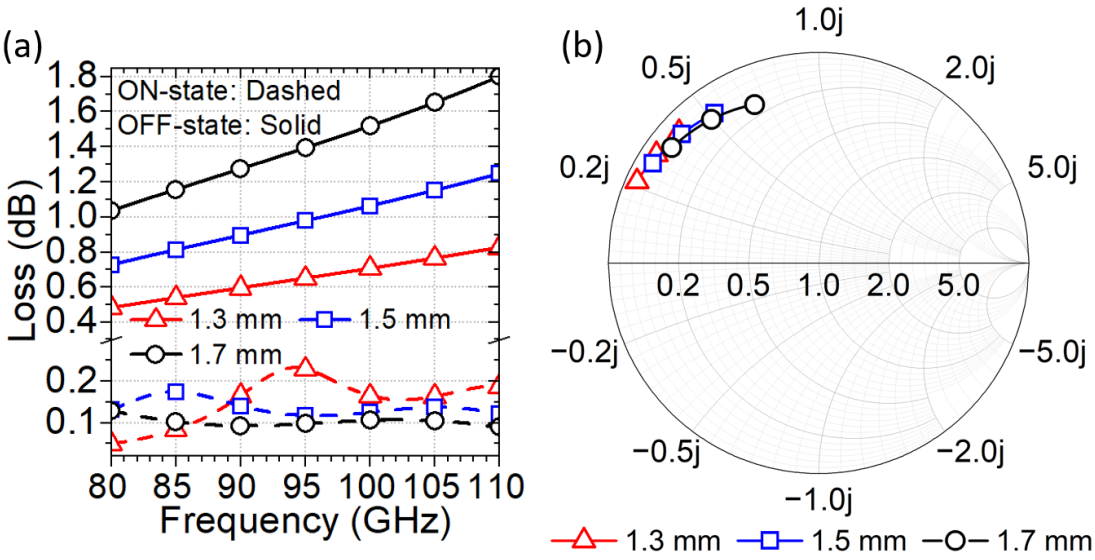

Figure 5.5: A parametric study of the effect of W_{EVA} on switch performance. (a) The loss of the switch in the ON-state and OFF-state. (b) The input impedance of the switch in the OFF-state.

5.2.2 Input Coupling

A parametric study of the input coupling distance, l_{in} (between the start of the EVA waveguide and the center of the first post), is shown in Fig. 5.7. In Fig. 5.7(a), the power dissipation in the ON-state increases with l_{in}, but decreases in the OFF-state as l_{in} is increased. In Fig. 5.7(b), while decreasing l_{in} makes the OFF-state of the switch less inductive, it also makes it less reflective, as the resistive post is moved closer to the input port of the switch.

A plot of the external quality factor (Q_{e}) versus l_{in} is shown in Fig. 5.8, obtained from detuning the post adjacent to port 2 in Fig. 5.2 and extracting Q_{e} using the method in [128]. Clearly increases in l_{in} result in an increase in Q_{e} corresponding to a decrease in input coupling. From (5.15), an increase in $l_1 = l_{\text{in}}$ will result in a decrease in resonator FBW due to a reduction in loading from the input ports.

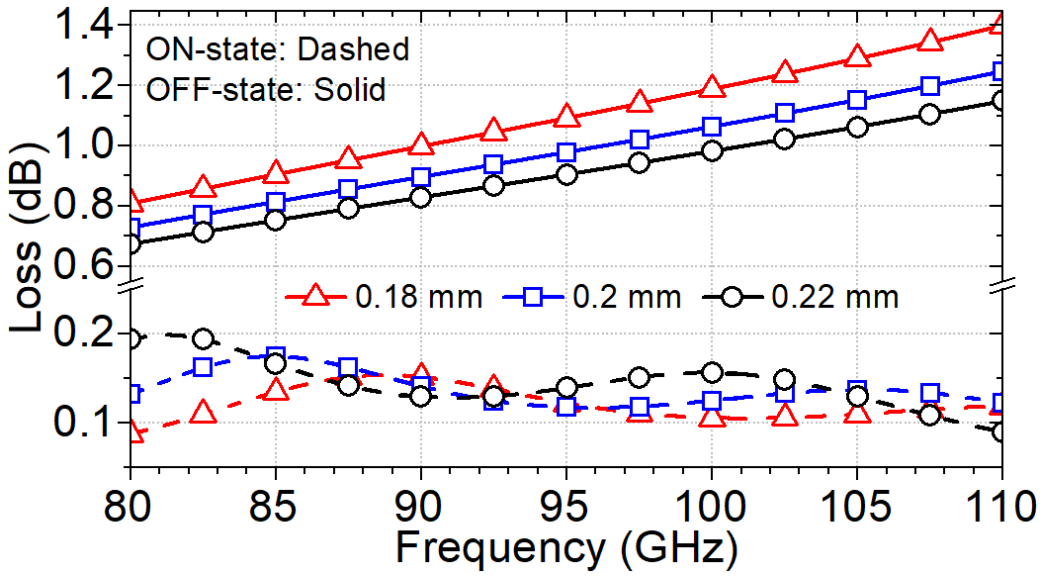

Figure 5.6: A parametric study of the effect of the silicon post diameter (d_{Si}) on switch loss.

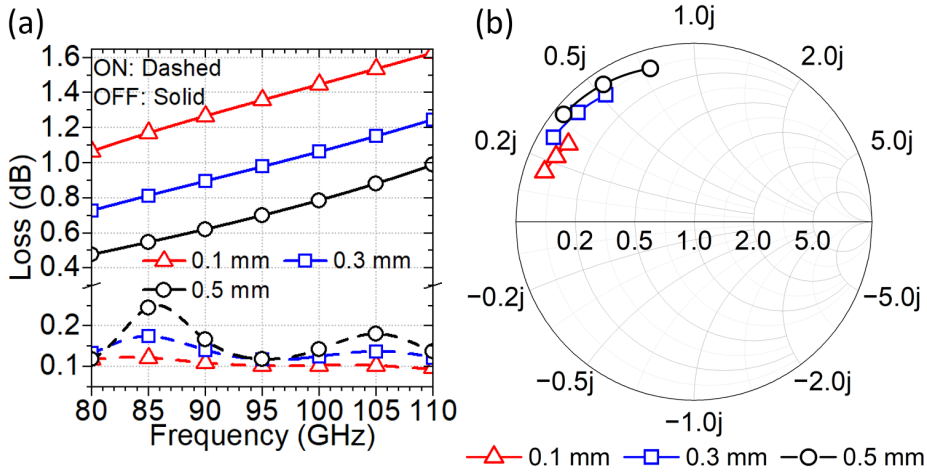

Figure 5.7: A parametric study of the effect of l_{in} on switch performance. (a) The loss of the switch in the ON-state and OFF-state. (b) The input impedance of the switch in the OFF-state.

5.2.3 Inter-Resonator Coupling

A parametric study of the distance between two resonating posts (l_{cp}) is shown in Fig. 5.9. By decreasing the distance between the posts, the power dissipated by the switch is reduced in both the ON-state and OFF-state. Note that a Smith chart was not shown for this study as it was found that there was very little variation in the OFF-

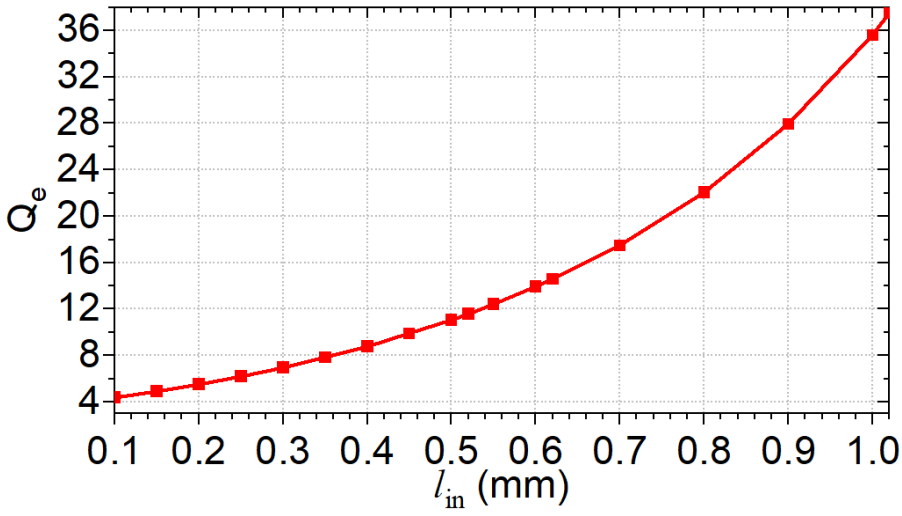

Figure 5.8: A plot of the effect of l_{in} on the external quality factor (Q_e).

state input impedance across different l_{cp} since most of the power is already reflected by the first post the incident signal encounters. From (5.14), increasing $l_2 = l_{\text{cp}}$ will decrease the FBW which is consistent with the phenomena observed in (5.9) and (5.10) where f_{e} and f_{m} converges with an increased l_{cp}. Fig. 5.10 demonstrates that this increase in l_{cp} corresponds to a decrease in the inter-resonator coupling between the posts, which is also consistent with observations from (5.9), (5.10), and (5.14).

Therefore, in order to increase FBW, the coupling between posts should be increased. However, the input coupling must also be increased in order reduce the ripple that will be introduced in between f_{e} and f_{m} as they move further apart. Based on the studies in Sections 5.2.2 and 5.2.3, it is once again observed that the proposed switch has fundamental trade-offs between ON-state loss and FBW with OFF-state reflectivity and isolation. The switch's FBW is fundamentally limited by how much isolation is desired in the design.

5.3 Design

With the proposed switches' principle of operation and fundamental trade-offs and limitations established, we will now discuss the practical implementation of the

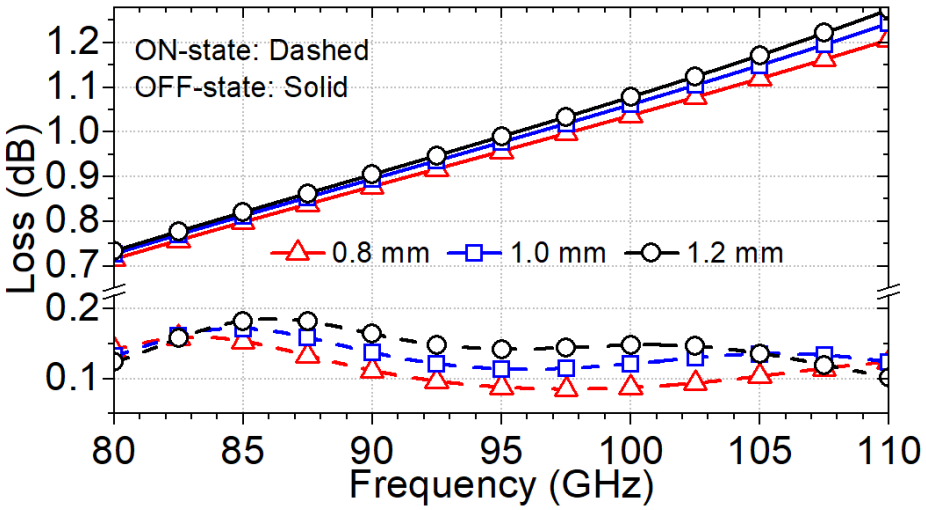

Figure 5.9: A parametric study of the effect of l_{cp} on the ON and OFF-state loss of the switch.

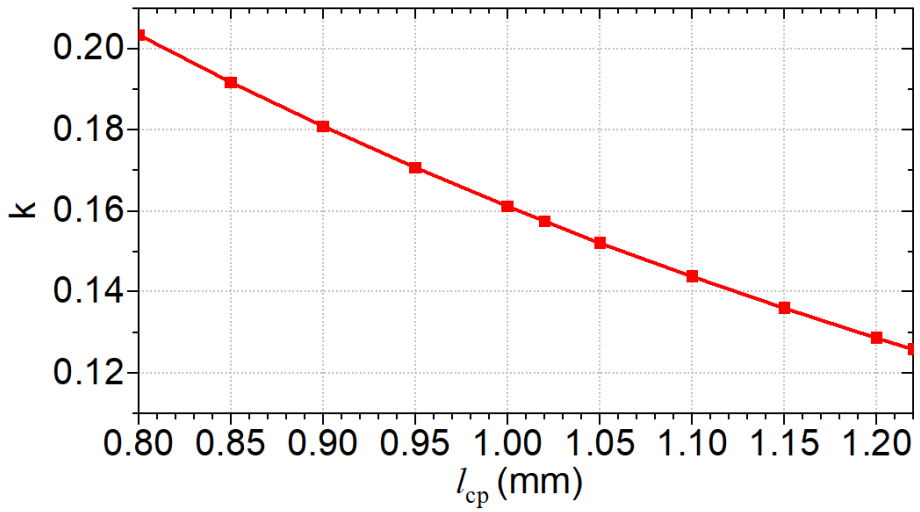

Figure 5.10: A plot of the effect of l_{cp} on the coupling coefficient (k).

device as well as the design of an SPDT version. Fig. 5.11 depicts the longitudinal cross-section of the two-pole SPST switch implementation proposed in this section. The switch channel and posts are formed by etching a 200 µm cavity into a 300 µm 10 kΩ·cm high resistivity silicon (HR-Si) wafer. This device wafer is then sandwiched with an 800 µm Si transition wafer – with cavities etched on both sides – which serves both as an E-plane bend and impedance taper [101] between standard W-band WR-10 waveguide connectors and the 200 µm reduced height waveguides. The WR-10

flange connectors can be placed with an offset from the first transition cavity to allow for an extra degree of freedom when designing the impedance taper. 50 µm deep holes are etched on the backside of the device wafer to allow for optical fibers controlling the two states of the photoconductive switch to be fed into each silicon post.

The close-up side view of the stacked-wafer E-plane bend used to feed the devices proposed in this chapter is presented in Fig. 5.12 along with a 3D model in Fig. 5.13. The impedance taper can be designed with the following procedure using a full-wave EM simulator:

1. Start with two decreasing step heights that are smaller than the standard waveguide height ($b = 1.27$ mm), but greater than the height of the device channel (0.2 mm). In this design, the step closer to the standard flange is 500 µm thick and the next step is 300 µm. For a single transition wafer implementation, such as for this work, the steps must add up to the total thickness of the wafer (800 µm).

2. Offset each waveguide step and the device (s_0, s_1, and s_2) and adjust the longitudinal length of each step (b_0 and b_1) such that the coupling apertures decrease in size with each successive step. To start, the distances between the center of each aperture should be approximately a quarter-wavelength at midband. For the W-band, the midband of 92.5 GHz has a $\lambda/4$ of 0.81 mm as shown by the yellow lines in Fig. 5.12.

3. If there is a very narrow or no observable passband in the simulated response, the change in step thickness is most likely causing significant impedance mismatches between steps. Repeat steps 1 and 2 with new step heights.

4. Fine tune the transverse widths (a_0 and a_1), offsets, and lengths of the two steps until the desired return loss response is achieved.

The 3-D model, simulation, and measured result of the transition are shown in

Fig. 5.13. The length of line (8.15 mm) on the device wafer is the minimum length such that two standard WR-10 UG-387 waveguide connectors can fit on the fabricated design. This direct connection of the two transitions (i.e. a thru line) has a simulated and measured peak IL of 0.36 dB and 1.16 dB, respectively.

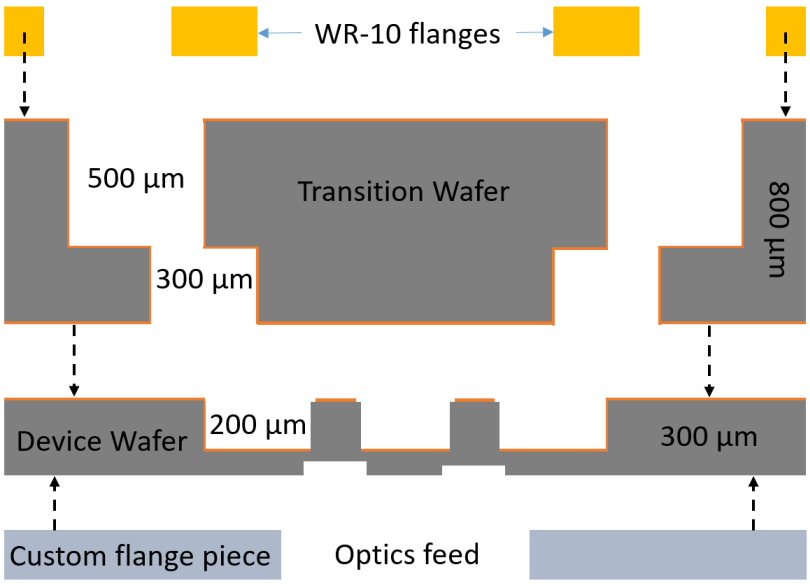

Figure 5.11: The exploded longitudinal cross-section of a silicon micromachined EVA waveguide switch. A 200 µm cavity is etched into a 300 µm HR-Si wafer to form the EVA channel and posts. Two cavities (500 and 300 µm deep) are etched in an 800 µm silicon wafer to form an E-plane bend and impedance taper that matches the 200 µm high device waveguide to standard WR-10 waveguide feeds. The device and transition wafers are sandwiched between WR-10 flange connectors and a custom laser cut sheet of stainless steel.

5.3.1 SPST EVA Switches With E-Plane Bend Transitions

The proposed switch's channel is embedded inside a 300 µm wafer. To create a functional component, we must now consider how to interface with the device. In [94] and [95], transitions to coplanar waveguides (CPW) were developed for a similar device. While the transition is useful for characterization purposes using ground-signal-ground probes, it is not suitable for use in practical systems since planar transmission lines have poorer power handling in the W-band. To fully maximize the power handling of this waveguide switch technology at the W-band and beyond, it

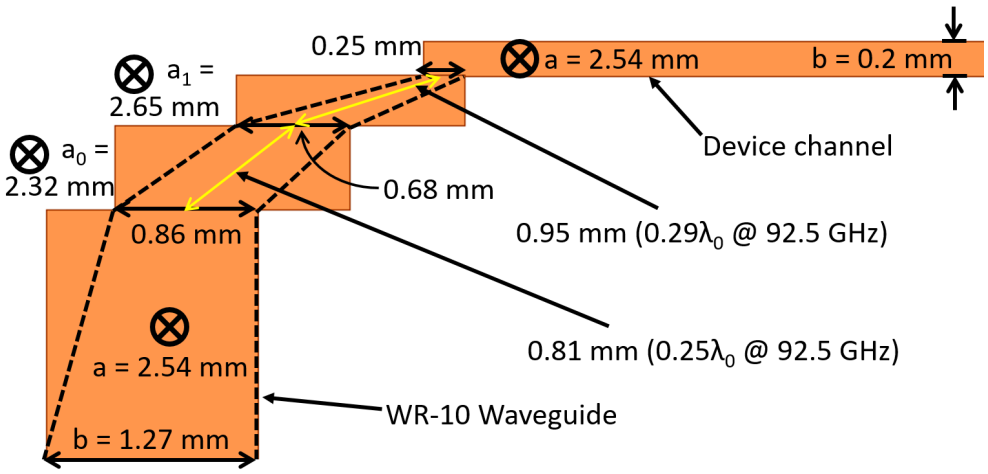

Figure 5.12: The side view of the E-plane bend used to feed the proposed SPST switches. The bend also acts as an impedance taper to match a WR-10 waveguide to the proposed devices which have a reduced height of 0.2 mm. The yellow arrows show the distance between the centers of the openings between each step.

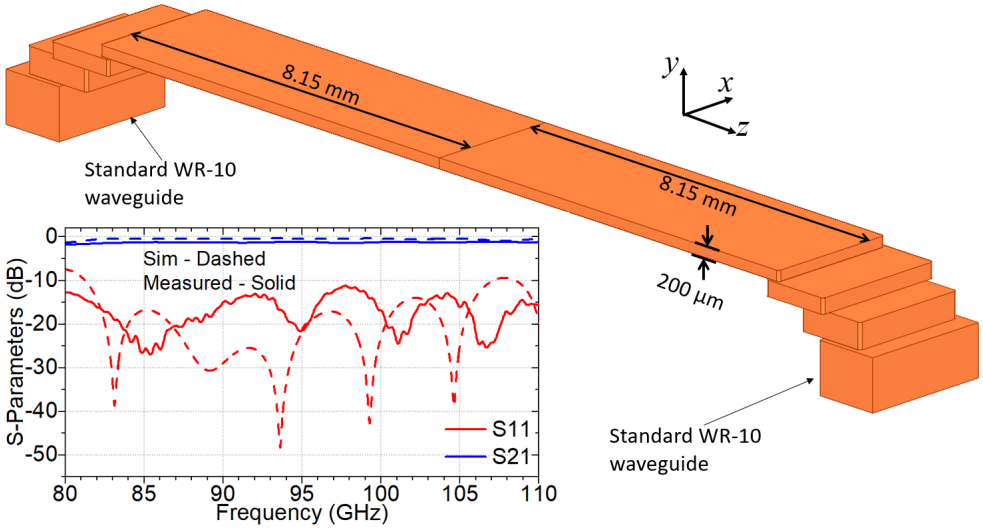

Figure 5.13: The 3D model, simulation, and measured results of the E-plane bend transition with a waveguide thru line. The total length of the thru line is the combined length of the transitions feeding the two ports of the devices shown in Fig 5.14 and Fig. 5.15.

is prudent that the entire system itself be fed, interconnected, and connectorized purely with waveguide structures. In this design, the switches are fed with standard WR-10 waveguides. Fig. 5.14 depicts a two-pole EVA switch with an E-plane bend. Note that the corners of each transition layer is rounded with a fillet radius of 50 µm to improve the power handling of the device. Likewise, the corners at the interface

between the 2.54 mm feed channel and 1.53 mm EVA channel have been rounded with a fillet radius of 150 µm. In Fig. 5.14 it can be seen that a return loss (RL) greater than 20 dB can be achieved across the entire 85 to 100 GHz design band with a total IL less than 0.6 dB. Furthermore, a minimum OFF-state isolation of 41.5 dB can be achieved in the design band.

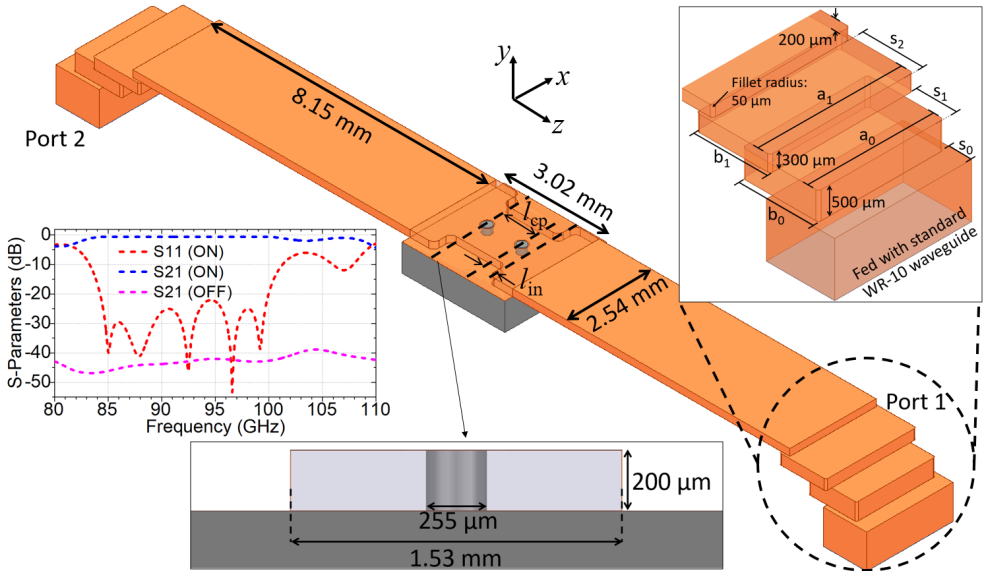

Figure 5.14: The 3D model of the proposed two-pole photoconductive EVA switch fed with E-plane bend transitions to standard WR-10 waveguides. Note that the top silicon layer has been rendered transparent to allow visibility inside the structure. The widths of the transition steps a_0 and a_1 are 2.32 mm and 2.65 mm, respectively, the length of the transition steps b_0 and b_1 are 1.41 and 1.37 mm, respectively, and step offsets s_0, s_1, and s_2 are 0.41, 0.73, and 1.12 mm. The distance between the two posts l_{cp} is 1.02 mm, and the input coupling length l_{in} is 0.3 mm. From simulation, it can be seen that a 20 dB return loss can be achieved spanning 85 to 100 GHz.

An EVA waveguide is normally in cutoff when no resonant structures are coupled inside the cavity and propagating fields decay exponentially since the propagation constant (β) becomes imaginary [7]. It can therefore be inferred that by increasing the length of the EVA channel, the OFF-state isolation can be improved. As can be seen from Fig. 5.15, the addition of a post and the overall increase in the EVA channel length allows greater than 60 dB isolation to be achieved up to 100 GHz. Furthermore, the ON-state response of the device resembles a three-pole bandpass

filter – note the additional ripple in the ON-state S_{11} response of Fig. 5.15 compared to Fig. 5.14 – which vastly increases the 10 dB RL fractional bandwidth (FBW): 19.5% (centered at 92.26 GHz) in the two-pole response is increased to 22.9% (centered at 91.58 GHz) in the three-pole response. The maximum IL in the 85 to 100 GHz design band is 0.74 dB, a relatively minor engineering trade-off for a significant improvement in isolation.

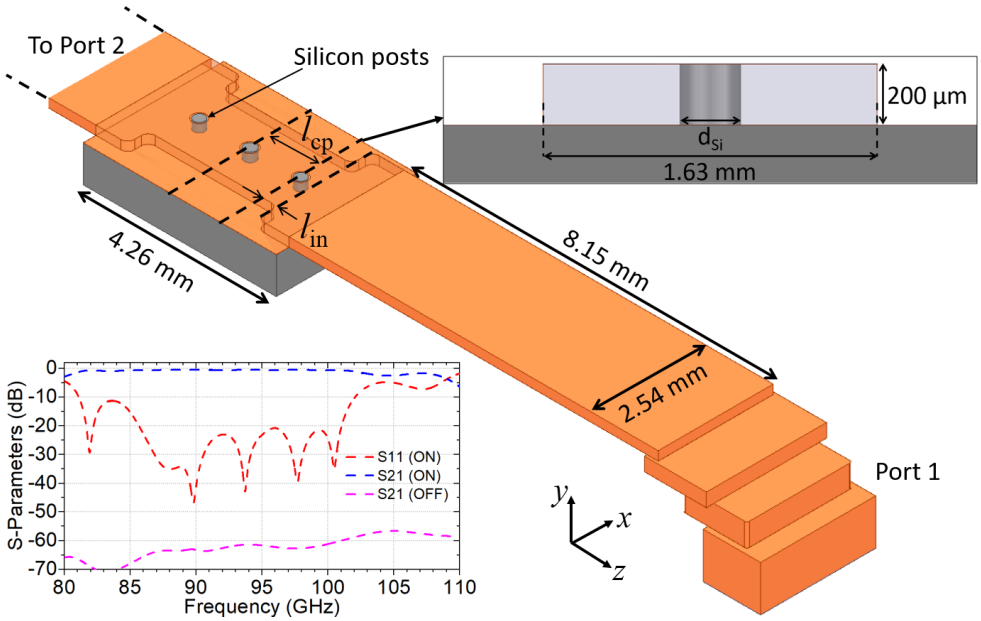

Figure 5.15: The 3D model and simulation results of the proposed three-pole photoconductive EVA switch with E-bend transitions to WR-10 waveguides. Note that the top silicon layer has been rendered transparent to allow visibility inside the structure. The E-bend transition dimensions are identical to those shown in Fig. 5.14. The diameter, d_{Si} is 0.26 mm for the center post and 0.24 mm for the two lateral posts. l_{cp} is 1.12 mm and l_{in} is 0.31 mm. The IL is less than 0.74 dB across the 85 to 100 GHz design band and can achieve greater than 60 dB OFF-state isolation.

5.3.2 Loss of the Transitions and the SPST Switches

The unloaded quality factor (Q_0) can also be extracted using the simulation model and results shown in Fig. 5.16. In this two-port method of extracting Q_0 [7], a single post is placed in the center of the EVA waveguide channel shown in Fig 5.14. The E-bend transitions are then removed and replaced by waveports directly feeding the full-mode reduced height waveguide segments. The resonator is then decoupled from

the input by increasing l_{in} to 10 mm. From the simulated S_{21} response in Fig. 5.16, the loaded quality factor (Q_{L}) can be computed as follows [7]:

$$Q_{\text{L}} = \frac{f_0}{f_2 - f_1} \tag{5.17}$$

where $f_2 - f_1$ represents to the half-power bandwidth of the resonator. This can then be used to obtain Q_0 as follows[7]:

$$Q_0 = (1 + g)Q_{\text{L}} \tag{5.18}$$

where:

$$g = \frac{S_{21}(\omega_0)}{1 - S_{21}(\omega_0)}. \tag{5.19}$$

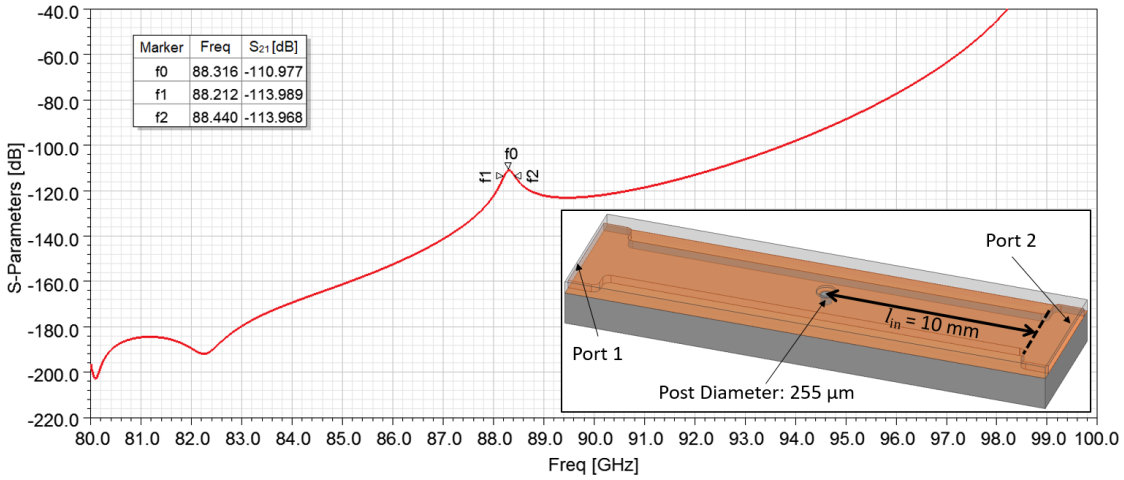

Figure 5.16: The 3D model of the setup and simulation results for extracting the external quality factor (Q_0) of a resonating post.

Using equations (5.17) – (5.19), we obtain a Q_0 of 510.5. While this number is significantly smaller compared to typical dielectric resonators that have Q_0 on the order of 50,000 [128], the designs presented in this chapter are for wider band application, and therefore do not require high frequency selectivity. As will be shown below, very low switch insertion losses can be achieved with these resonators.

Both SPST switch designs presented in Section 5.3.1 are fed with identical transitions. Since the thru waveguide and the SPST devices are fabricated on the same wafer, the IL obtained from Fig. 5.13 is assumed to be what is added to the switches fed by the same transitions. Subtracting 0.36 dB from the simulated peak ILs of the two-pole (0.6 dB) and three-pole (0.74 dB) SPST switches, we obtain 0.24 and 0.38 dB for the simulated IL of the respective switching elements.

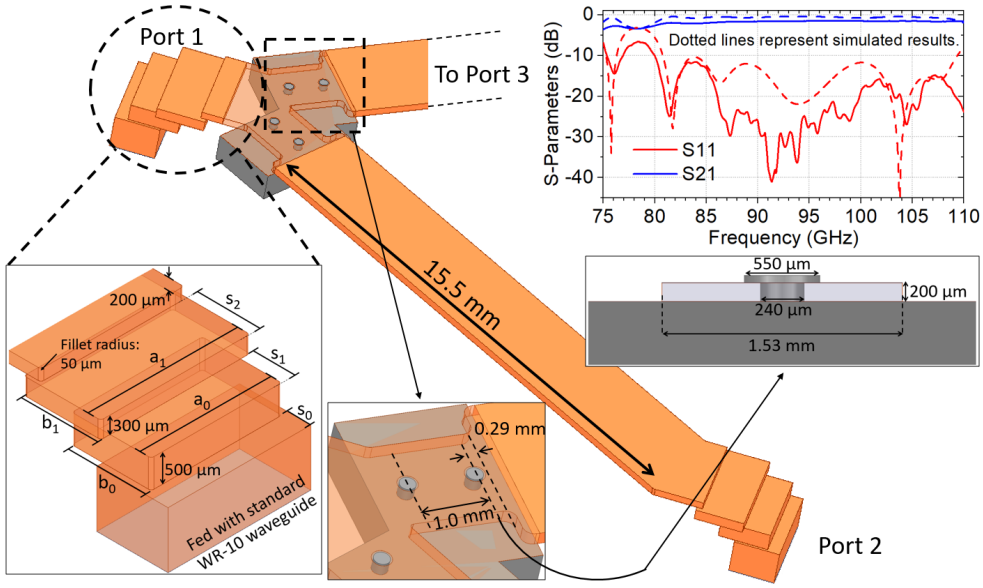

Figure 5.17: The 3D model and simulation results of the proposed two-pole photoconductive EVA SPDT switch with E-bend transitions to WR-10 waveguides. Note that the top silicon layer has been rendered transparent to allow visibility inside the structure. The graph shows the simulated and measured data of a 15.0-mm thru line with the E-bend transitions that branch off at the same angle as the proposed switch. The widths of the transition steps a_0 and a_1 are 2.4 mm and 2.8 mm, respectively, the length of the transition steps b_0 and b_1 are 1.39 and 1.35 mm, respectively, and step offsets s_0, s_1, and s_2 are 0.35, 0.74, and 1.2 mm.

5.3.3 SPDT EVA Switches With E-Plane Bend Transitions

An SPDT switch consists of a common port that is always connected to one of two output branches. Fig. 5.17 depicts the 3D model of an SPDT switch with one switching element per branch and two silicon posts per switching element. With power handling in consideration, all corners in the transitions and the device have

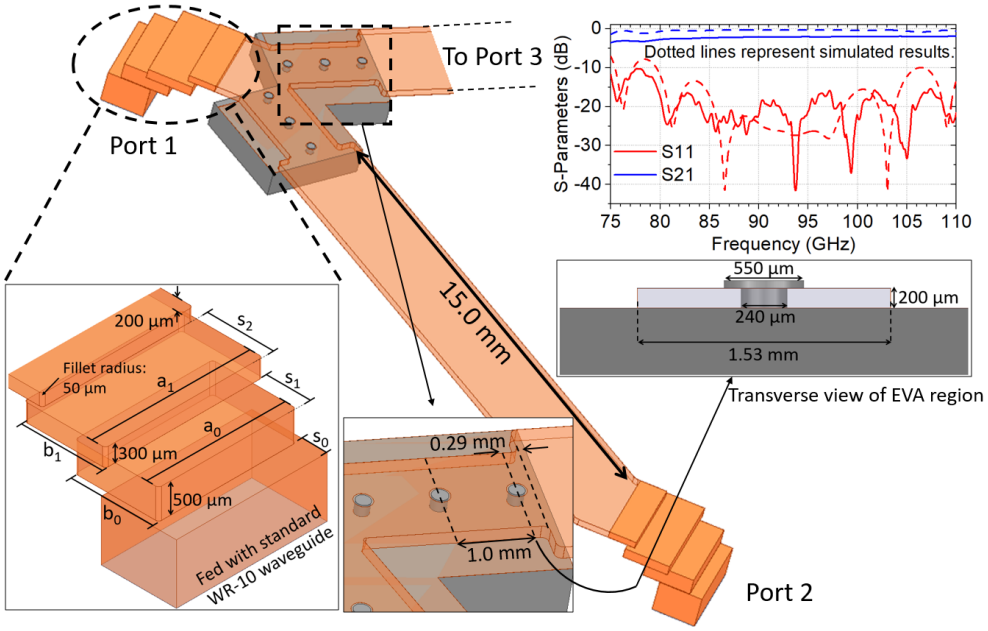

Figure 5.18: The 3D model and simulation results of the proposed two-pole photoconductive EVA SPDT switch with E-bend transitions to WR-10 waveguides. The graph shows the simulated and measured data of a 15.5-mm thru line with the E-bend transitions that branch off at the same angle as the proposed switch. The widths of the transition steps a_0 and a_1 are 2.5 mm and 2.9 mm, respectively, the length of the transition steps b_0 and b_1 are 1.4 and 1.33 mm, respectively, and step offsets s_0, s_1, and s_2 are 0.37, 0.72, and 1.11 mm.

been rounded with a minimum fillet radius of 50 µm. The angle (θ) between the two branches have been selected such that the two EVA channels can be placed directly against the transverse width of the common port feed (2.54 mm) and can be computed as follows:

$$\theta = 180^\circ - 2\sin^{-1}\left(\frac{a}{2W_{\text{EVA}}}\right) \tag{5.20}$$

where a is the width of the feeding waveguide (2.54 mm) and W_{EVA} is the width of the evanescent channel (1.53 mm) with the resultant angle between the two branches being 67.8°. The diagonal sections on ports 2 and 3 have to be extended to allow for all three required UG-387 connectors to fit on the fabricated device.

In the simulation, port 3 represents the isolated branch, where the silicon posts are photo-excited. The isolation between port 3 and the common port (port 1) is

greater than 43.5 dB across the 85 to 100 GHz design band. Simulation also shows that the signal propagation between the common and through port is no greater than 1.1 dB with a return loss at port 1 no less than 15.5 dB across the design band. The measured peak IL of the E-bend transitions with a 15.5-mm thru line is 1.5 dB redcompared to the simulated 0.47 dB. Using the same assumptions as in Section 5.3.2, the simulated IL of the switching element is 0.63 dB.

Likewise, the three post switch topology presented in Section 5.3.1 can easily be integrated into an SPDT configuration with some minor alterations to its dimensions. Fig. 5.18 illustrates the 3D model of the proposed photoconductive three-post SPDT switch. The EVA channel is wider than that of the two-post design and will result in a greater angle of separation between ports 2 and 3 (74.5°, calculated from (11)). The steeper bend angle results in a different input impedance at the ports and therefore the E-bend impedance transformer dimensions from the two-post design cannot be reused in contrast to their SPST counterparts. The measured peak IL of the E-bend transitions for the three-post design with a 15.0-mm thru line is 2.0 dB compared to the simulated 0.37 dB.

Similar to the single throw designs, the three-post SPDT design has significant improvements in isolation over the two-post design, achieving a minimum of 63 dB in the 85 to 100 GHz design band with a minor trade-off in IL. The maximum through IL in the design band is 1.19 dB, just a 0.09 dB increase over the two-post design. Using the same assumptions as in Section 5.3.2, the simulated IL of the switching element is 0.82 dB.

5.3.4 Power Handling Study of SPST Switches

With limitations of the available equipment to test the full-extent of power handling of the devices at the W-Band, it is prudent to estimate the failure modes using a full-wave simulator. Two of the possible failure modes of operating the SPST switches with high power is as follows: firstly, there is the possibility of electric breakdown

due to the electric field of the mode propagating in the waveguide approaching the limit of the material. In the case of air, it will be approximately 3 MV/m [129]. Secondly, there is the issue of the sputtered 1.2 µm metal films that form the walls of the waveguide channel failing due to high current densities which increase with RF power. It is known from literature that the critical current density of the metals used in the process (gold and copper) is 0.5 MA/cm^2 where it has been shown that exceeding this limit in MEMS switches will cause "electromigration, current bunching, and localized hot-spots", all of which can "result in quick thermal failure" [127]. This critical current density can be converted into a surface current density approximation by taking its product with the skin depth at 85.5 GHz (0.223 µm) which yields 1115 A/m.

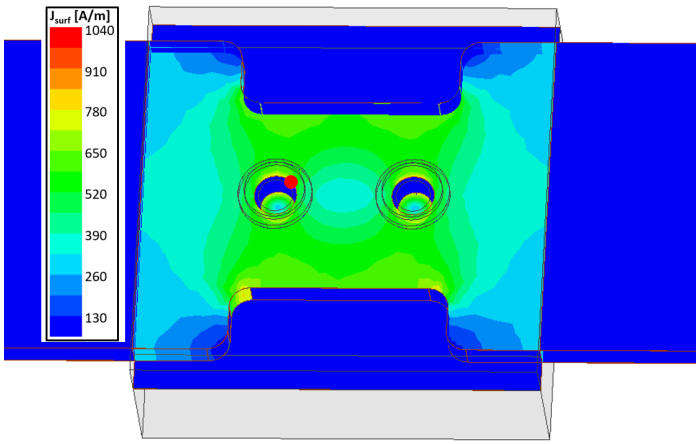

Figure 5.19: The simulated surface current plot of the proposed two post photoconductive SPST switch at 85.5 GHz with 5 W of input RF power for its ON-state. The red sphere marks the spot where the HFSS field calculator calculated the maximum surface current density in the structure to be 1070 A/m.

According to the field calculator feature in HFSS, the maximum electric field in the structure at 85.5 GHz is 2.599 MV/m which is below the electric breakdown field of air.

A plot of the simulated surface current density (J_{surf}) of the two post SPST switch is illustrated in Fig. 5.19. According to the field calculator, the maximum J_{surf} in the structure is located at the discontinuity in the center of the metallic roof of the

waveguide where the silicon posts are located. At 5 W of input power, the value of J_{surf} at this location is 1070 A/m which is approaching the theoretical limit of 1115 A/m. In the OFF-state of the device, the electric field and J_{surf} at 5 W was calculated to be 1.287 MV/m and 772.3 A/m, respectively. It can therefore be inferred that the theoretical maximum power handling of this particular structure is approximately 5 W and device failure is most likely to be due to ON-state current.

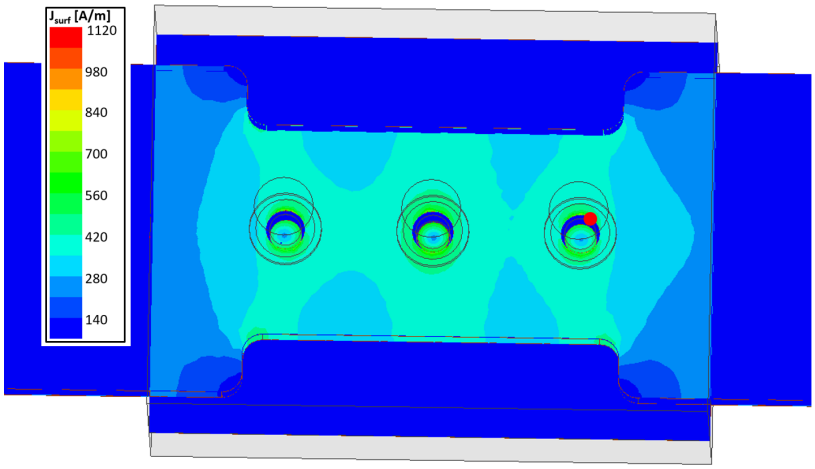

Figure 5.20: The simulated surface current plot of the proposed three post photoconductive SPST switch at 85.5 GHz with 2.9 W of input RF power for its ON-state. The red sphere marks the spot where the HFSS field calculator calculated the maximum surface current density in the structure to be 1097 A/m.

Likewise, the surface current density plot for the ON-state of the three-post photoconductive switch is shown in Fig. 5.20. Once again, the maximum J_{surf} can be shown to be at the conductor discontinuity where the silicon posts are etched is 1097 A/m at 2.9 W of input RF power. By contrast, the electric field is 1.529 MV/m which is well below the 3 MV/m. In the OFF-state, the maximum electric field and J_{surf} was calculated to be 0.688 MV/m and 891.8 A/m at 85.5 GHz. Once again, it can be inferred that the theoretical maximum power handling of the proposed three-post switch is approximately 2.9 W with its first failure mode due to ON-state current. From this study, it is clear that the key enabling higher power handling in future designs lies in depositing higher conductor thicknesses.

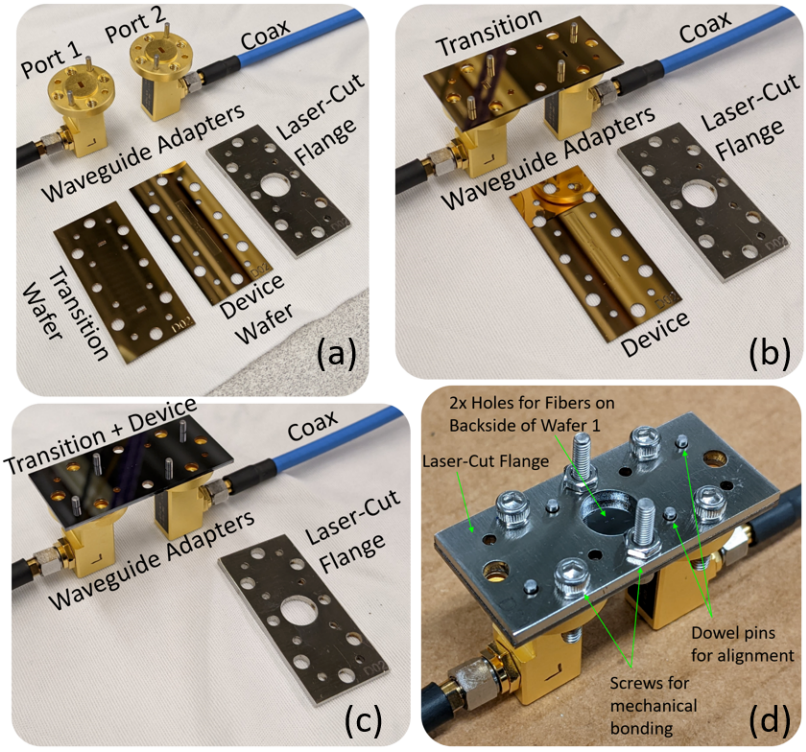

Figure 5.21: Pictures of the assembly of the two-pole SPST EVA photoconductive waveguide switch. (a) Picture before assembly, (b) transition wafer placed on the waveguide adapters and aligned using dowel pins, (c) device wafer placed on top of transition wafer, (d) the final assembled two-pole SPST EVA photoconductive waveguide switch.

5.4 Assembly

Fig. 5.21(d) shows the assembly and final experimental prototype of a two-pole SPST EVA photoconductive waveguide switch. Alignment is achieved using the dowel pins standard on UG-387/U waveguide flange connectors slotted into the smaller through holes etched using standard silicon deep reactive ion etching (DRIE) processes into both the transition and device wafers, and laser cut into the custom stainless steel flange piece. The microfabrication of the devices was outsourced to a contractor by Jones Microwave Inc. Fig. 5.21(a)-(c) shows the assembly of the switch. The transition wafer is first placed onto the waveguide adapters through the dowel pins located on the adapter flanges. The device wafer is then placed on top of the transition wafer, again using the dowel pins, aligning both wafers to each other and

the waveguide openings in the adapters. Finally, the laser-cut metal flange piece is placed on top, and screws are inserted through the larger holes to mechanically bind the wafers together, as shown in Fig. 5.21(d). The waveguide adapters are primarily used for characterization purposes, and are not part of the switch.

5.5 Experimental Results and Analysis

5.5.1 Small-Signal Results of the SPST Switches

The block diagram and photograph of the experimental setup for characterizing the S-parameters of the proposed switches are shown in Fig. 5.22. Frequency extender modules are used to allow small-signal characterization up to 110 GHz. Fiber optic cables are landed on the chip after the 1.0 mm coaxial to WR-10 adapters are torqued on to the device under test (DUT). The ON-state S-parameters of the two-pole SPST switch (with the laser switched off), and the OFF-state (with the laser switched on), obtained from the VNA are shown in Fig. 5.23. The device is able to achieve a 10 dB RL bandwidth spanning 82.1 GHz to 101.3 GHz with a peak ON-state IL of 1.34 dB (at 98.6 GHz) and minimum OFF-state isolation of 40.3 dB.

The experiment setup of the three-pole SPST switch is depicted in Fig. 5.24. Its measured results plotted in Fig. 5.25 show that it is able to achieve a peak IL of 1.39 dB (at 94.7 GHz) with at least 57.8 dB OFF-state isolation. The 10 dB RL bandwidth spans 80.4 to 102.5 GHz.

Since the thru line IL was shown to be around 1.16 dB, we can conclude that the majority of the loss in the aforementioned measurements are from the transitions. The extracted peak IL of the two and three pole SPST switches is therefore 0.18 and 0.23 dB, respectively.

In Fig. 5.26 and Fig. 5.27, the IL vs frequency at different optical powers are plotted for the two-pole and three-pole SPST switches, respectively. It can be seen from the corresponding group delay plots, that the response is relatively flat across

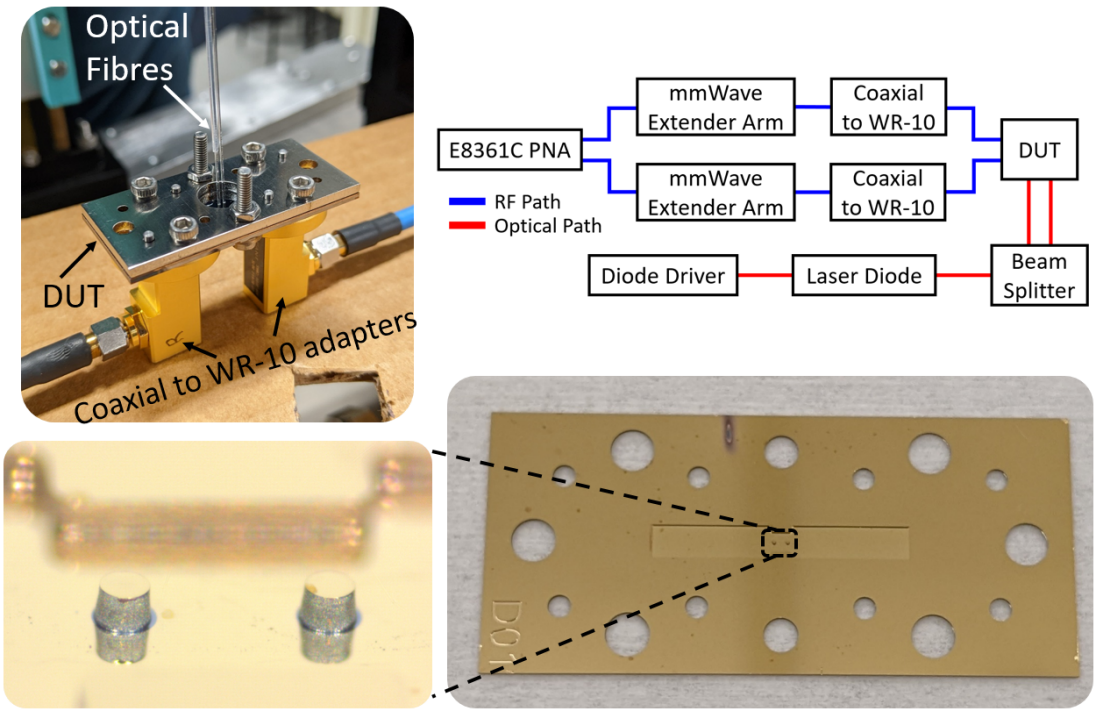

Figure 5.22: The block diagram and photographs of the experimental setup for measuring the S-parameters of the proposed two-pole SPST switch. The N5260 extender modules allow for RF characterization up to 110 GHz. An adapter is used to interface the 1.0 mm coaxial output from the extender modules to the WR-10 connectors on the device under test (DUT). The optical setup uses a Wavelength Electronics LD5CHA laser diode driver, a 915 nm laser diode from Sheaumann Laser Inc., an OZ Optics non-polarizing beam splitter, and two 400/440 µm multimode fibers. The size of the switch excluding transitions is 2.54 × 3.02 mm.

the pass band of the filter response, and this switch technology can therefore also have applications as tunable attenuators. A 30 dB isolation can be achieved with just 178 mW of optical power in the two-pole SPST switch. For its three-pole counterpart, this can be achieved with just 111 mW.

5.5.2 Small-Signal Results of the SPDT Switches

The experiment setup and microscope images of a two-pole SPDT switch is presented in Fig. 5.28. The two-pole SPDT switch presented in the original work [96], had silicon posts with an overcut profile. Following adjustments to the process control in refabrication the new device has a more vertical profile and the lower IL results

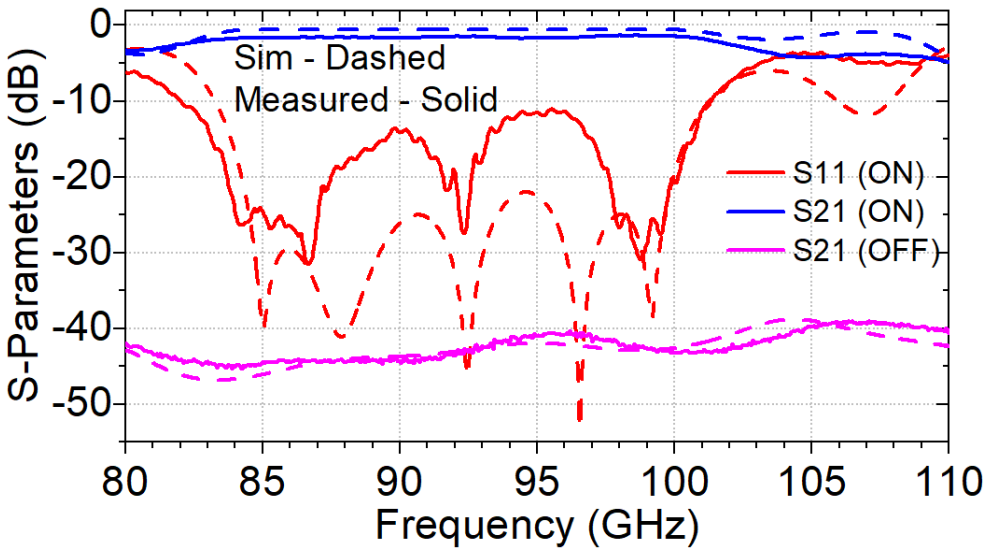

Figure 5.23: The measured and simulated results of the proposed two-pole SPST switch for both the thru and isolated states.

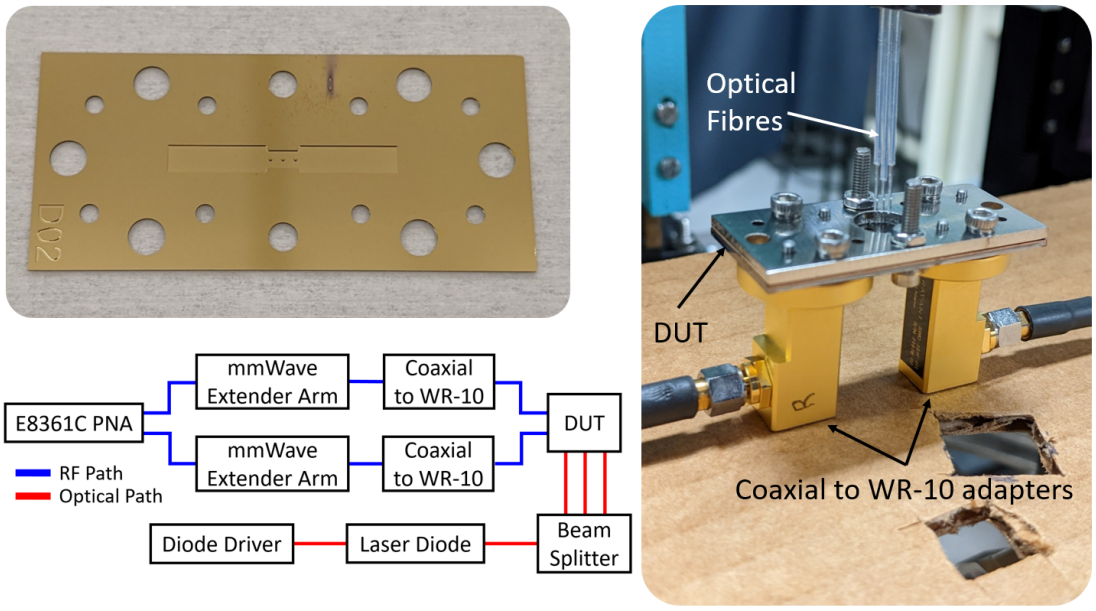

Figure 5.24: The experimental setup for the proposed three-pole SPST switch. The size of the switch excluding transitions is 2.54 × 4.26 mm.

are presented in Fig. 5.29. This refabricated device achieved a maximum thru branch IL of 1.66 dB. Since the measured IL of a thru line was around 1.5 dB, it can be concluded that the IL of the switching element itself is 0.16 dB. The design achieved a 22.8% 10-dB return loss fractional bandwidth (FBW) centered at 95.08 GHz and achieves greater than 40 dB isolation across this operational band.

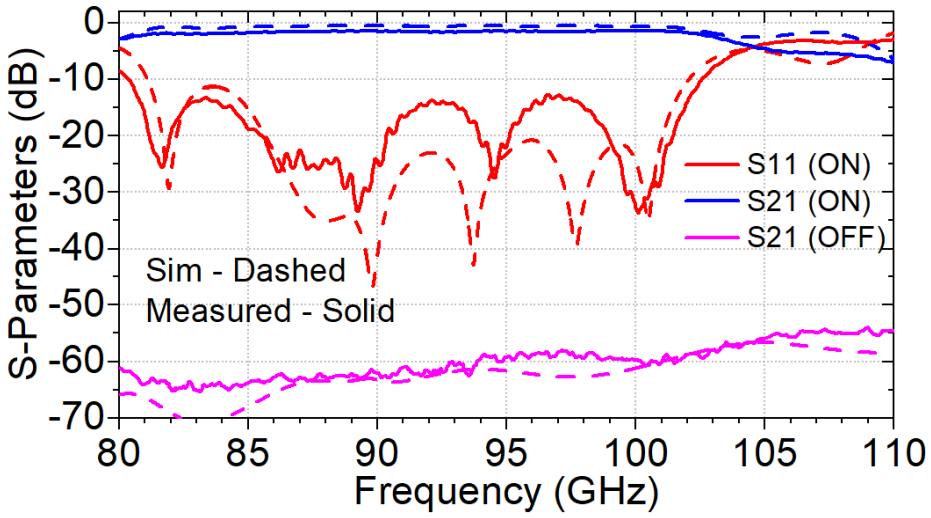

Figure 5.25: The measured and simulated results of the proposed three-pole SPST switch for both the thru and isolated states.

Likewise, the photograph three-post SPDT switch originally developed in this work is presented in Fig. 5.30 and it measured S-Parameters in Fig. 5.31. This device has a maximum IL of 2.32 dB. Since the measured IL of its corresponding transition with a thru line is 2.0 dB, it can be concluded that the IL of the switch itself is around 0.32 dB Furthermore, this device achieved a 10-dB FBW of 21.8% centered at 92.22 GHz and greater than 50 dB isolation from 82.8 GHz and above.

5.5.3 Power Handling Measurement of the SPST Switch

The measurement setup depicted in Fig. 5.32 was used to experimentally evaluate the power handling capabilities of the fabricated SPST switches. A series of amplifiers was used to boost the 85 GHz continuous wave (CW) signal from the mmWave module up to +37 dBm (5 W). A variable attenuator dial on the Keysight N5260-60003 mmWave head allowed the input power to be manually tuned. A circulator was placed after the power amplifier to protect it from reflected power in the event that the DUT fails. A power meter configured with a Keysight W8486A sensor was connected to the coupled port of a directional coupler to measure the power going into the DUT. The output of the DUT was then connected to a second directional

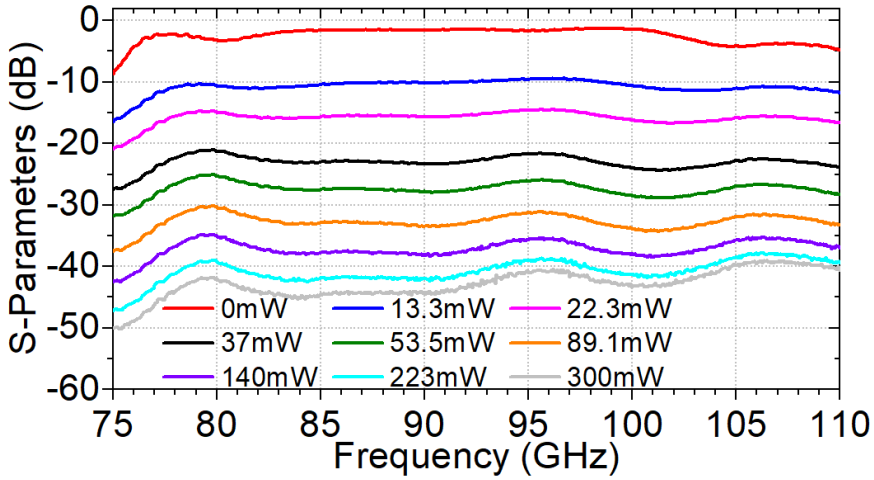

(a)

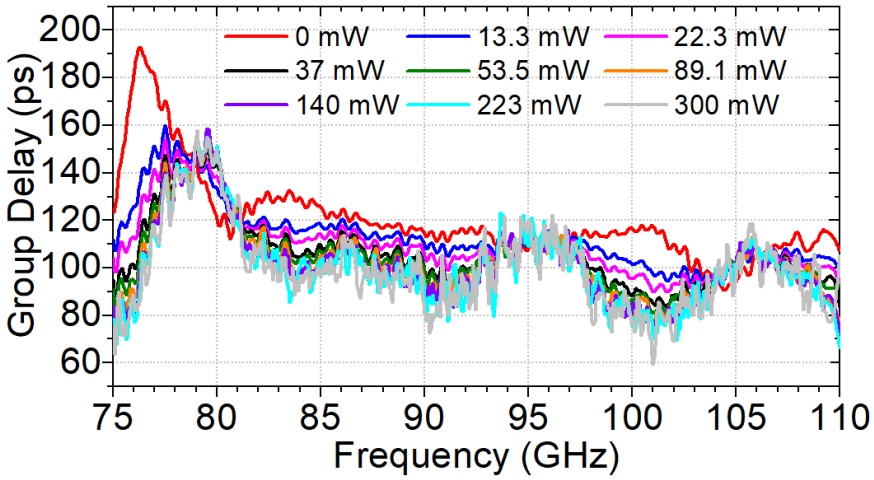

(b)

Figure 5.26: The (a) measured S_{21} responses at different powers of 915 nm optical excitation for the two-pole SPST switch; and (b) its corresponding group delay response.

coupler whose coupled port was fed into port 2 of the VNA. The depicted setup was capable of providing a maximum input power of +32 dBm (1.6 W) continuous wave (CW) at 85 GHz at the input of the DUT.

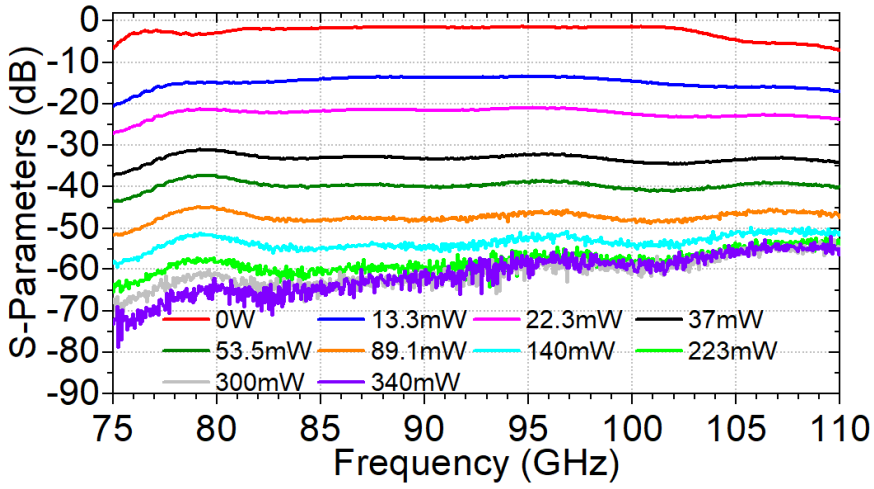

(a)

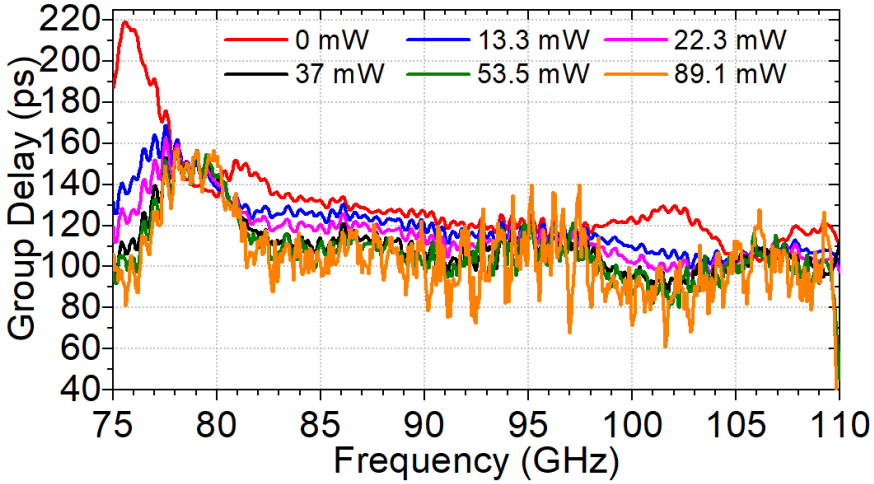

(b)

Figure 5.27: The (a) measured S_{21} responses at different powers of 915 nm optical excitation for the three-pole SPST switch; and (b) its corresponding group delay response.

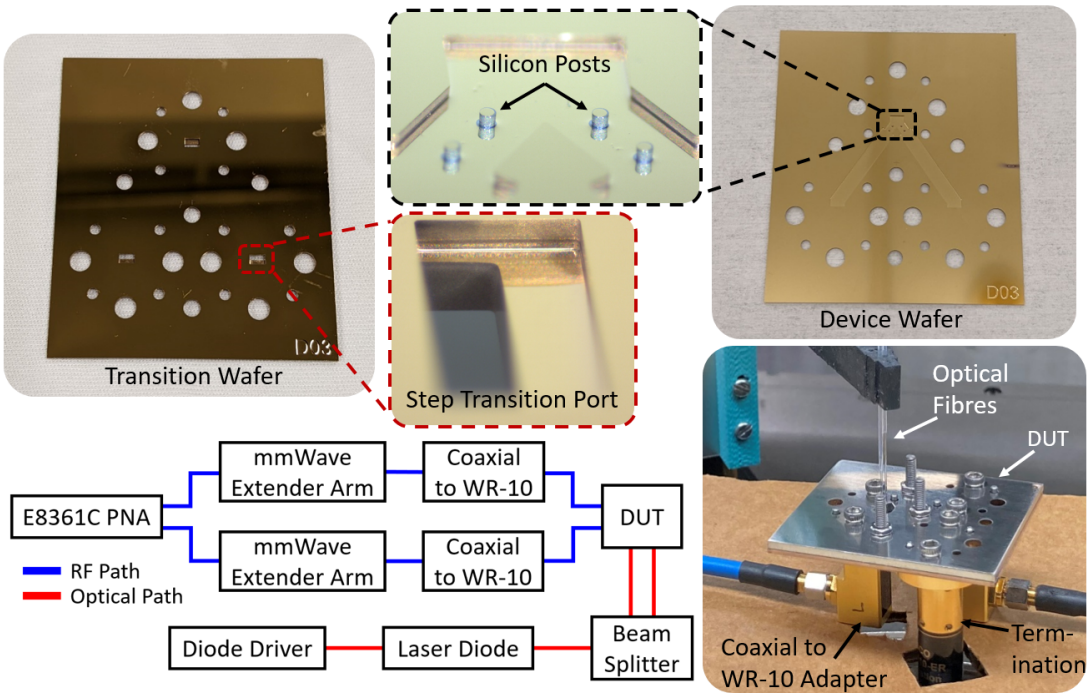

Figure 5.28: The assembly and experimental setup of the proposed two-pole SPDT switch.

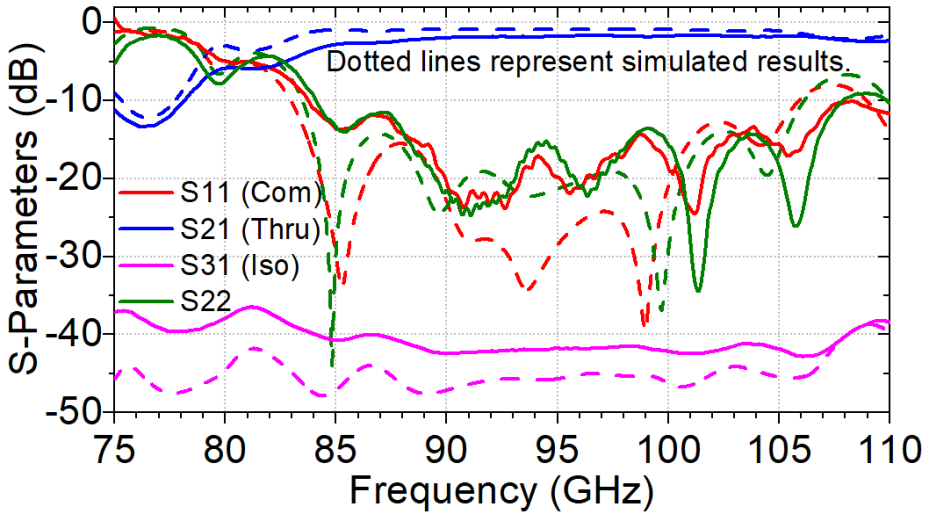

Figure 5.29: The measured and simulated results of the proposed two-pole SPDT switch.

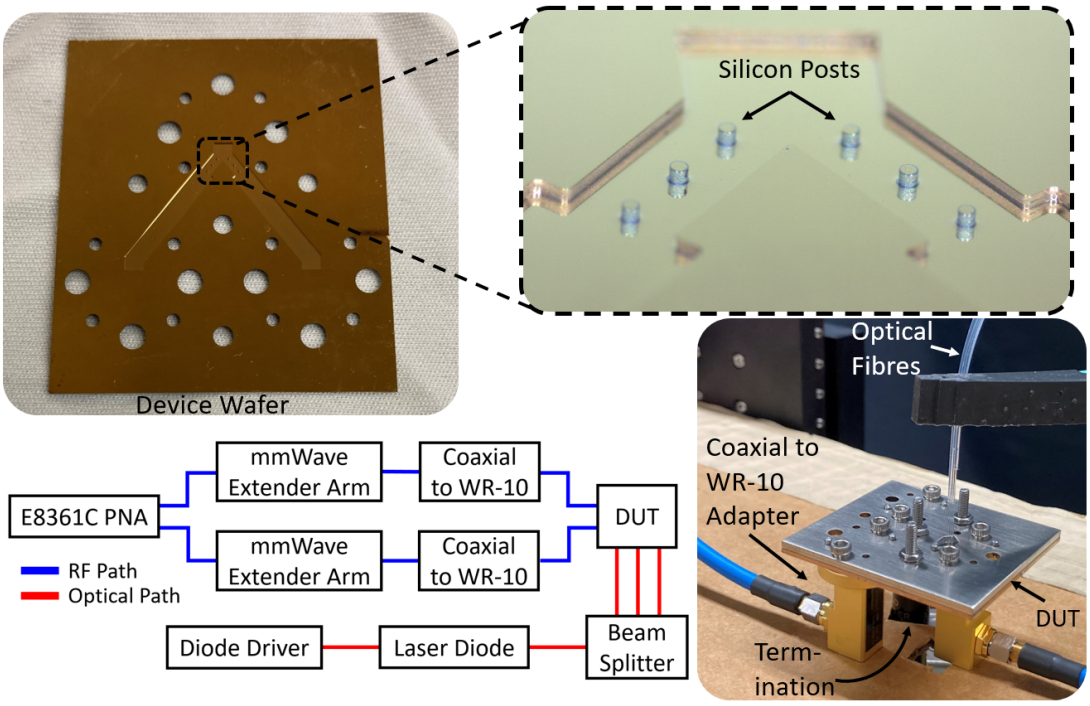

Figure 5.30: The experimental setup of the proposed three-pole SPDT switch.

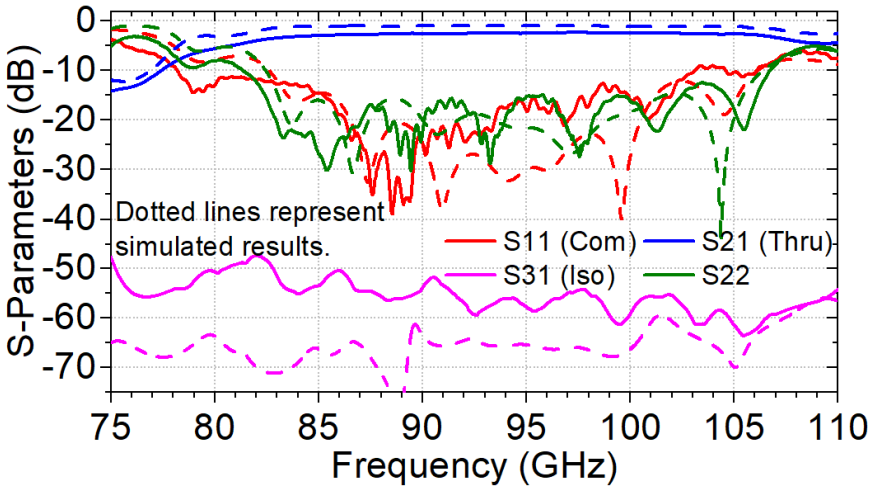

Figure 5.31: The experimental setup of the proposed three-pole SPDT switch.

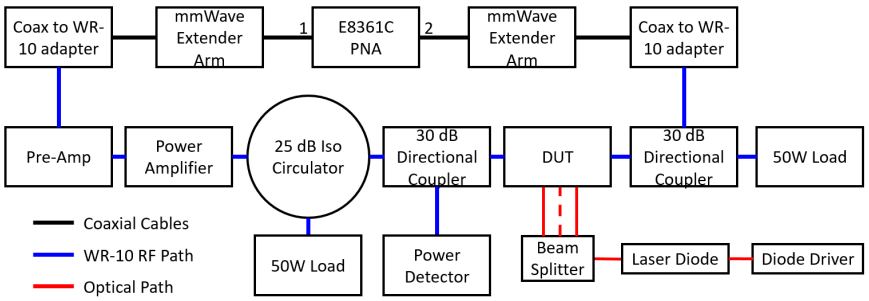

(a)

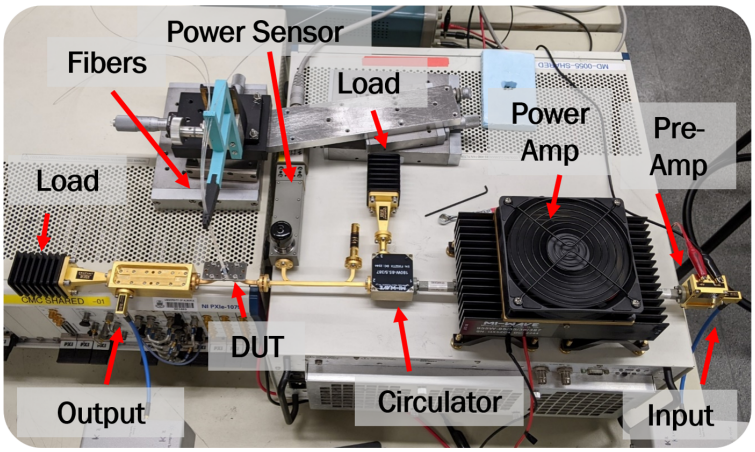

(b)

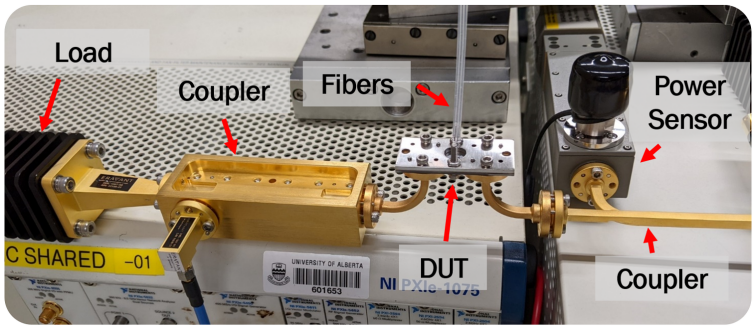

(c)

Figure 5.32: The high power setup. (a) The block diagram for evaluating the power handling capabilities of the fabricated SPST switches. The N5260-60003 has a variable attenuator that can be used to adjust the input power into the power amplifier and by extension, the DUT. A circulator connected to a 50 W termination is used to protect the power amplifier from reflected power should the DUT fail under testing. A power sensor and meter is used to detect and verify the input power into the DUT and a thru-reflect-load (TRL) calibration can be performed to extract the S-parameters of the switch at 85.5 GHz. (b) A photograph of the high power experiment setup. (c) A close-up photograph of the three-pole SPST switch in the high power setup. This setup was able to deliver a maximum of +32 dBm to the DUT.

Both the ON- and OFF-states of the two- and three-pole SPST switches were measured using the setup in Fig. 5.32. A close-up of the three-pole SPST switch is shown in Fig. 5.32(c). The switch was subjected to an initial incident power of +20 dBm at 85 GHz and the power was then gradually increased to the +32 dBm CW upper limit of the setup. The S-parameters of the two switches were then measured again at +20 dBm input power, and there were negligible differences to the data plotted in Fig. 5.23 and Fig. 5.25. This experiment was repeated five times, for both ON-state and OFF-states of the two- and three-pole SPST switches. We can therefore conclude that the switches can handle greater than 1.6 W of RF power. In simulation, it is expected that the two-pole and three-pole SPST switches can handle 5.0 and 2.9 W, respectively, and based on these simulations, the failure mode is expected to be due to the maximum current handling of the metal in the waveguide channel, not the silicon switching element itself, which has been shown in literature to be able to have excellent linearity and have a measured IP3 on the order of +68.8 dBm [99]. Furthermore, it was demonstrated in [99] that a planar silicon switching element can handle 100 W of RF power without any degradation in insertion loss nor isolation. It was also reported that there was no "gain compression up to 50 dBm (100 W)" [99], further suggesting that the limitations on using photoconductive switch technology in waveguides are due to electric breakdown and current handling which occurs at much lower powers than where non-linear effects become significant. By plating thicker metals in future implementations of this device, the waveguide switch is expected to be able to handle more power than what was initially designed in this thesis.

5.5.4 Switching Speed Measurement of the SPST Switch

A block diagram and photographs of the experimental setup for characterizing the switching speed of a SPST switch between 85 to 92.5 GHz are shown in Fig 5.33. Due to scheduling considerations at the time, similar light-activated EVA waveguide

SPST switches from Jones et al. in [95] with CPW to waveguide transitions, operating within the same band were characterized instead. An Agilent E8361C PNA and 110 GHz extender module head was configured to output a single frequency signal to a Cascade Microtech Infinity 110 GHz GSG probe which is landed on the CPW trace of the SPST switch. A second probe was landed on the other side of the device and was connected to a Keysight 110 GHz UXR1102A Infinium UXR-Series oscilloscope. A function generator was configured to output a square wave to modulate the laser diode with a period of 60 µs which has an internal rise/fall delay of 117.1 ns. A 915 nm ($h\nu$ = 1.36 eV, chosen for high quantum efficiency in Si [122]) SP-915-270 Sheaumann Laser Inc. laser diode with a pig-tailed 105/125 µm single-mode (SM) fiber was connected to an OZ Optics non-polarizing beam splitter where two of its 400/440 multi-mode (MM) output fibers are connected to the DUT (the fabricated SPST switch). A 3D printed structure was used to guide the unterminated fiber ends into backside holes etched above each Si post. A Wavelength Electronics FL591FL laser diode driver was used to drive the laser diode, which has a rise/fall time of 300 ns.

The laser modulated waveforms extracted from the UXR oscilloscope are shown in Fig. 5.34, displayed in red. The blue waveforms represent the signals from the FL591FL's built in current monitor pins with a transfer function of 5 mA/mV. Although the diode driver current never fully switches off, the monitor voltage of 50 mV corresponds to 250 mA which is half of the SP-915-270 laser diode's threshold current.

From the extracted waveforms at four measured frequency points, the average 10%-90% rise time and 90%-10% fall time is 3.83 µs and 1.43 µs, respectively. The maximum extracted rise and fall time from these measured frequencies are 4.00 µs and 1.55 µs, respectively. As can be seen from Table I, these results demonstrate that this technology shows significant promise in being a high-speed alternative to electromechanical RF switches, and lower loss, higher isolation alternative to PIN

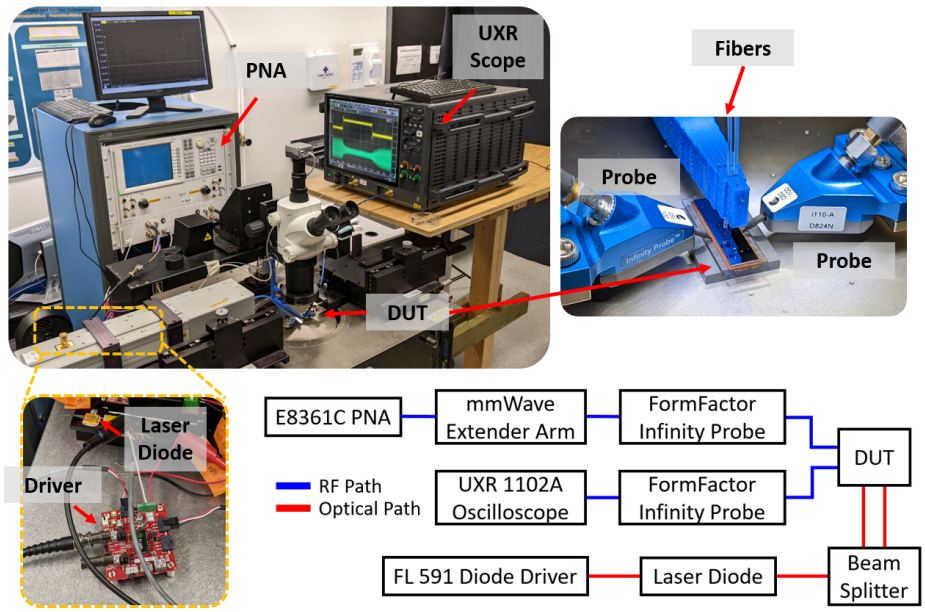

Figure 5.33: A block diagram and photographs showing the experimental setup for characterizing the rise and fall times of the silicon photoconductive SPST switch. The E8361C PNA was set to output single frequencies to the optical fiber modulated DUT (SPST switch). The resultant waveform was measured on a Keysight UXR-Series scope.

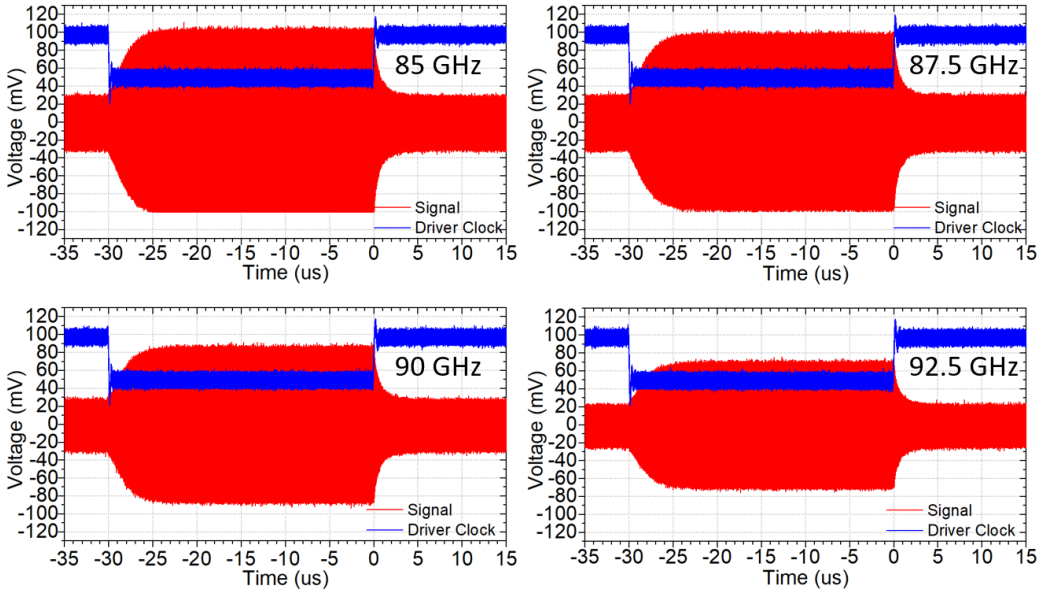

Figure 5.34: The time domain waveforms extracted from the Keysight UXR oscilloscope. The E8361C PNA was configured to output single tone waveforms at four different frequencies: 85, 87.5, 90, and 92.5 GHz.

Table 5.1: Comparison of the Proposed Three-Pole SPDT Switch With Current State-of-the-Art Solutions.

Ref.	Technology	Frequency Range (GHz)	10-dB RL FBW (%)	Peak IL (dB)	Isolation (dB)	Power Handling (dBm)	Switching Speed	Volume[c,d]
This Work	Photoconductive Si (Waveguide)	82.2–102.3	21.8	0.32	50	32[b]	4 µs[b]	53.62
[88]	Photoconductive Si (SIW)	74 – 85.8	15	2.2	30	Unknown	40 µs	35.5[e]
[83]	Electromechanical (Waveguide)	75 – 110[a]	37.8[a]	0.6[a]	55[a]	50	50 ms	> 203
[84]	PIN Diode (Waveguide)	68 – 79[a]	15[a]	1.4[a]	25[a]	10	50 ns	> 203
[130]	PIN Diode (SIW)	6.76 – 11.8	37	2.1	10	24	2 ns	2.02[e]

[a] Results reported include transition losses.
[b] Results extracted from two- and three-pole SPST switches.
[c] Excludes the dimensions of biasing circuitry / electromechanical rotors.
[d] Normalized to λ^3 in the respective material at the center frequency.
[e] Printed circuit board designs, not connectorized with waveguides.

diode switches. The fall time of the switch is dependent on the rate of carrier generation whereas the rise time is dependent on the rate of carrier recombination. Since recombination is generally a slower process, it is expected that the rise time longer than the fall time as is apparent from Fig. 5.34 [94].

In Table 5.1, the proposed three-pole is compared with other waveguide SPDT switches. The proposed design shows the lowest IL compared to other integrated waveguide solutions and has the highest isolation and power handling for solid-state mmWave switches. Furthermore, the proposed device has a vastly superior switching speed compared to electromechanical switches while only sacrificing 10 dB of isolation. Compared with other waveguide connectorized designs, the proposed SPDT switch also offers a significant reduction in device footprint. With improvements to the transition design, the total IL of devices developed using the proposed technology can easily compete with traditionally machined waveguide switches and the device volume can be even further reduced.

Finally, to scale this waveguide switch technology to lower frequency bands, both the width of the evanescent mode channel and the diameter of the posts will need to increase thus requiring more optical power to achieve the same levels of RF isolation presented here. As the size of standard waveguides increases at lower bands, it may be more practical to feed the devices with transitions to planar transmission lines

such as CPW as was demonstrated in [95] and [94]. It is also possible to integrate bulk silicon with SIW [87, 88] where fabrication with silicon micromachining is no longer practical with the physical scale of the waveguide devices.

5.6 Summary

In summary, this chapter demonstrated the capabilities and promise of silicon micromachined EVA photoconductive waveguide switches for mmWave technologies. In this expanded work, the design procedure and characterization of a W-Band photoconductive three-pole EVA variable attenuator and SPDT switch was presented which was shown to have significant improvements to the power requirements in achieving high isolation. The fabricated three-pole devices only requires a total continuous wave optical power of 110 mW to achieve a 30 dB isolation, a 38% reduction over a two-pole design. With 900 mW of total optical power, greater than 50 dB of isolation was achieved by the proposed three-pole design from 85 to 100 GHz compared to 40 dB achieved by the 2-pole design.

Furthermore, the refabricated 2-pole SPDT switch originally presented in [96] was shown to have an extracted IL of 0.2 dB, and its newly presented 3-pole counterpart having an extracted IL of 0.32 dB in the W-Band.

Additionally, this chapter presented the first ever switching speed and power handling characterization of this EVA waveguide switch technology. It was shown that the fabricated switches have a maximum 10-90 and 90-10 fall time of 4.00 µs and 1.55 µs, respectively. The 2-pole and 3-pole switching elements have also been shown to be able to handle +32 dBm of continuous wave RF power at 85 GHz in both their ON and OFF states.

The results show that silicon-micromachined photoconductive EVA waveguide switches maintain the low IL and high isolation of mmWave electromechanical switch while having a ten-fold improvement in switching speed. The proposed switches also demonstrate higher power handling capabilities over mmWave PIN diode switches. It is

therefore expected that this switch technology will open up new use cases where the performance of mmWave PIN diode and electromechanical switches do not meet specifications of 5G and 6G communication devices and mmWave radar applications.

Chapter 6

Conclusions & Future Work

6.1 Conclusions

In a world with growing demand for high-speed wireless connectivity, it is clear that the current infrastructure will not be able provide enough bandwidth to the billions of devices that will need a wireless connection over the next decade. In order to meet these demands, industry and researchers have proposed utilizing the mmWave and sub-THz for future generations of wireless communications where spectra are abundant and for the most part unused.

With higher path loss and atmospheric attenuation, mmWave and sub-THz transceivers must compensate by using higher gain antennas and arrays which must have the capability to be electronically steered in order to ensure adequate coverage, which is typically done by phase shifters, Butler matrices, multi-throw switches, or a combination of the above. It is known that the size and complexity of phased array beamformers increase with the number of antenna elements and it is therefore prudent that techniques for miniaturizing these components be investigated.

Components at mmWave and THz frequencies also often use waveguides as interconnects due to their low-loss and high-power handling capabilities. However, waveguides can be difficult to integrate with planar circuits. It is clear that the key to miniaturizing a beamforming network lies in planarizing and miniaturizing waveguide interconnects and components.

First, a low frequency prototype of a miniaturized waveguide, RHMSIW, 4×4 Butler matrix was developed. In this work it was found that the ridge of one asymmetric RHMSIW interconnect can be used to directly feed the ridge of another transversely flipped RHMSIW line. This finding was key to enabling over 70% miniaturization over a reference half-mode design. Two novel 90°RHMSIW bends were also developed to form the fixed delay lines in the Butler matrix. Furthermore, a varactor tuned phase shifter was developed on the same RHMSIW platform and can be integrated with the Butler matrix to enable semi-continuous beam steering. These results were published in [J1] and [C1].

This thesis then demonstrated how the low-frequency Butler matrix prototype can be scaled to the 28 GHz 5G n267 band. Some additional shielding had to be introduced in order to prevent cross coupling between components. Furthermore, a study was conducted to determine what operating region of RHMSIW leads to maximum radiation, and what region allows propagation with minimal radiation loss. The study found that the leaky-wave region of a RHMSIW line can be best predicted to start at intersection point of its attenuation constant (α) with its phase constant (β), and ends where β converges with the wavenumber of the substrate (k). The use of RHMSIW as a leaky-wave antenna was first proposed in [C2] and the results of the 28 GHz Butler matrix were published in [C3]. The study on the leaky-wave region of RHMSIW was recently submitted to the IEEE Transaction on Antennas and Propagation Communications.

Finally, this thesis detailed the design of highly compact photoconductive silicon micromachined evanescent-mode waveguide variable attenuators and double-throw switches. Detailed studies were conducted to establish the engineering trade-offs of evanescent-mode switch designs i.e., isolation, loss, and bandwidth. This work also documented the first-ever switching speed and high-power characterization of silicon micromachined evanescent-mode switches at 85 GHz in addition to the standard S-parameter measurements. The switches were shown to be able to have switching

speeds faster than 4 µs, and experimentally demonstrated to be able to be able to handle 1.6 W of continuous wave RF power in both the ON- and OFF-state of the switch. The switch is competitive with the performance of current state-of-the-art waveguide switches in the W-Band and has 73% reduction in device volume compared to commercially available waveguide switches. These studies and results are published in [J2] and [J3].

6.2 Contributions

The following is a list of academic journal and conference paper contributions published during the course of the doctoral program documented in this thesis.

6.2.1 Related Journal Publications

[J3] E. T. Der et al., "Design and characterization of W-band silicon micromachined high-power and high-speed photoconductive evanescent-mode waveguide single and double throw switches," in IEEE Trans. Microw. Theory Techn., 2023. DOI: 10.1109/TMTT.2023.3328483.

[J2] E. T. Der et al., "A W-band SPDT photoconductive evanescent-mode waveguide switch," in IEEE Microw. Wirel. Techn. Lett., vol. 33, no. 6, pp. 831-834, Jun. 2023.

[J1] E. T. Der, T. R. Jones and M. Daneshmand, "Miniaturized 4 × 4 Butler matrix and tunable phase shifter using ridged half-mode substrate integrated waveguide," in IEEE Trans. Microw. Theory Techn., vol. 68, no. 8, pp. 3379-3388, Aug. 2020.

6.2.2 Related Conference Papers and Abstracts

[C3] E. T. Der, T. R. Jones and M. Daneshmand, "A miniaturized 28 GHz 4×4 Butler matrix using shielded ridged half-mode SIW," IEEE MTT-S Int. Microw.

Symp. Dig., Atlanta, GA, USA, Jun. 2021, pp. 776-779.

[C2] E. T. Der and M. Daneshmand, "Miniaturized Ka-band leaky-wave antenna using ridged half-mode substrate integrated waveguides," 2020 IEEE International Symposium on Antennas and Propagation and North American Radio Science Meeting, Montreal, QC, Canada, Jul. 2020, pp. 241-242

[C1] E. T. Der, T. R. Jones and M. Daneshmand, "Miniaturized tunable phase shifter using a periodically loaded ridged half-mode substrate integrated waveguide," IEEE MTT-S Int. Microw. Symp. Dig., Boston, MA, USA, Jun. 2019, pp. 180-183.

6.2.3 Miscellaneous Journal Publications

[M1] T. R. Jones, N. Vahabisani, E. T. Der, and M. Daneshmand, "Monolithic millimeter-wave air-filled waveguide resonator for filter applications," IEEE Microw. Wirel. Compon. Lett., vol. 29, no. 6, pp. 379–381, 2019.

6.3 Future Work

In this thesis, miniaturized beamforming networks and components were developed in planar waveguide platforms. One of the key things limiting the miniaturization of the proposed Butler matrices is the length of coupling region required for the 0-dB crossover couplers. To achieve even greater miniaturization, methods for miniaturizing the longitudinal length of RHMSIW components need to be developed. Work has also yet to be performed to integrate RHMSIW Butler matrices with compatible antennas and multi-throw switches to create a complete integrated RF frontend.

While the evanescent-mode waveguide switches in this thesis achieved a highly compact form-factor over state-of-the-art waveguide switches, further studies will need to be conducted on transverse miniaturization of evanescent mode waveguides

in order to allow integration of the switch technology with miniaturized waveguide beamformers.

Finally, the future direction of all of the technologies showcased in this thesis is to scale their operation into the sub-terahertz domain.

Bibliography

[1] Y. Ye, D. Wu, Z. Shu, and Y. Qian, "Overview of lte spectrum sharing technologies," *IEEE Access*, vol. 4, pp. 8105–8115, Nov. 2016.

[2] P. Dhull, A. P. Guevara, M. Ansari, S. Pollin, N. Shariati, and D. Schreurs, "Internet of things networks: Enabling simultaneous wireless information and power transfer," *IEEE Microw. Mag.*, vol. 23, no. 3, pp. 39–54, Mar. 2022.

[3] A. A. Abu-Arabia, Iskandar, and R. Hakimi, "Evaluation of 5g nr link efficiency in 28 ghz spectrum sharing," in *2020 6th International Conference on Wireless and Telematics (ICWT)*, Yogyakarta, Indonesia, Sep. 2020, pp. 1–6.

[4] G. Wikström *et al.*, "Challenges and technologies for 6G," in *2020 2nd 6G Wireless Summit (6G SUMMIT)*, Levi, Finland, Mar. 2020, pp. 1–5.

[5] H. Viswanathan and P. E. Mogensen, "Communications in the 6g era," *IEEE Access*, vol. 8, pp. 57 063–57 074, Mar. 2020.

[6] L. U. Khan, I. Yaqoob, M. Imran, Z. Han, and C. S. Hong, "6g wireless systems: A vision, architectural elements, and future directions," *IEEE Access*, vol. 8, pp. 147 029–147 044, Aug. 2020.

[7] D. M. Pozar, *Microwave Engineering*, 4th. Hoboken, NJ, USA: John Wiley & Sons, Inc., Nov. 2011.

[8] S. A. Busari, S. Mumtaz, S. Al-Rubaye, and J. Rodriguez, "5G millimeter-wave mobile broadband: performance and challenges," *IEEE Commun. Mag.*, vol. 56, no. 6, pp. 137–143, Jun. 2018.

[9] M. Giordani, M. Polese, M. Mezzavilla, S. Rangan, and M. Zorzi, "Toward 6g networks: Use cases and technologies," *IEEE Commun. Mag.*, vol. 58, no. 3, pp. 55–61, Mar. 2020.

[10] Qorvo, Inc., *Phase Shifters*, 2021. [Online]. Available: https://www.qorvo.com/products/control-products/phase-shifters, [Accessed on: Sept. 1, 2023.] [Online]. Available: https://www.qorvo.com/products/control-products/phase-shifters.

[11] I. Ahmed, I. Shoaib, S. Shoaib, and N. Shoaib, "A switched-beam three-element printed loop antenna array for mimo systems," in *Proc. 7th Eur. Conf. Antennas Propag. (EuCAP)*, Gothenburg, Sweden, Apr. 2013, pp. 2599–2601.

[12] P. Harati *et al.*, "E-band downlink wireless data transmission for future satellite communication," in *Proc. Topical Workshop on Internet of Space (TWIOS)*, Phoenix, AZ, USA, Jan. 2017, pp. 1–4.

[13] S. Rizvi, A. Aziz, M. T. Jilani, N. Armi, G. Muhammad, and S. H. Butt, "An investigation of energy efficiency in 5g wireless networks," in *2017 International Conference on Circuits, System and Simulation (ICCSS)*, London, UK, Jul. 2017, pp. 142–145.

[14] F. Akbar and A. Mortazawi, "Design of a compact, low complexity scalable phased array antenna," in *IEEE MTT-S Int. Microw. Symp. Dig.*, Phoenix, AZ, USA, Jun. 2015, pp. 1–3.

[15] J. Iannacci, "A perspective vision of micro/nano systems and technologies as enablers of 6G, super-iot, and tactile internet [point of view]," *Proc. IEEE*, vol. 111, no. 1, pp. 5–18, Jan. 2023.

[16] T. R. Jones and M. Daneshmand, "The characterization of a ridged half-mode substrate-integrated waveguide and its application in coupler design," *IEEE Trans. Microw. Theory Techn.*, vol. 64, no. 11, pp. 3580–3591, Nov. 2016.

[17] C. P. Chen *et al.*, "Silicon micromachined waveguide circuit for a 2 THz schottky receiver: Progress and challenges," *IEEE J. Microw.*, vol. 2, no. 4, pp. 592–598, Oct. 2022.

[18] A. Sabban and K. Gupta, "Characterization of radiation loss from microstrip discontinuities using a multiport network modeling approach," *IEEE Trans. Microw. Theory Tech.*, vol. 39, no. 4, pp. 705–712, 1991.

[19] U. Editor, *Waveguide Mathematics*. Accessed: Aug. 20, 2023. [Online]. Available: https://www.microwaves101.com/encyclopedias/waveguide-mathematics.

[20] W. McGrath, C. Walker, M. Yap, and Y.-C. Tai, "Silicon micromachined waveguides for millimeter-wave and submillimeter-wave frequencies," *IEEE Trans. Microw. Guided Wave Lett.*, vol. 3, no. 3, pp. 61–63, 1993.

[21] N. Vahabisani and M. Daneshmand, "Monolithic wafer-level rectangular waveguide and its transition to coplanar waveguide line using a simplified 3-D fabrication process," *IEEE Trans. Compon. Packag. Manuf. Technol.*, vol. 4, no. 1, pp. 168–176, 2014.

[22] F. Xu and K. Wu, "Guided-wave and leakage characteristics of substrate integrated waveguide," *IEEE Trans. Microw. Theory Tech.*, vol. 53, no. 1, pp. 66–73, 2005.

[23] T. R. Jones, N. Vahabisani, E. T. Der, and M. Daneshmand, "Monolithic millimeter-wave air-filled waveguide resonator for filter applications," *IEEE Microw. Wirel. Compon. Lett.*, vol. 29, no. 6, pp. 379–381, 2019.

[24] Y. J. Cheng, K. Wu, and W. Hong, "Power handling capability of substrate integrated waveguide interconnects and related transmission line systems," *IEEE Trans. Adv. Packag.*, vol. 31, no. 4, pp. 900–909, Nov. 2008.

[25] X.-P. Chen and K. Wu, "Substrate integrated waveguide filter: Basic design rules and fundamental structure features," *IEEE Microwave Magazine*, vol. 15, no. 5, pp. 108–116, 2014.

[26] D. Deslandes and K. Wu, "Accurate modeling, wave mechanisms, and design considerations of a substrate integrated waveguide," *IEEE Trans. Microw. Theory Techn.*, vol. 54, no. 6, pp. 2516–2526, Jun. 2006.

[27] W. Hong *et al.*, "Half mode substrate integrated waveguide: A new guided wave structure for microwave and millimeter wave application," in *2006 Joint 31st International Conference on Infrared Millimeter Waves and 14th International Conference on Teraherz Electronics*, 2006, pp. 219–219.

[28] Q. Lai, C. Fumeaux, W. Hong, and R. Vahldieck, "Characterization of the propagation properties of the half-mode substrate integrated waveguide," *IEEE Trans. Microw. Theory Techn.*, vol. 57, no. 8, pp. 1996–2004, Aug. 2009.

[29] N. Marcuvitz, *Waveguide Handbook*. Stevenage, UK: IET, 1986.

[30] T. R. Jones and M. Daneshmand, "Miniaturized slotted bandpass filter design using a ridged half-mode substrate integrated waveguide," *IEEE Microw. Wirel. Compon. Lett.*, vol. 26, no. 5, pp. 334–336, 2016.

[31] T. R. Jones and M. Daneshmand, "The microfabrication of monolithic miniaturized ridged half-mode waveguides for 5G millimeter-wave communication systems," in *IEEE MTT-S Int. Microw. Symp. Dig.*, Philadelphia, PA, USA, Jun. 2018, pp. 323–326.

[32] P. Rizzi, *Microwave Engineering: Passive Circuits*. Eaglewood Cliffs, NJ: Prentice-Hall, 1988.

[33] C.-J. Chen and T.-H. Chu, "Design of 60-ghz siw short-slot couplers," in *2009 Asia Pacific Microwave Conference*, 2009, pp. 2096–2099.

[34] W. M. Abdel-Wahab and S. Safavi-Naeini, "Low loss h-shape siw hybrid coupler for millimeter-wave phased arrays antenna systems," in *Proc. 2012 IEEE Int. Symp. Antennas Propag.*, Chicago, IL, USA, Jul. 2012, pp. 1–2.

[35] A. Doghri, T. Djerafi, A. Ghiotto, and K. Wu, "Substrate integrated waveguide directional couplers for compact three-dimensional integrated circuits," *IEEE Trans. Microw. Theory Techn.*, vol. 63, no. 1, pp. 209–221, Jan. 2015.

[36] B. Liu, W. Hong, Y.-Q. Wang, Q.-H. Lai, and K. Wu, "Half mode substrate integrated waveguide (hmsiw) 3-db coupler," *IEEE Microw. Wirel. Compon. Lett.*, vol. 17, no. 1, pp. 22–24, Jan. 2007.

[37] T. R. Jones and M. Daneshmand, "Miniaturized folded ridged half-mode substrate integrated waveguide," in *2017 47th European Microwave Conference (EuMC)*, 2017, pp. 528–531.

[38] T. R. Jones and M. Daneshmand, "Miniaturized folded ridged half-mode and quarter-mode substrate integrated waveguides for filter design," *IEEE Trans. Microw. Theory Techn.*, vol. 67, no. 8, pp. 3414–3426, Aug. 2019.

[39] T. R. Jones and M. Daneshmand, "Miniaturized reconfigurable dual-band bandstop filter with independent stopband control using folded ridged quarter-mode substrate integrated waveguide," in *IEEE MTT-S Int. Microw. Symp. Dig.*, Boston, MA, USA, Jun. 2019, pp. 102–105.

[40] M. Nosrati and M. Daneshmand, "Substrate integrated waveguide L-shaped iris for realization of transmission zero and evanescent-mode pole," *IEEE Trans. Microw. Theory Techn.*, vol. 65, no. 7, pp. 2310–2320, Jul. 2017.

[41] M. Nosrati and M. Daneshmand, "Gap-coupled excitation for evanescent-mode substrate integrated waveguide filters," *IEEE Trans. Microw. Theory Techn.*, vol. 66, no. 6, pp. 3028–3035, Jun. 2018.

[42] M. Nosrati, Z. Abbasi, and M. Daneshmand, "Single-layer substrate-integrated waveguide evanescent-mode filter," *IEEE Microw. Wirel. Compon. Lett.*, vol. 28, no. 12, pp. 1107–1109, Dec. 2018.

[43] S. Ahmadi, "New Radio Access Physical Layer Aspects (Part 2)," in *5G NR: Architecture, Technology, Implementation, and Operation of 3GPP New Radio Standards*. London, United Kingdom: Academic Press, Jun. 2019, pp. 411–654.

[44] S. Ahmadi, "New Radio Access RF and Transceiver Design Considerations," in *5G NR: Architecture, Technology, Implementation, and Operation of 3GPP New Radio Standards*. London, United Kingdom: Academic Press, Jun. 2019, pp. 655–745.

[45] S. Dutta, C. N. Barati, D. Ramirez, A. Dhananjay, J. F. Buckwalter, and S. Rangan, "A case for digital beamforming at mmwave," *IEEE Trans. Wirel. Commun.*, vol. 19, no. 2, pp. 756–770, Feb. 2020.

[46] A. Alieldin, Y. Huang, M. Stanley, S. D. Joseph, and D. Lei, "A 5G MIMO antenna for broadcast and traffic communication topologies based on pseudo inverse synthesis," *IEEE Access*, vol. 6, pp. 65 935–65 944, Oct. 2018.

[47] Y. Ding and K. Wu, "Varactor-tuned substrate integrated waveguide phase shifter," in *IEEE MTT-S Int. Microw. Symp. Dig.*, Baltimore, MD, USA, Jun. 2011, pp. 1–4.

[48] J. Li, J. Chen, P. Chen, and F. Zhu, "Varactor-tuned half mode substrate integrated waveguide reflection-type phase shifter," in *2012 IEEE MTT-S International Microwave Workshop Series on Millimeter Wave Wireless Technology and Applications*, 2012, pp. 1–3.

[49] L.-S. Wu *et al.*, "A new type of periodically loaded half-mode substrate integrated waveguide and its applications," *IEEE Trans. Microw. Theory Techn.*, vol. 58, no. 4, pp. 882–893, Apr. 2010.

[50] T. Quemerais, D. Gloria, D. Golanski, and S. Bouvot, "High-Q MOS varactors for millimeter-wave applications in CMOS 28-nm FDSOI," *IEEE Electron Device Lett.*, vol. 36, no. 2, pp. 87–89, Feb. 2015.

[51] H.-S. Lee and B.-W. Min, "W-band CMOS 4-bit phase shifter for high power and phase compression points," *IEEE Trans. Circuits Syst. II Express Briefs*, vol. 62, no. 1, pp. 1–5, Jan. 2015.

[52] C.-Y. Huang, K.-H. Hsieh, and R. Hu, "40 nm-CMOS W-band phase shifter for millimeter-wave phased array," in *Proc. Photon. Electromagn. Research Symp. Spring (PIERS-Spring)*, Rome, Italy, Jun. 2019, pp. 1700–1705.

[53] Y. Xiong, X. Zeng, and J. Li, "A frequency-reconfigurable CMOS active phase shifter for 5G mm-Wave applications," *IEEE Trans. Circuits Syst. II Express Briefs*, vol. 67, no. 10, pp. 1824–1828, Oct. 2020.

[54] D.-W. Kang and S. Hong, "A 4-bit cmos phase shifter using distributed active switches," *IEEE Trans. Microw. Theory Tech.*, vol. 55, no. 7, pp. 1476–1483, Jul. 2007.

[55] J.-J. Hung, L. Dussopt, and G. Rebeiz, "Distributed 2- and 3-bit w-band mems phase shifters on glass substrates," *IEEE Trans. Microw. Theory Tech.*, vol. 52, no. 2, pp. 600–606, Feb. 2004.

[56] A. Stehle *et al.*, "RF-MEMS switch and phase shifter optimized for W-band," in *Proc. 38th Eur. Microw. Conf. (EuMC)*, Amsterdam, Netherlands, Oct. 2008, pp. 104–107.

[57] U. Shah *et al.*, "Submillimeter-wave 3.3-bit RF MEMS phase shifter integrated in micromachined waveguide," *IEEE Trans. Terahertz Sci. Technol.*, vol. 6, no. 5, pp. 706–715, May 2016.

[58] X. Zhao, U. Shah, O. Glubokov, and J. Oberhammer, "Micromachined subterahertz waveguide-integrated phase shifter utilizing supermode propagation," *IEEE Trans. Microw. Theory Tech.*, vol. 69, no. 7, pp. 3219–3227, Jul. 2021.

[59] C. Errando-Herranz, A. Y. Takabayashi, P. Edinger, H. Sattari, K. B. Gylfason, and N. Quack, "Mems for photonic integrated circuits," *IEEE J. Sel. Top. Quantum Electron.*, vol. 26, no. 2, pp. 1–16, Feb. 2020.

[60] A. K. Vallappil, M. K. A. Rahim, B. A. Khawaja, N. A. Murad, and M. G. Mustapha, "Butler matrix based beamforming networks for phased array antenna systems: A comprehensive review and future directions for 5G applications," *IEEE Access*, vol. 9, pp. 3970–3987, Jan. 2021.

[61] E. Brookner, "Phased-array and radar breakthroughs," in *Proc. IEEE Radar Conf.*, Waltham, MA, USA, Apr. 2007, pp. 37–42.

[62] C. A. Balanis, *Antenna Theory: Analysis and Design*, 4th ed. Hoboken, NJ, USA: John Wiley & Sons, Inc., Feb. 2016.

[63] Y. J. Cheng *et al.*, "Substrate integrated waveguide (SIW) rotman lens and its Ka-band multibeam array antenna applications," *IEEE Trans. Antennas Propag.*, vol. 56, no. 8, pp. 2504–2513, Aug. 2008.

[64] K. Tekkouk, M. Ettorre, and R. Sauleau, "SIW Rotman lens antenna with ridged delay lines and reduced footprint," *IEEE Trans. Microw. Theory Tech.*, vol. 66, no. 6, pp. 3136–3144, Jun. 2018.

[65] C.-J. Chen and T.-H. Chu, "Design of a 60-GHz substrate integrated waveguide Butler matrix—a systematic approach," *IEEE Trans. Microw. Theory Techn.*, vol. 58, no. 7, pp. 1724–1733, Jul. 2010.

[66] T. Djerafi and K. Wu, "A low-cost wideband 77-GHz planar Butler matrix in SIW technology," *IEEE Trans. Antennas Propag.*, vol. 60, no. 10, pp. 4949–4954, Oct. 2012.

[67] R. Rotman, M. Tur, and L. Yaron, "True time delay in phased arrays," *Proc. IEEE*, vol. 104, no. 3, pp. 504–518, Mar. 2016.

[68] Y. Gao, M. Khaliel, F. Zheng, and T. Kaiser, "Rotman lens based hybrid analog–digital beamforming in massive MIMO systems: array architectures, beam selection algorithms and experiments," *IEEE Trans. Veh. Technol.*, vol. 66, no. 10, pp. 9134–9148, Oct. 2017.

[69] Q.-L. Yang, Y.-L. Ban, J.-W. Lian, Z.-F. Yu, and B. Wu, "SIW Butler matrix with modified hybrid coupler for slot antenna array," *IEEE Access*, vol. 4, pp. 9561–9569, Dec. 2016.

[70] C.-C. Chang, R.-H. Lee, and T.-Y. Shih, "Design of a beam switching/steering Butler matrix for phased array system," *IEEE Trans. Antennas Propag.*, vol. 58, no. 2, pp. 367–374, Feb. 2010.

[71] P. Chen, W. Hong, and J.-f. Xu, "A novel Butler matrix based on half-mode substrate integrated waveguide technology," *J. Microw.*, vol. 14, no. 3, pp. 5–9, Jun. 2008.

[72] A. A. M. Ali, N. J. G. Fonseca, F. Coccetti, and H. Aubert, "Design and implementation of two-layer compact wideband butler matrices in SIW technology for Ku-band applications," *IEEE Trans. Antennas Propag.*, vol. 59, no. 2, pp. 503–512, Feb. 2011.

[73] M.-I. Lai, T.-Y. Wu, J.-C. Hsieh, C.-H. Wang, and S.-K. Jeng, "Compact switched-beam antenna employing a four-element slot antenna array for digital home applications," *IEEE Trans. Antennas Propag.*, vol. 56, no. 9, pp. 2929–2936, Sep. 2008.

[74] V. A. Nguyen and P. S. Ook, "Compact switched and reconfigurable 4-ports beam antenna array for MIMO applications," in *Proc. IEEE MTT-S International Microwave Workshop Series on Intelligent Radio for Future Personal Terminals*, Daejeon, Korea (South), Aug. 2011, pp. 1–3.

[75] M. M. M. Ali and A.-R. Sebak, "Design of compact millimeter wave massive mimo dual-band (28/38 ghz) antenna array for future 5g communication systems," in *Proc. 17th Int. Symp. Antenna Techn. Appl. Electromagn. (ANTEM)*, Montreal, QC, Canada, Jul. 2016, pp. 1–2.

[76] M. A. Al-Tarifi, M. S. Sharawi, and A. Shamim, "Massive MIMO antenna system for 5G base stations with directive ports and switched beamsteering capabilities," *IET Microw. Antennas Propag.*, vol. 12, no. 10, pp. 1709–1718, Aug. 2018.

[77] S. Tao, H. Zhao, Y.-L. Ban, and Z. Chen, "An overlapped switched-beam antenna array with omnidirectional coverage for 2.4/5.8 GHz three-channel MIMO WLAN applications," *IEEE Antennas Wirel. Propag. Lett.*, vol. 19, no. 1, pp. 79–83, Jan. 2020.

[78] Y. Chen, L. Zhang, Y. He, W. Li, and S.-W. Wong, "A pattern reconfigurable SIW horn antenna realized by PIN diode switches," in *2021 Computing, Communications and IoT Applications (ComComAp)*, Shenzhen, China, 2021, pp. 112–115.

[79] E. T. Der, T. R. Jones, and M. Daneshmand, "Miniaturized 4×4 butler matrix and tunable phase shifter using ridged half-mode substrate integrated waveguide," *IEEE Trans. Microw. Theory Techn.*, vol. 68, no. 8, pp. 3379–3388, Aug. 2020.

[80] E. T. Der, T. R. Jones, and M. Daneshmand, "A miniaturized 28 GHz 4×4 butler matrix using shielded ridged half-mode SIW," in *IEEE MTT-S Int. Microw. Symp. Dig.*, Atlanta, GA, USA, 2021, pp. 776–779.

[81] Logus Microwave Corporation, *Waveguide switches.* Accessed: Jul. 27, 2022. [Online]. Available: https://www.logus.com/products/waveguide-switches/.

[82] Quinstar Technology Inc., *Electromechanical waveguide switches QWZ series.* Accessed: Jul. 27, 2022. [Online]. Available: https://quinstar.com/shop/control-products-ferrite/waveguide-pin-switches-single-double-throw/waveguide-pin-switches-double-throw-qss-qsd/.

[83] Eravant Inc., *Electromechanical Waveguide Switches Control Sub-THz Signals.* Accessed: Jul. 6, 2022. [Online]. Available: https://sftp.eravant.com/content/resources/Eravant-MWJ-March-2023-SWJ-Switch.pdf.

[84] Quinstar Technology Inc., *Waveguide PIN switches – double throw QSS/ QSD series.* Accessed: Jul. 27, 2022. [Online]. Available: https://quinstar.com/shop/control-products-ferrite/waveguide-pin-switches-single-double-throw/waveguide-pin-switches-double-throw-qss-qsd/.

[85] T. Sickel, P. Meyer, and P. W. van der Walt, "An in situ tunable diode mounting topology for high-power X-band waveguide switches," *IEEE Trans. Microw. Theory Techn.*, vol. 55, no. 2, pp. 281–286, Feb. 2007.

[86] E. Der, V. Volotovskyy, H. Sun, B. Tomanek, and J. C. Sharp, "Design of a high power PIN-diode controlled switchable RF transmit array for TRASE RF imaging," *Concepts Magn. Reson. B: Magn. Reson. Eng.*, vol. 48B, no. 1, e21365, Feb. 2018, ISSN: 15525031. DOI: 10.1002/cmr.b.21365.

[87] E. Shepeleva, M. Makurin, A. Lukyanov, A. R. Vilenskiy, S. L. Chernyshev, and M. V. Ivashina, "Low-loss K-band photoconductive switches in SIW technology," in *2020 50th European Microwave Conference (EuMC)*, Utrecht, Netherlands, Jan. 2021, pp. 538–541.

[88] E. Shepeleva *et al.*, "Integrated W-band photoconductive switches in SIW technology," *IEEE Microw. Wirel. Compon. Lett.*, vol. 31, no. 7, pp. 865–868, Apr. 2021.

[89] J. Ren, Z. Jiang, P. Fay, J. L. Hesler, C.-Y. E. Tong, and L. Liu, "High-performance WR-4.3 optically controlled variable attenuator with 60-dB range," *IEEE Microw. Wirel. Compon. Lett.*, vol. 28, no. 6, pp. 512–514, Apr. 2018.

[90] J. M. Gonzalez, D. Baillargeat, and L. Roy, "LTCC-based optically tunable microwave filter," in *CCECE 2010*, Calgary, AB, Canada, May 2010, pp. 420–422.

[91] A. W. Pang, S. Bensmida, and M. J. Cryan, "Nonlinearity and power handling characterization of an optically reconfigurable microwave switch," in *IEEE MTT-S Int. Microw. Symp. Dig.*, Philadelphia, PA, USA, Jun. 2018, pp. 420–422.

[92] A. Fisher, Z. V. Missen, T. R. Jones, and D. Peroulis, "A fiber-free DC-7 GHz 35 W integrated semiconductor plasma switch," in *IEEE MTT-S Int. Microw. Symp. Dig.*, Atlanta, GA, USA, 2021, pp. 27–30.

[93] E. K. Kowalczuk, C. J. Panagamuwa, and R. D. Seager, "Design and operation influences regarding rise and fall time of a photoconductive microwave switch," in *2013 Loughborough Antennas & Propagation Conference (LAPC)*, Loughborough, UK, Nov. 2013, pp. 149–154.

[94] T. R. Jones, A. Fisher, D. W. Barlage, and D. Peroulis, "A photogenerated silicon plasma waveguide switch and variable attenuator for millimeter-wave applications," *IEEE Trans. Microw. Theory Techn.*, vol. 69, no. 12, pp. 5393–5403, Dec. 2021.

[95] T. R. Jones, A. Fisher, D. W. Barlage, and D. Peroulis, "A W-band photoconductive evanescent-mode waveguide switch," in *IEEE MTT-S Int. Microw. Symp. Dig.*, Denver, CO, USA, 2022, pp. 959–962.

[96] E. T. Der *et al.*, "A W-band SPDT photoconductive evanescent-mode waveguide switch," *IEEE Microw. Wirel. Technol. Lett.*, vol. 33, no. 6, pp. 831–834, Jun. 2023.

[97] A. Fisher, T. R. Jones, and D. Peroulis, "A DC to 110 GHz plasma switch," in *IEEE MTT-S Int. Microw. Symp. Dig.*, Denver, CO, USA, Jun. 2022, pp. 251–254.

[98] A. Fisher, T. R. Jones, and D. Peroulis, "A reconfigurable reflective/absorptive SPDT plasma switch," in *IEEE MTT-S Int. Microw. Symp. Dig.*, San Diego, CA, USA, Jun. 2023.

[99] A. Fisher, T. R. Jones, and D. Peroulis, "Design and optimization of a high-power solid-state plasma RF switch," *IEEE Trans. Microw. Theory Tech.*, 2023. DOI: 10.1109/TMTT.2023.3297365.

[100] J. O. García, J. C. Melgarejo Lermas, V. E. Boria, and M. Guglielmi, "On the integration of microwave filters and waveguide switches," *IEEE Microw. Wirel. Compon. Lett.*, vol. 31, no. 3, pp. 265–268, Mar. 2021.

[101] X. Zhao, O. Glubokov, and J. Oberhammer, "A silicon-micromachined waveguide platform with axial ports for integrated sub-THz filters," *IEEE Trans. Microw. Theory Tech.*, vol. 70, no. 2, pp. 1221–1232, Feb. 2022.

[102] 3GPP Organizational Partners, "3GPP TS 38.101-1," 3GPP, Valbonne, France, Tech. Rep., 2017.

[103] B. Horwath and R. Abhari, "A 60 GHz 2×2 planar phased array with SIW modified butler matrix feed," in *Proc. 2016 IEEE Int. Symp. Antennas Propag. (APSURSI)*, Fajardo, PR, USA, Jun. 2016, pp. 1147–1148.

[104] D. Kholodniak, G. Kalinin, E. Vernoslova, and I. Vendik, "Wideband 0-dB branch-line directional couplers," in *IEEE MTT-S Int. Microw. Symp. Dig.*, vol. 3, Boston, MA, USA, Jun. 2000, 1307–1310 vol.3.

[105] X. Wang, X.-W. Zhu, L. Tian, P. Liu, W. Hong, and A. Zhu, "Design and experiment of filtering power divider based on shielded HMSIW/QMSIW technology for 5G wireless applications," *IEEE Access*, vol. 7, pp. 72 411–72 419, May 2019.

[106] F.-L. Lin and R.-B. Wu, "Computations for radiation and surface-wave losses in coplanar waveguide bandpass filters," *IEEE Trans. Microw. Theory Techn.*, vol. 47, no. 4, pp. 385–389, Apr. 1999.

[107] F. Monticone and A. Alù, "Leaky-wave theory, techniques, and applications: From microwaves to visible frequencies," *Proc. IEEE*, vol. 103, no. 5, pp. 793–821, May 2015.

[108] J. Coonrod, *Don't Get Lost in the Layers and the Smaller Wavelengths*, Accessed: Aug. 2, 2023. [Online]. Available: https://www.microwavejournal.com/blogs/1-rog-blog/post/35658-dont-get-lost-in-the-layers-and-the-smaller-wavelengths.

[109] J. Xu, W. Hong, H. Tang, Z. Kuai, and K. Wu, "Half-mode substrate integrated waveguide (HMSIW) leaky-wave antenna for millimeter-wave applications," *IEEE Antennas Wirel. Propag. Lett.*, vol. 7, pp. 85–88, Apr. 2008.

[110] A. J. Martinez-Ros, J. L. Gómez-Tornero, and F. Quesada-Pereira, "Efficient analysis and design of novel SIW leaky-wave antenna," *IEEE Antennas Wirel. Propag. Lett.*, vol. 12, pp. 496–499, Apr. 2013. DOI: 10.1109/LAWP.2013.2256769.

[111] D. R. Jackson and A. A. Oliner, "Leaky-wave antennas," in *Modern Antenna Handbook*, C. A. Balanis, Ed., Hoboken, NJ: John Wiley & Sons, Ltd, 2008, ch. 7, pp. 325–367.

[112] Q. Lai, C. Fumeaux, and W. Hong, "On the transition from radiating to guiding behavior of the half-mode substrate integrated waveguide," in *Proc. 2010 Asia-Pacific Microw. Conf.*, Yokohama, Japan, Dec. 2010, pp. 1601–1604.

[113] A. A. Oliner and D. R. Jackson, "Leaky-wave antennas," in *Antenna Engineering Handbook*, J. L. Volakis, Ed., 4th ed., New York: McGraw-Hill Education, 2007, ch. 11.

[114] L. Goldstone and A. Oliner, "Leaky-wave antennas I: Rectangular waveguides," *IRE Trans. Antennas Propag.*, vol. 7, no. 4, pp. 307–319, Oct. 1959.

[115] N. Nguyen-Trong and C. Fumeaux, "Half-mode substrate-integrated waveguides and their applications for antenna technology: A review of the possibilities for antenna design," *IEEE Antennas Propag. Mag.*, vol. 60, no. 6, pp. 20–31, Dec. 2018.

[116] R. Marks, "A multiline method of network analyzer calibration," *IEEE Trans. Microw. Theory Techn.*, vol. 39, no. 7, pp. 1205–1215, Jul. 1991.

[117] F. Xu and K. Wu, "Numerical multimode calibration technique for extraction of complex propagation constants of substrate integrated waveguide," in *IEEE MTT-S Int. Microw. Symp. Dig.*, vol. 2, Fort Worth, TX, USA, Jun. 2004, 1229–1232 Vol.2.

[118] T. R. Jones, "Miniaturization of Microwave to Millimeter-Wave Integrated Waveguides and their Applications," Ph.D. dissertation, University of Alberta, 2019. DOI: 10.7939/r3-kj81-sf41.

[119] M. Kishihara, K. Fujitani, A. Yamaguchi, Y. Utsumi, and I. Ohta, "Design and Fabrication of PTFE Substrate-Integrated Waveguide Butler Matrix for Short Millimeter Waves," *IEICE Trans. Electron.*, no. 3, pp. 111–115, Mar. 2023. DOI: 10.1587/transele.2022ECS6003.

[120] A. Tamayo-Domínguez, J.-M. Fernández-González, and M. Sierra-Castañer, "3-d-printed modified butler matrix based on gap waveguide at w-band for monopulse radar," *IEEE Trans. Microw. Theory Techn.*, vol. 68, no. 3, pp. 926–938, Mar. 2020.

[121] A. Krivovitca, U. Shah, O. Glubokov, and J. Oberhammer, "Micromachined silicon-core substrate-integrated waveguides with co-planarprobe transitions at 220–330 GHz," in *IEEE MTT-S Int. Microw. Symp. Dig.*, Philadelphia, PA, USA, Jun. 2018, pp. 190–193.

[122] S. Sze and K. K. Ng, *Physics of Semiconductor Devices*. Hoboken, NJ, USA: John Wiley & Sons, Inc., Oct. 2006.

[123] C. Hu, *Modern Semiconductor Devices for Integrated Circuits*. Upper Saddle River, NJ, USA: Prentice-Hall, Mar. 2009.

[124] G. Craven and C. Mok, "The design of evanescent mode waveguide bandpass filters for a prescribed insertion loss characteristic," *IEEE Trans. Microw. Theory Techn.*, vol. 19, no. 3, pp. 295–308, Mar. 1971.

[125] P. Ludlow, V. Fusco, G. Goussetis, and D. E. Zelenchuk, "Applying band-pass filter techniques to the design of small-aperture evanescent-mode waveguide antennas," *IEEE Trans. Antennas Propag.*, vol. 61, no. 1, pp. 134–142, Jan. 2013.

[126] J.-S. Hong and M. J. Lancaster, *Microstrip Filters for RF / Microwave*, 2nd. Hoboken, NJ, USA: John Wiley & Sons, Inc., Mar. 2011.

[127] G. M. Rebeiz, *RF MEMS: Theory, Design, and Technology*. Hoboken, NJ, USA: John Wiley & Sons, Inc., Feb. 2003.

[128] R. J. Cameron, C. M. Kudsia, and R. R. Mansour, *Microwave Filters for Communication Systems*. Hoboken, NJ, USA: John Wiley & Sons, Inc., Mar. 2018.

[129] M. G. Hogg, I. V. Timoshkin, S. J. MacGregor, M. P. Wilson, M. J. Given, and T. Wang, "Electrical breakdown of short non-uniform air gaps," in *2013 19th IEEE Pulsed Power Conference (PPC)*, San Francisco, CA, USA, Jun. 2013, pp. 1–4.

[130] I. Lim and S. Lim, "Substrate-integrated-waveguide (SIW) single-pole-double-throw (SPDT) switch for X-band applications," *IEEE Microw. Wirel. Compon. Lett.*, vol. 24, no. 8, pp. 536–538, Aug. 2014.

[131] R. E. Collin, *Field Theory of Guided Waves*. New York: Wiley-IEEE, 1991.

[132] R Mavaddat, *Network Scattering Parameters* (Advanced Series in Circuits and Systems). Singapore: WORLD SCIENTIFIC, Mar. 1996, vol. 2, ISBN: 978-981-02-2305-2. DOI: 10.1142/2791. [Online]. Available: https://www.worldscientific.com/worldscibooks/10.1142/2791.

[133] D. Frickey, "Conversions between S, Z, Y, H, ABCD, and T parameters which are valid for complex source and load impedances," *IEEE Trans. Microw. Theory Techn.*, vol. 42, no. 2, pp. 205–211, Feb. 1994. DOI: 10.1109/22.275248.

Appendix A: General Fabrication Process for RHMSIW Structures

Although the RHMSIW is a multilayer PCB structure, the fabrication procedure is relatively simple since the bonded bottom substrate serve only as a "ground" plane and therefore does not need to be aligned with patterned structures on the top substrate when pressed bonded. The equipment used for drilling and milling the substrates are the LPKF ProtoMat S62 and the LPKF ProtoLaser U3 respectively.

A.1 Preparation of the Top Substrate and Drilling Blind Vias

The LPKF ProtoMat S62 has a ±25 µm positional tolerance associated with its drill which may be unacceptable especially for designs where the tolerance is a significant fraction of the diameter of via interconnects that are to be drilled on a substrate. To improve the positional accuracy of the drilled holes, the LPKF ProtoLaser U3 was used to mark pilot holes on the surface of the substrate material.

Fig. A.1 illustrates the preliminary steps of drilling the blind via interconnects linking the top and ridge layers of a RHMSIW structure on the top substrate.

First, 1.5 mm fiducial holes are drilled into the top substrate using the S62 for the purpose of alignment. The board is then aligned on the U3 which was setup such that circles of diameter 0.1 mm to 0.2 mm smaller than the desired via diameter are milled away from the copper where the centers of the interconnects are to be in the final design. This ensures that the drill bit in the S62 will sink into the desired

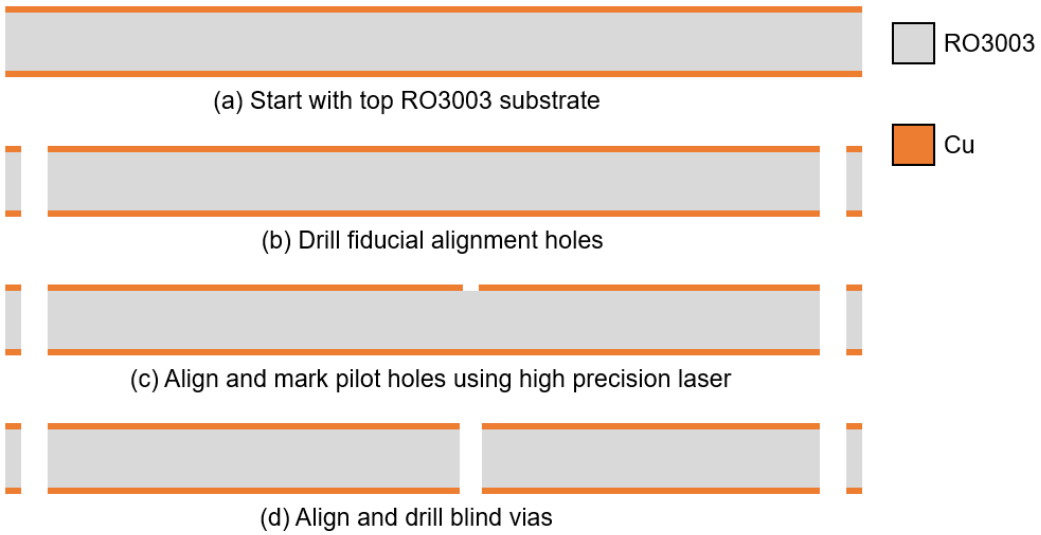

Figure A.1: Process flow for marking pilot holes and drilling blind vias for the top substrate of RHMSIW structures.

hole positions with reasonable accuracy before drilling into the substrate material. The board is then re-aligned on the S62 and all of the blind vias connecting the top metallization layer to the ridge layer are drilled in this step.

A.2 Cleaning the Blind Vias

Both surfaces of the drilled substrate are deburred by sanding. The substrate is then rinsed with water; the board should be pressed against the hose as firmly as possible so as to allow the pressure from the water to force any copper flakes or substrate fibres left over from the drilling process out of the drilled hole. The board is then dried with a nitrogen gas nozzle. If holes still appear to be obstructed after inspection, the board should be rinsed and dried again. If the problems persist, the board can be re-aligned on the S62 to press any remaining obstructions out by drilling; thoroughly rinse and dry after drilling.

A.3 Electroplating the Blind Vias

The via interconnects are to be electroplated in a copper (II) sulfate / sulfuric acid solution. Since the walls of the drilled holes are non-conductive, they must be coated with an activator prior to electroplating. The powdered silver and carbon "Conductive Electroplating Ink" from Think & Tinker Ltd. was applied to one side of the drilled board. The holes on the board must then be thoroughly vacuumed to ensure that the ink does not obstruct the plating solution. The board is then flipped and the process is repeated. If obstructed holes are observed, repeat the steps described in step A.2 and reapply the ink. Once the board has been inspected, the ink must be hard baked for 30 minutes at 100°C. A cross-section of the resultant structure is depicted in Fig. A.2(a).

The board is to be plated for a duration of one hour with a DC current such that the average surface current density across the board is 7.0 A/ft^2. When calculating the total surface area of the board it is prudent to multiply the total board area by two so as to include the area of the top and bottom of the substrate. The positive terminal of the power supply is to be connected to the sacrificial copper material and the negative terminal to the substrate. Thoroughly rinse off all acid residue from the electroplated board with deionized water and dry. The electroplated cross-section of the structure is shown in Fig. A.2(b).

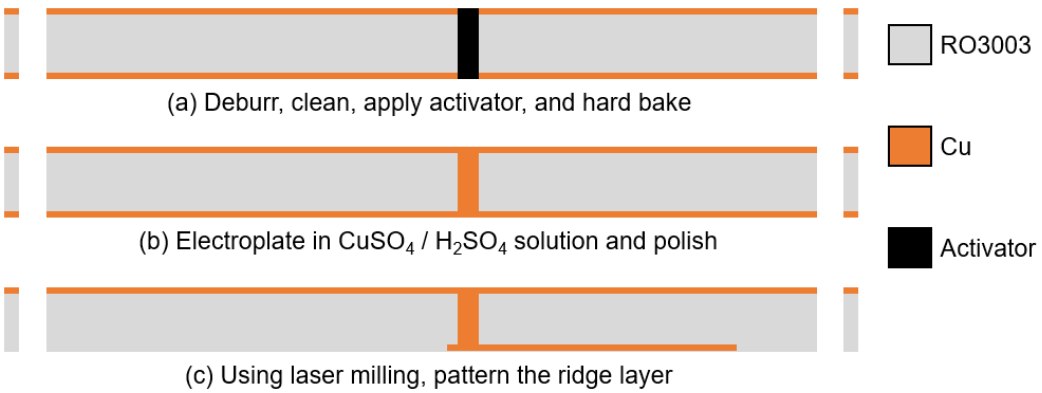

Figure A.2: Process flow depicting the electroplating of blind vias and patterning of the ridge layer.

A.4 Patterning the Ridge Layer

The electroplated copper faces of the board are to be thoroughly polished with a sanding pad prior to laser milling on the U3. With the face where the ridge layer patterns are to be patterned facing up, the board is aligned using the fiducial holes drilled in steps A.1 and milled. The fully processed top substrate is shown in Fig. A.2(c).

A.5 Preparing the Bottom Substrate and Press Bonding

For substrates that are laminated with copper on both faces, one face of the substrate is to be blanketed with a non-permeable tape and then dropped in a copper etchant bath. For substrates that are only laminated on one face, chemical etching is not required. When cleaving the bottom substrate for bonding with the patterned top substrate, it should generally be slight larger in area than the top substrate in order to completely eliminate the need for alignment and also as an extra precaution to account for any drifting of materials during press bonding. For the same reasons, the bonding sheets to be pressed in between the two substrates should be slightly larger than the bottom substrate. Follow the bonding material manufacturer's processing instructions for press bonding.

A.6 Processing the Bonded Substrates

Repeat the steps described in steps A.1 to A.4 in the order presented for the drilling and plating of through vias, and the patterning of the top conducting layer. Fig. A.3 summarizes the steps to be repeated for the processing of through via interconnects and the top conductor of the RHMSIW structure on the bonded board.

If the ground plane defects need to be patterned (such as the device presented in Chapter 4), a new set of fiducial holes need to be drilled using the alignment provided by the original set as the presence of the bottom substrate now renders the original

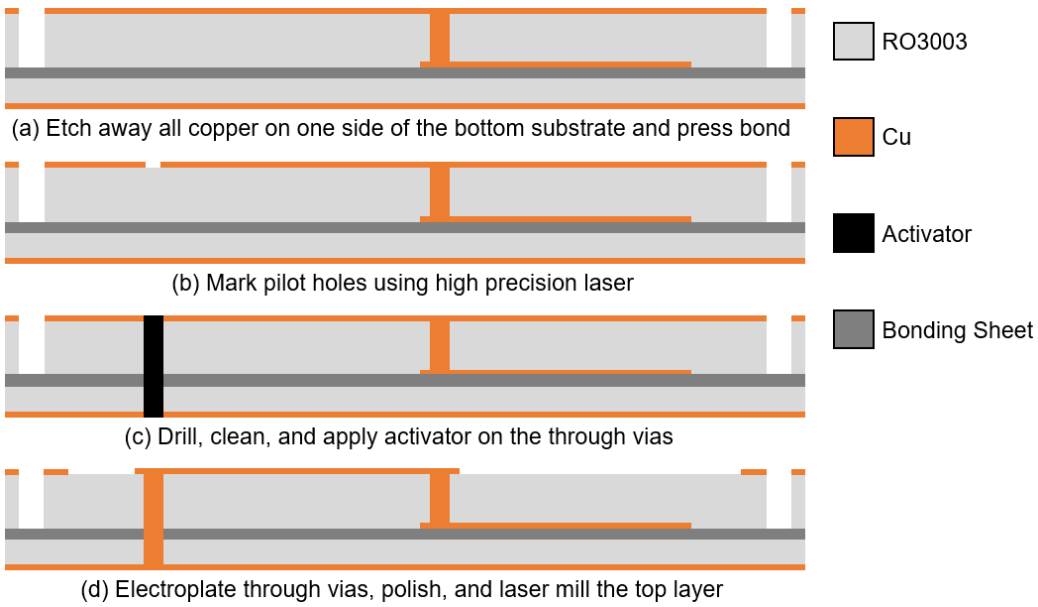

Figure A.3: Illustration of the final fabrication steps on the bonded substrate.

fiducials "blind". The board can then be aligned on the LPKF U3 with the ground conductor facing up using the new set of "through" fiducials and milled.

Appendix B: Supplementary Content on Varactor Loaded RHMSIW Phase Shifters

Here the principle of operation, and additional simulated and measured data on the RHMSIW tunable phase shifter is presented. The biasing network of the design in Chapter 3 was modified from the design presented here to simplify the assembly and experiment setup.

B.1 Principle of Operation

The design presented in this paper is a miniaturized tunable phase shifter constructed using RHMSIW technology for operation in the 5G frequency bands between 2.5 and 3.7 GHz. Periodic varactor loading is applied across the waveguide, modifying the overall phase velocity of the fundamental quasi-$TE_{0.5,0}$ propagation mode, allowing one to dynamically tune the amount of phase incurred within the transmission coefficient S_{21}. In this section, the design and periodic loading of a RHMSIW is first described, outlining the calculation of the fundamental mode cutoff frequency using the transverse resonance technique, and the effect of periodic loading on the propagation constant and the generation of bandgaps in the dispersion relation. Finally, the overall design layout of the tunable phase shifter using varactor loading is presented, along with design considerations in regards to varactor spacing and bias network.

B.1.1 Periodic Loading of Ridged Half-Mode SIW

As was discussed in Chapter 2, it was previously shown in [27] that a virtual magnetic wall can be introduced down the center of an SIW waveguide, bisecting the transverse plane. The footprint of SIWs can then be halved by omitting all of the conductors on one side of the PMC wall without violating any boundary conditions due to the high width to height ratio. This HMSIW can then be further miniaturized by capacitively loading the open side of the waveguide with a reduced height ridge structure, forming a RHMSIW as shown in Fig. 3.2(a).

In Fig. 3.2(b), an equivalent transverse circuit model of the RHMSIW cross-section is shown, where the transverse resonance method can be used to compute the waveguides propagation constant [16]. Accordingly, the sum of the input admittance looking to the left and right at the reference plane equates to zero, yielding the equation:

$$Y_{in}^{(1)} + Y_{in}^{(2)} = 0, \tag{B.1}$$

which can be expanded into:

$$-\cot(k_c W) + \frac{B}{Y_{01}} + \frac{Y_{02}}{Y_{01}} \tan(k_c W_r) = 0 \tag{B.2}$$

where W is the width of the waveguide channel, W_r is the width of the capacitive ridge, kc is the cutoff wavenumber of the fundamental quasi-$\mathrm{TE}_{0.5,0}$ mode, B is the susceptance introduced by the step from the waveguide channel to the capacitive ridge, Y_{01} and Y_{02} are respectively the characteristic admittance of the waveguide channel and ridge channel, and $Y_{in}^{(1)}$ and $Y_{in}^{(2)}$ are the input admittance looking to the left and right of the reference plane. The propagation constant β of an unloaded RHMSIW can then be obtained as follows:

$$\beta = \sqrt{k^2 - k_c^2} \tag{B.3}$$

The propagation constant β_p of a general periodically loaded transmission line (TL) capacitively loaded with a susceptance $b = \omega C$ at periodic distance d in between each

element can be computed as follows [131]:

$$\beta_p d = \cos^{-1}\left[\cos(\beta d) - \frac{b}{2}\sin\beta d\right] \tag{B.4}$$

where β is the propagation constant of the unloaded TL.

The following results can be inferred from equations (B.2) to (B.4):

1. If we increase the amount of capacitive loading on the waveguide ridge, the cutoff frequency of the propagation constant decreases, increasing the amount of phase incurred across a fixed length and operating frequency. Furthermore, tunable elements will introduce more capacitive loading to the structure, while also allowing for tuning of the cutoff frequency. The waveguide dimensions will have to be optimized such that the lower 3 dB cutoff of S_{21} is at f_c of the new periodically loaded waveguide when under maximum capacitive loading.

2. At any given frequency and loading period, the propagation constant and phase incurred in the TL varies with capacitive loading.

3. The argument of the arccosine in (B.4) must be bound between [-1, 1] for a solution to exist. Therefore, there are bandgaps that exist periodically with frequency at a given b.

4. As b increases, the first bandgap of the TL shifts down in frequency as well as the cutoff of β_p.

For the most effective loading of the RHMSIW, the loading elements must be placed where the transverse electric field is at its maximum, i.e., between the open edge of the ridge structure and ground. Because the ridge of the RHMSIW is embedded in between two substrates, the elements must be connected to the ridge using blind via holes to the top metal layer. This introduces parasitic series inductance to the tuning elements, which must be taken into consideration. Furthermore, it was shown in [16] that the maximum miniaturization is achieved when W_r is approximately 0.45 to 0.55 times the total width of the waveguide ($W + W_r$).

B.1.2 Final Tunable Phase Shifter Design

In Fig. B.1, the final design layout of a tunable periodically loaded RHMSIW phase shifter taking the above considerations into account is shown. The proposed design was fabricated on Rogers RO3003 substrates. The top plate and embedded ridge is milled on a 30 mil substrate and bonded to a 10 mil substrate laminated with the ground plane using 4 mil thick Rogers RO4450F Bondply in the process adapted from [16] and described in Appendix A. All vias on the layout have a diameter of 0.5 mm. The final area of the layout is 59.9 mm by 12.7 mm.

For the tuning elements, Skyworks SMV2019-040-LF varactors with 4.8 Ω and 0.45 nH of parasitic series resistance and inductance are chosen. The layout of the varactor bias network is shown in Fig. B.2. Each varactor diode anode is connected to DC ground through a blind via connecting the top layer of the PCB to the ridge of the waveguide and a positive bias V_{CC} is applied to each of the cathodes through 22 kΩ resistors which forms a uniform high impedance RF choke across all frequencies. A strip of through vias at the bottom of the layout connects the varactor to the RF ground plane of the waveguide. The grounding strip is loaded with tightly packed vias to minimize the parasitic series inductance introduced. In [49], it was shown that the periodic distance between each varactor load should be as small as possible for wide bandgaps, but the biasing network and the varactor itself must be able to physically fit in between each period. Taking these trade-offs into account, the varactors in the final design were placed 2.1336 mm apart from each other with a total of 10 varactors along the waveguide ridge.

The layout shown in Fig. B.1 was simulated using Keysight ADS with biasing pads, via interconnects, and varactor SPICE models included to account for all parasitic inductance and capacitance.

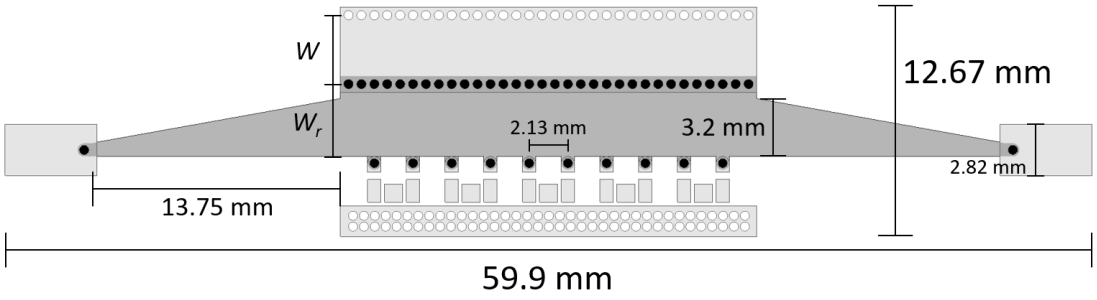

Figure B.1: The top down view of the proposed phase shifter layout with the dimensions of the waveguide structure. The top conductor layer is depicted in light gray and the embedded layer is in dark gray, blind vias are in black, and through vias are in white. $W = 3.8$ mm and $W_r = 4.0$.

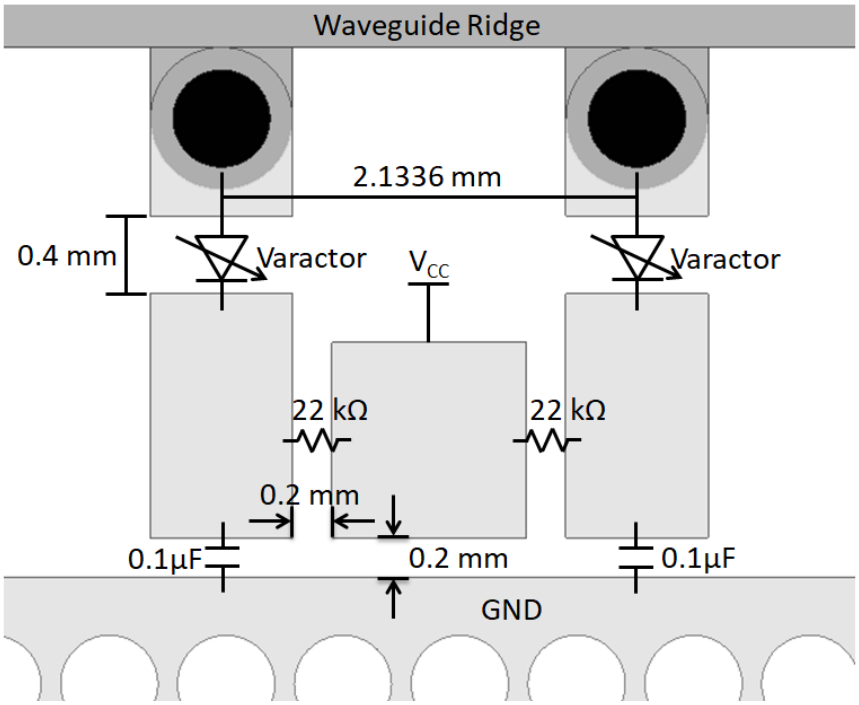

Figure B.2: The top down close-up view of the varactor biasing network layout with dimensions.

B.2 Results and Discussion

In Fig. B.3, a picture of the fabricated device is shown. The final design area including varactor bias network is 59.9 mm by 12.67 mm. Fig. B.4 plots the measured and simulated scattering parameters for a bias voltage of 7.2 V, showing good agreement between the simulation model and measurement. The small discrepancy

is likely due to additional parasitics introduced by the soldered SMA connectors and components.

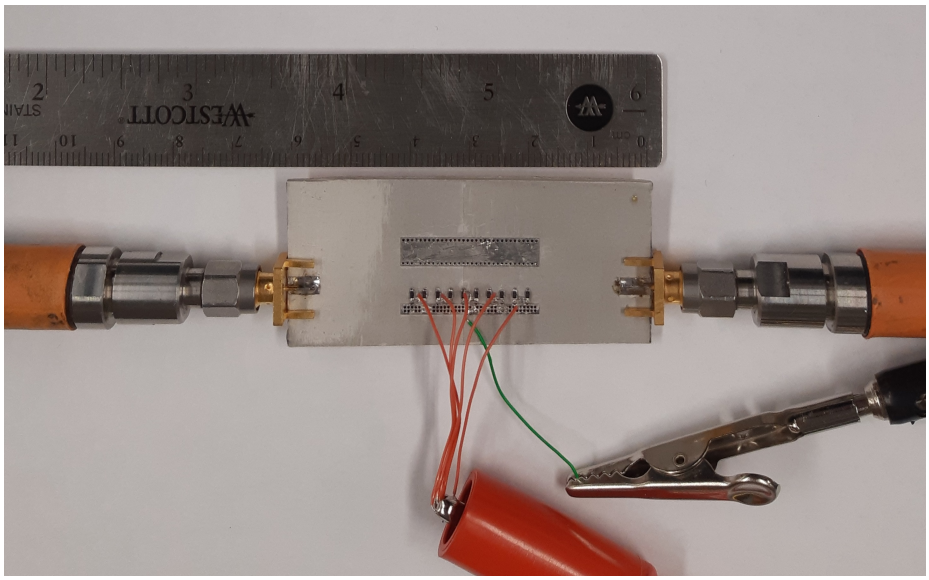

Figure B.3: Measured and simulated scattering parameters versus frequency response with bias voltage 7.2 V applied to the varactors.

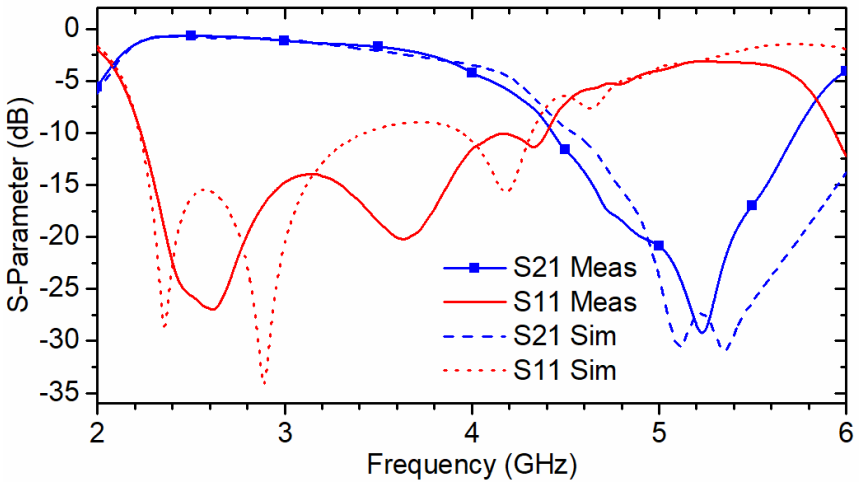

Figure B.4: Measured and simulated scattering parameters versus frequency response with bias voltage 7.2 V applied to the varactors.

In Fig. B.5(a), the measured $|S_{21}|$ for different bias voltages is shown. In the plot, it can clearly be seen that as the capacitive loading increases by decreasing the bias voltage, the bandgap decreases in frequency. Self-resonance with parasitic inductance in the varactor package and the soldering joints causes the bandgap to further decrease

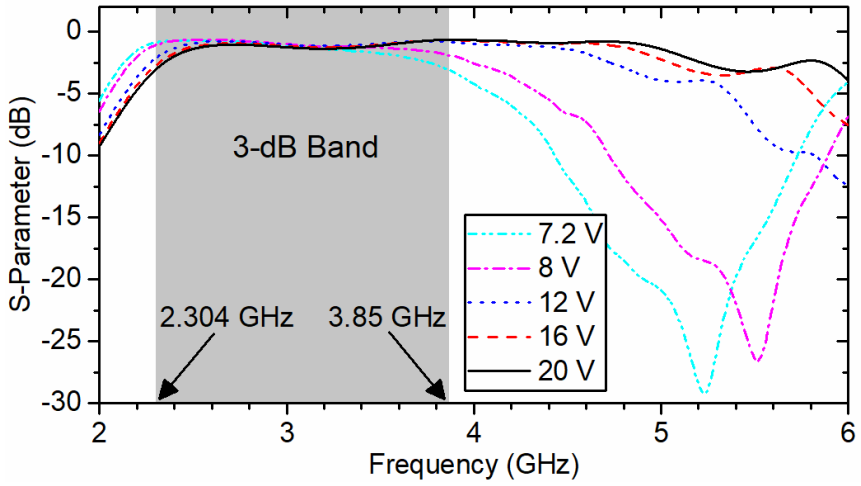

(a)

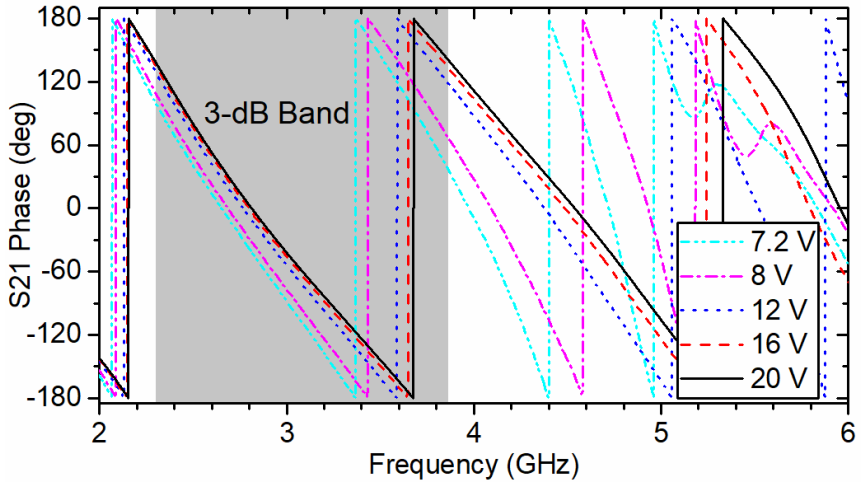

(b)

Figure B.5: (a) Measured $|S_{21}|$ and (b) phase of S_{21} versus frequency response with varying biasing voltages applied to the varactors.

in frequency and is one of the main factors contributing to insertion loss / reduced phase tunability. In Fig. B.5(b), the measured phase of S_{21} is plotted for different bias voltages. The fabricated device is capable of 102.416°, 48.624°, and 38.679° of phase tuning at 3.85 GHz, 3.077 GHz, and 2.304 GHz respectively. In Fig. 7, the relative phase shift versus bias voltage for the lower, middle, and upper 3 dB band frequencies are plotted.

Table I compares the performance and miniaturization of the tunable periodically loaded RHMSIW phase shifter with the HMSIW phase shifter in [49]. The total

width of the waveguide channels are normalized to the lower cutoff wavelength in the substrate the devices are fabricated on and it was found that the design presented in this paper achieves a 34.13% width reduction while achieving comparable phase shift. Note that the normalized width is less than 0.25λ and 0.125λ for the HMSIW and RHMSIW respectively because the capacitance introduced from varactor loading miniaturizes the devices further. The design using RHMSIW provides more tunability because the structure suffers less radiation loss and therefore incurs lower insertion loss compared to HMSIW as was shown in [16]. Lower insertion loss allows for more varactor loading and higher capacitance tuning before the lower or upper band cutoffs drops below 3 dB.

B.3 Summary

The design of a novel miniaturized tunable periodically loaded RHMSIW phase shifter design suitable for use in 5G communications applications was presented. With comparable performance to existing HMSIW based designs at similar frequencies, a reduction in footprint of 34.13% and maximum phase tunability of 102.4° at 3.85 GHz was achieved. With some minor reworking, the design can also be scaled up to operate at the newer 5G millimeter wave bands.

Appendix C: Extracting Propagation Constants using the Multiline Method

It is known that the S-Parameter matrix cannot be cascaded. The S-matrices obtained from a full-wave EM simulator such as HFSS or from measurements on a VNA:

$$[S] = \begin{bmatrix} S_{11} & S_{12} \\ S_{21} & S_{22} \end{bmatrix} \tag{C.1}$$

must therefore be converted into "transfer S-matrices", or T-matrices for the analysis detailed in this appendix:

$$[T] = \begin{bmatrix} T_{11} & T_{12} \\ T_{21} & T_{22} \end{bmatrix}. \tag{C.2}$$

[S] can be converted into [T] with the following equations [132, 133]:

$$T_{11} = \frac{1}{S_{21}} \tag{C.3}$$

$$T_{12} = -\frac{S_{22}}{S_{21}} \tag{C.4}$$

$$T_{21} = \frac{S_{11}}{S_{21}} \tag{C.5}$$

$$T_{22} = -\frac{\det[S]}{S_{21}}. \tag{C.6}$$

The multiline method of extracting the propagation constant $\gamma = \alpha + j\beta$ of a waveguide or transmission line requires that two lines - that are identical in all dimensions apart from longitudinal length - be measured or simulated. Fig. C.1 depicts a block diagram representation of the T-matrix of two transmission lines with different lengths.

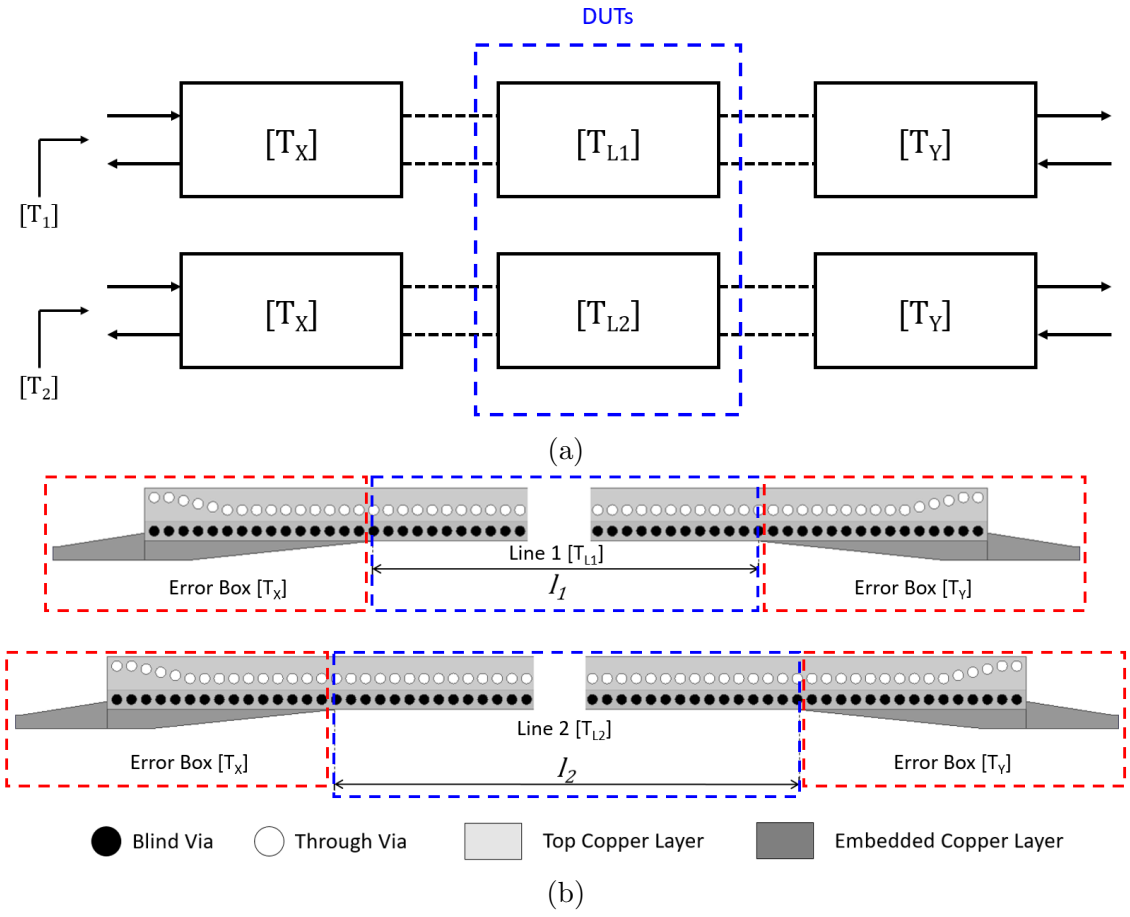

Figure C.1: Illustrations of the multiline method of extracting propagation constants. (a) The block diagram representation. (b) A layout of the simulation models used for extracting β in Chapter 4.

$[T_X]$ and $[T_Y]$ are "unknown cascade matrices" [116] or "error boxes" [118] that represent generic transitions, connectors, and/or ports that feed the lines of two lengths, a shorter one with T-matrix $[T_{L1}]$, and a longer line with T-matrix $[T_{L2}]$.

Cascaded, the T-matrices of the overall measurements are:

$$[T_1] = [T_X][T_{L1}][T_Y] \tag{C.7}$$

and

$$[T_2] = [T_X][T_{L2}][T_Y]. \tag{C.8}$$

If $[T_{L1}]$ and $[T_{L2}]$ represent the T-matrices of matched lines, they should be diagonal matrices in the form of [116]:

$$[T_{L(n)}] = \begin{bmatrix} e^{-\gamma l_{(n)}} & 0 \\ 0 & e^{+\gamma l_{(n)}} \end{bmatrix} \tag{C.9}$$

and its inverse will be in the form of:

$$[T_{L(n)}]^{-1} = \begin{bmatrix} e^{+\gamma l_{(n)}} & 0 \\ 0 & e^{-\gamma l_{(n)}} \end{bmatrix} \tag{C.10}$$

where $l_{(n)}$ is the length of the line.

Inverting $[T_1]$ we obtain:

$$[T_1]^{-1} = [T_Y]^{-1}[T_{L1}]^{-1}[T_X]^{-1} = [T_Y]^{-1} \begin{bmatrix} e^{+\gamma l_1} & 0 \\ 0 & e^{-\gamma l_1} \end{bmatrix} [T_X]^{-1} \tag{C.11}$$

where $l_{(n)}$ is the length of the line.

Multiplying (C.11) with (C.8), we obtain:

$$[T_P] = [T_X]^{-1}[T_{L1}]^{-1}[T_{L2}][T_X] = [T_X]^{-1} \begin{bmatrix} e^{-\gamma(l_2-l_1)} & 0 \\ 0 & e^{+\gamma(l_2-l_1)} \end{bmatrix} [T_X]. \tag{C.12}$$

In this form, $[T_P]$ and $[T_{L1}]^{-1}[T_{L2}]$ are known as similar matrices with identical eigenvalues. Therefore the eigenvalues of $[T_P]$ are:

$$\lambda = e^{\pm\gamma(l_2-l_1)} \tag{C.13}$$

which can be rearranged to solve for the complex propagation constant ($\gamma = \alpha + j\beta$) of the line under test.